

## NATIONAL & INTERNATIONAL SCIENTIFIC EVENTS

Euro PM2023 Congress and Exhibition

Venue: Lisbon Congress Centre  
 Location: Lisbon, Portugal

Begins: October 01, 2023  
 Ends: October 04, 2023

15th ISRM Congress 2023

Venue: Salzburg Congress  
 Location: Salzburg, Austria

Begins: October 09, 2023  
 Ends: October 14, 2023

7th World Engineers Convention

Venue: Prague Congress Centre  
 Location: Prague, Czech Republic

Begins: October 11, 2023  
 Ends: October 13, 2023

16th Asian Congress on Biotechnology

Venue: Tan Son Nhat Hotel  
 Location: Ho Chi Minh City, Tayland

Begins: October 15, 2023  
 Ends: October 19, 2023

International Conference on Ubiquitous Information Management and Communication

Venue: Offline and Online  
 Location: Kuala Lumpur, Malaysia

Begins: January 03 2024  
 Ends: January 05, 2024

IEEE Consumer Communications &amp; Networking Conference

Venue: Flamingo Hotel  
 Location: Las Vegas, USA

Begins: January 06 2024  
 Ends: January 09, 2024

The 37th International Conference on Micro Electro Mechanical Systems

Venue: AT&T Hotel and Conference Center  
 Location: Texas, USA

Begins: January 21 2024  
 Ends: January 25, 2024

The 14th International Conference on Key Engineering Materials

Venue: N/A  
 Location: Dubai, United Arab Emirates

Begins: March 06 2024  
 Ends: March 09, 2024

10th International Conference on Computer Technology Applications

Venue: Hotel Ibis Wien Mariahilf  
 Location: Vienna, Austria

Begins: May 15 2024  
 Ends: May 17, 2024

12nd World Biomaterials Congress

Venue: EXCO  
 Location: Daegu, Korea

Begins: May 26 2024  
 Ends: May 31, 2024

22nd Triennial Congress of The International Ergonomics Association

Venue: Jeju International Convention Center  
 Location: Jeju Island, Korea

Begins: August 25 2024  
 Ends: August 29, 2024

18th European Conference on Soil Mechanics and Geotechnical Engineering

Venue: Altice Arena  
 Location: Lisbon, Portugal

Begins: August 26 2024  
 Ends: August 30, 2024

# HITTITE

JOURNAL OF SCIENCE & ENGINEERING

HJSE Official Journal of Hitit University Volume 10, Issue 3, 2023 dergipark.org.tr/en/pub/hjse



HJSE Official Journal of Hitit University Volume 10, Issue 3, 2023 dergipark.org.tr/en/pub/hjse



Abstracted &amp; Indexed in:

TR Dizin Mühendislik ve Temel Bilimler Veri Tabanı |  
 CrossRef | Google Scholar | MIP Database | StuartxChange | ResearchBib | Scientific Indexing Services (SIS)

**HITTITE**  
JOURNAL OF SCIENCE & ENGINEERING

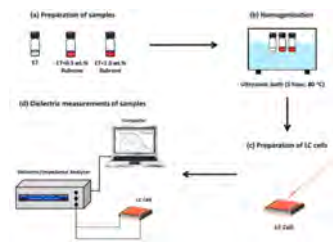
Volume 10, Issue 3, 2023

dergipark.org.tr/en/pub/hjse

*The Role of Rubrene Concentration on Dielectric Parameters of Nematic Liquid Crystals*

193-199  
 Gulsum Kocakulah

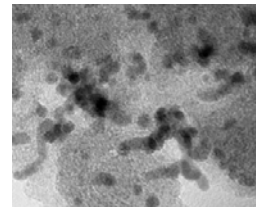
In this study, the dielectric parameters of E7 coded nematic liquid crystal (NLC) composites containing the different amounts of rubrene fluorescent dye were investigated. E7, E7+0.5 wt.% Rubrene, and E7+1.0 wt.% Rubrene samples were prepared.



*Electrochemical Dopamine Detection Using Palladium/Carbon Nano Onion Hybrids*

201-209  
 Hasan Huseyin Ipekci

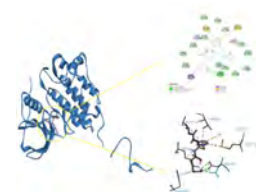
In the given study, palladium-decorated carbon nano-onion nanostructures (Pd/CNO) were used as an electrochemical catalyst for detecting dopamine (DA).



*Interaction of GHK Tripeptide with Receptors Targeted in Some Cancer Studies: A Theoretical Approach with Molecular Docking*

211-217  
 Bilge Bicak and Serda Kecel Gunduz

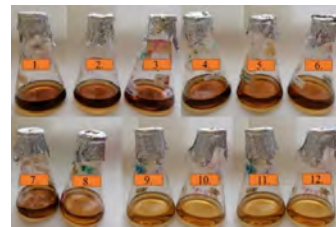
In this study, ER, PR, EGFR and HER2 receptors, which are among the most frequently used target receptors, were selected.



*Use of Heat-Killed Aspergillus Ochraceus NRRL 3174 Discs as Biosorbent for Petroleum Removal*

219-228  
 Nermin Hande Avcioglu, Sezen Bilen Ozyurek and Isil Seyis Bilkay

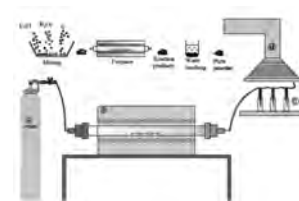
The purpose of this work was to evaluate the petroleum sorption capacity of heat-killed fungal discs obtained from Aspergillus ochraceus strain.



*Cobalt boride (Co2B) Particle Synthesis by One-step Carbothermic Reduction*

229-235  
 Levent Kartal

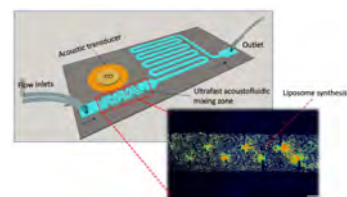
In this study, crystalline Co<sub>2</sub>B powder production was carried out by a one-step carbothermal reduction method starting from cheap, easily accessible oxide-based materials.



*Nanoscale Liposome Synthesis for Drug Delivery Applications via Ultrafast Acoustofluidic Micromixing*

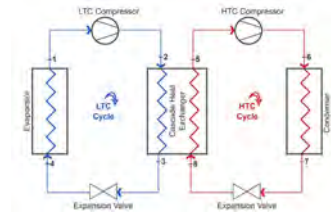
237-241  
 Ali Pourabdollah Vardin and Gurkan Yesiloz

In this work, we report an ultrafast acoustofluidic micromixer to synthesize liposome nanoparticles, which have been widely investigated in the literature as drug carriers due to their biocompatibility and biodegradability.



*Energy, Exergy, and Environment Performance Evaluation of Cascade Refrigeration System with Natural Refrigerants*  
 243-248  
 Meltem Kosan

In this study, two cascade systems consisting of R744/R290 (System 1) and R1270/R290 (System 2) natural refrigerant pairs were designed and thermodynamically examined.



*Investigation of Deep Learning Approaches for Identification of Important Wheat Pests in Central Anatolia*  
 249-257

Tolga Hayit and Sadik Eren Kose

This study employed various pre-trained deep learning approaches to identify key wheat pests in the Central Anatolia Region, namely *Aelia* spp., *Anisoplia* spp., *Eurygaster* spp., *Pachytychius hordei*, and *Zabrus* spp.



*On The Blind Denoising Efficiency of Image Denoising Algorithms Through Robustness, Image Quality and Computational Burden*  
 259-267

Kenan Gencol

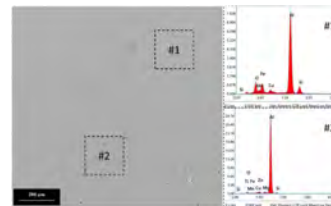
In this study, we assess the performance of the image denoising algorithms armored for these goals. We are aimed to determine the optimal performance yielded by such algorithms and the noise bounds wherein each algorithm is superior.



*Simultaneous Effect of Welding Current with Post-Weld T6 Heat Treatment on Corrosion Susceptibility of Al6013 Alloy Joined by GTAW*  
 269-277

Mehmet Topuz

Al6013 base metals were joined successfully with ER4047 weld metal by using the GTAW method under different welding currents.



**Owner**

Prof. Dr. Ali Osman ÖZTÜRK on behalf  
of Hitit University

**Editor-in-chief**

Prof. Dr. Ali KILIÇARSLAN

**Associate Editors**

Prof. Dr. D. Ali KÖSE

Assoc. Prof. Dr. Öncü AKYILDIZ

**Production**

Assoc. Prof. Dr. Kazım KÖSE

Res. Asst. Dr. Erhan ÇETİN

Res. Asst. Dr. Mustafa Reşit HABOĞLU

Res. Asst. Harun Emre KİRAN Res.

Asst. Ömer Faruk TOZLU

Lect. Tugrul YILDIRIM

**Editor's Office**

Tel: +90 364 227 45 33 / 12 36

Fax: +90 364 227 45 35

Email: alikilicarslan@hitit.edu.tr

**Subscription Service:**

Tel: +90 364 227 45 33 / 12 82

Fax: +90 364 227 45 35

Email: hjse@hitit.edu.tr

**EDITORIAL BOARD**

Prof. Dr. İftikhar AHMAD

Prof. Dr. Mike BECKETT

Prof. Dr. İbrahim DİNÇER

Prof. Dr. Ali ELKAMEL

Prof. Dr. Mohamad S QATU

Prof. Dr. Saffa RIFFAT

Prof. Dr. Thanos SALIFOLOU

Prof. Dr. Yuehong SU

Dr. Wojciech NOGALA

Prof. Dr. Yusuf AYVAZ

Prof. Dr. Adil DENİZLİ

Prof. Dr. Ali GENÇER

Prof. Dr. Metin GÜRÜ

Prof. Dr. Murat HOŞÖZ

Prof. Dr. Sadık KAKAÇ

Prof. Dr. Tarık Ömer OĞURTANI

Prof. Dr. Ender SUVACI

Prof. Dr. Ali TOPÇU

Prof. Dr. Kazım Savaş BAHÇECİ

Prof. Dr. Cengiz BAYKASOĞLU

Prof. Dr. Naki ÇOLAK

Prof. Dr. Vedat DENİZ

Prof. Dr. Hakan GÜNGÜNEŞ

Prof. Dr. Bülent KABAK

Prof. Dr. Ali KILIÇARSLAN

Prof. Dr. Dursun Ali KÖSE

Prof. Dr. İrfan KURTBAŞ

Prof. Dr. İbrahim SÖNMEZ

Assoc. Prof. Dr. Seyfi ŞEVİK

Prof. Dr. Dilber Esra YILDIZ

University of Malakand, Chakdara, Pakistan

Bangor University, Bangor, United Kingdom

Uoit Ontario University, Ontario, Canada

University of Waterloo, Ontario, Canada

Central Michigan University, Michigan, United States

The University of Nottingham, United Kingdom

Aristotle University of Thessaloniki, Thessaloniki, Greece

The University of Nottingham, United Kingdom

Polish Academy of Sciences, Poland

Suleyman Demirel University, Turkey

Hacettepe University, Turkey

Ankara University, Turkey

Gazi University, Turkey

Kocaeli University, Turkey

TOBB University, Turkey

Middle East Technical University, Turkey

Anadolu University, Turkey

Hacettepe University, Turkey

Hitit University, Turkey

Hitit University, Turkey

Hitit University, Turkey

Hitit University, Turkey

Hitit University, Turkey

Hitit University, Turkey

Hitit University, Turkey

Hitit University, Turkey

Hitit University, Turkey

Hitit University, Turkey

Hitit University, Turkey

Hitit University, Turkey

Journal Name	: HITTITE JOURNAL OF SCIENCE AND ENGINEERING
Year	: 2023
Managing Editor	: Prof. Dr. Ali KILIÇARSLAN
Managing Office	: Hitit University Faculty of Engineering
Managing Office Tel	: +90 364 227 45 33 / 12 36
Publication Language	: English
Publication Type	: Peer Reviewed, Open Access, International Journal
Delivery Format	: 4 times a year (quarterly)
Print ISSN	: 2149-2123
Online ISSN	: 2148-4171
Publisher Address	: Hitit Üniversitesi Kuzey Kampüsü Çevre Yolu Bulvarı 19030 Çorum / TÜRKİYE
Publisher Tel	: +90 364 227 45 33/1236



*As the team of Hittite Journal of Science and Engineering, we have published the new issue (2023-Volume 10, Issue 3). As a Editor in Chief, I am grateful to all our authors and contributing reviewers of this issue. I also would like to thank to the President of Hitit University, Prof. Dr. Ali Osman Öztürk, for his support and interest in HJSE and also to the Associate Editors of HJSE, namely Prof. Dr. Dursun Ali Kose and Assoc. Prof. Dr. Oncu Akyıldız, as well as our Production Editors Dr. Kazim Kose, Mustafa Reşit Haboğlu, Erhan Çetin, Tugrul Yıldırım, Harun Emre Kıran and Ömer Faruk Tozlu for their invaluable efforts in making of the journal.*

*The number of articles submitted to HJSE has been increasing, although I have announced in the previous issue (2023-Volume 10, Issue 2) that the articles within the scope of "Engineering", "Computer Science", "Food Science and Technology", "Materials Science" and the subcategories within this scope (listed in the submission section of HJSE) would be accepted for publication.*

*In this new issue, because of the important decision that we have taken in June 6, 2023, most of articles published are from the engineering discipline and related science such as material and computer science. But, there are still three articles from natural science such as physics because these articles had been submitted before June 6, 2023.*

*It's my pleasure to invite the researchers and scientists from all branches of engineering to join us by sending their best papers for publication in Hittite Journal of Science and Engineering.*

*Dr. Ali Kiliçarslan*

*Editor-in-Chief*

# The Role of Rubrene Concentration on Dielectric Parameters of Nematic Liquid Crystal

Gulsum Kocakulah 

<sup>R</sup>Duzce University, Department of Physics, Duzce, Turkiye

## ABSTRACT

In this study, the dielectric parameters of E7 coded nematic liquid crystal (NLC) composites containing the different amounts of rubrene fluorescent dye were investigated. E7, E7+0.5 wt.% Rubrene, and E7+1.0 wt.% Rubrene samples were prepared. Frequency dependent dielectric constants ( $\epsilon'$  and  $\epsilon''$ ), dielectric anisotropy ( $\Delta\epsilon'$ ), and ac conductivity ( $\sigma_{ac}$ ) graphs of rubrene doped E7 NLC composites were obtained by dielectric spectroscopy method and compared with pure E7 NLC. By using these graphs, relaxation frequency ( $f_R$ ), relaxation time ( $\tau_R$ ), dielectric strength ( $\delta\epsilon'$ ), and crossover frequency ( $f_c$ ) parameters of the E7 NLC and its rubrene doped composites were determined. An increase in  $f_R$  from 3.045 MHz to 3.697 MHz for 0 V and from 627 kHz to 686 kHz for 40 V was observed with increasing rubrene concentration. On the other hand, a decrease in  $\tau_R$  from 0.052  $\mu$ s to 0.043  $\mu$ s for 0 V and from 0.254  $\mu$ s to 0.232  $\mu$ s for 40 V was seen with increasing rubrene concentration. Furthermore, an increase in  $f_c$  from 1.145 MHz to 1.298 MHz was obtained with increasing rubrene concentration. The results show that the dielectric parameters change with the concentration of rubrene and it is thought that this study will provide a basis for investigating the dielectric properties of rubrene doped NLC composites. Moreover, it is concluded that the produced composites are a suitable base material for electro-optical device applications such as smart displays, photonics and electrical circuit elements.

### Keywords:

Dielectric anisotropy; Nematic liquid crystal; Relaxation frequency; Relaxation time; Rubrene

## INTRODUCTION

Liquid crystals (LCs) are known as materials whose properties are between isotropic liquid and anisotropic crystal [1-3]. This fascinating feature of LCs has attracted the attention of many research groups for broad applications in various fields of science and technology. This materials widely used in smart windows [4, 5], displays [6, 7], sensors [8, 9], and other electro-optical device applications. Especially, nematic liquid crystal (NLC) is technologically considerable phases within LCs and it is broadly used in the field of display [10-12]. The molecular orientation of NLCs is quite responsive to external stimuli like electric and magnetic fields [13, 14]. In recent years, the physical properties of NLCs can be also developed with several dopant materials such as polymers [15, 16], dyes [17, 18], and nanoparticles [19-21]. These dopant materials affect the molecular orientation of NLCs and can change their physical properties. Although there are studies examining the electro-optical and dielectric properties of dye doped NLC composites in the literature, the number of studies

investigating the dielectric properties of fluorescent dye doped NLCs is very few. Therefore, the use of fluorescent dye was preferred in order to observe the change in dielectric properties of E7 NLC in this research. Fluorescent dyes are defined as materials that both absorb and strongly emit in the visible region of the electromagnetic spectrum. Moreover, dyes with fluorescent properties are known as materials that distinguish from fluorescent brighteners that emit visible light but absorb ultraviolet [22]. The absorption characteristics of fluorescent dyes influence the orientation mechanisms of NLCs. Thus, the physical properties of LC based composites are significantly affected [23].

Rubrene, which is known as 5,6,11,12-tetraphenyl-naphthacene, is composed of tetracene backbone and four phenyl groups substituted at the 5, 6, 11, 12 positions. Rubrene powder is red or light brown and has strong absorption in the blue-violet to green spectrum [24]. Moreover, this fluorescent dye is important due to

### Article History:

Received: 2022/12/29

Accepted: 2023/06/17

Online: 2023/09/30

Correspondence to: Gulsum Kocakulah,

E-mail: gulsum.kocakulah@gmail.com,

Phone: +90 380 541 2404;

Fax: +90 380 541 2403

This article has been checked for similarity.



This is an open access article under the CC-BY-NC license

<http://creativecommons.org/licenses/by-nc/4.0/>

### Cite as:

G. KOCAKULAH, "The Role of Rubrene Concentration on Dielectric Parameters of Nematic Liquid Crystal" Hittite Journal of Science and Engineering, 10(3): 193–199, 2023. doi:10.17350/hjse19030000307

emission properties, electrical conductivity and mobility [25]. It is a p-type organic semiconductor with an emission wavelength of 550 nm [24, 26]. In addition, the carrier mobility in organic field effect transistors is quite high [27, 28]. Rubrene, which has unique physical and chemical properties, has been used in many electro-optical device applications such as field-effect transistors [29], organic light-emitting diodes [30], and solar cells [31, 32] until today.

This paper reports the effect of rubrene concentration on the dielectric parameters of E7 NLC. The frequency dependent dielectric parameters (dielectric constants:  $\epsilon'$  and  $\epsilon''$ , dielectric anisotropy:  $\Delta\epsilon'$ , and ac conductivity:  $\sigma_{ac}$ ) of pure and rubrene doped samples were investigated for Planar-state ( $V=0$  V) and Homeotropic-state ( $V=40$  V). In addition, relaxation frequency ( $f_R$ ), crossover frequency ( $f_C$ ), relaxation time ( $\tau_R$ ), and dielectric strength ( $\delta\epsilon'$ ) parameters of the samples were obtained using these data. The results showed that rubrene caused a significant change in dielectric parameters of E7 NLC.

## MATERIAL AND METHODS

The E7 NLC ( $n_o=1.521$  and  $n_e=1.746$ ) used in the experiment was purchased from Instec. This material consists of 4-cyano-4'-n-pentyl-biphenyl (5CB, 51 wt.%), 4-cyano-4'-n-heptyl-biphenyl (7CB, 25 wt.%), 4-cyano-4'-n-octyloxy-biphenyl (80CB, 16 wt.%), and 4-cyano-4'-n-pentyl-p-terphenyl (5CT, 8 wt.%). The phase transition temperature of E7 NLC nematic phase to isotropic phase ( $T_{N-I}$ ) is 60.5 °C. Rubrene fluorescent dye (sublimed grade and  $\lambda_{em}=550$  nm) was provided from Sigma Aldrich. The molecular formulas of the E7 and rubrene were given in Figure 1(a-b). Also, indium thin oxide (ITO) coated planar aligned LC cells has been used for the measurements and purchased from Instec. The 18  $\mu\text{m}$  spacer was used in the cells, and the surface resistance of the ITO coated glass plates was given as a 25  $\Omega/\text{cm}^2$ .

Schematic representation of the sample preparations and measurements procedure was given in Figure 2(a-d). Firstly, rubrene doped NLC composites were prepared with a concentration of 0.5 wt.% and 1.0 wt.% (Figure 2(a)). Then, composites was homogenised in an ultrasonic bath for 5 hour at 80 °C (Figure 2(b)). Finally, pure E7 NLC and rubrene doped E7 NLC composites were filled into the LC cells with the above specifications by capillary method (Figure 2(c)). Produced samples were coded as: E7, E7+0.5 wt.% Rubrene, and E7+1.0 wt.% Rubrene.

Dielectric parameters of pure and rubrene doped E7 NLC was determined with a computer-controlled Novo-control Alpha-A Dielectric/Impedance Analyzer between 1 kHz and 10 MHz with a test signal of 100 mV<sub>rms</sub> for 0 V and

40 V at room temperature (Figure 2(d)).

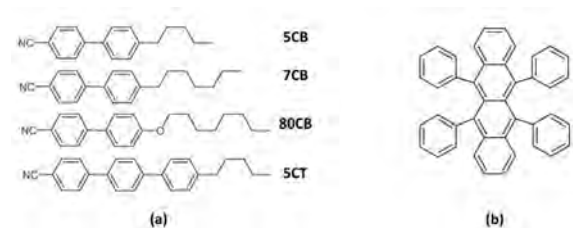


**Figure 1.** The molecular formula of the (a) E7 NLC and (b) Rubrene fluorescent dye.

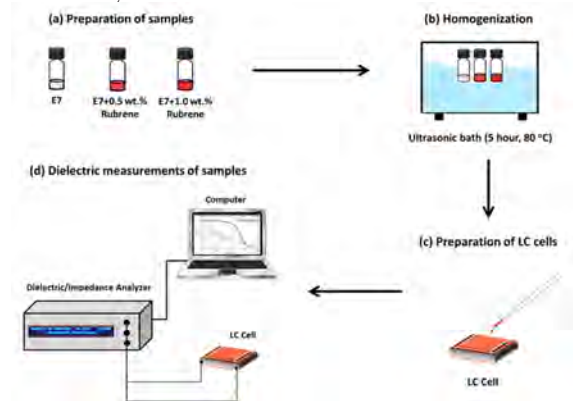


**Figure 2.** Schematic representation of the sample preparations and measurements.

## RESULTS AND DISCUSSION

Dielectric response of LC materials show complex behaviour and provides information about molecular polarizability and dipole moment when an electric field is applied. The complex dielectric constant acts as the most considerable parameter in determining the dielectric behaviour of LCs and is given by the following formula [33, 34]:

$$\epsilon^* = \epsilon' - i\epsilon'' \quad (1)$$

where,  $\epsilon'$  and  $\epsilon''$  is real and imaginary parts of the complex dielectric constant, respectively. Also,  $\epsilon'$  is energy stored in materials and defines as [35]:

$$\epsilon' = \frac{Cd}{\epsilon_0 A} = \frac{C}{C_0} \quad (2)$$

where, C is the capacitance and  $C_0$  is the capacitance of the free space. Also, d is the thickness and A is the area of the LC cell.  $\epsilon_0$  is dielectric constant of free space. Besides,  $\epsilon''$  denotes loss of energy in materials and defines as [35]:

$$\epsilon'' = \frac{Gd}{\omega\epsilon_0 A} = \frac{G}{\omega C_0} \quad (3)$$

where,  $\omega$  is the angular frequency and  $G$  is the conductance.

Figure 3(a-b) demonstrates the frequency dependent  $\epsilon'$  comparison graphs of the samples for 0 V and 40 V. Small changes occurred in  $\epsilon'$  value for both 0 V and 40 V depending on the increasing rubrene concentration. These small increases and decreases were seen in the low frequency regions. The reasons for these changes will be given in the explanations of Figure 4(a-b). Furthermore, in order to observe the voltage dependent  $\epsilon'$  values of the pure E7 NLC and rubrene doped E7 NLC composites, the frequency dependent  $\epsilon'$  variation graphs were given in Figure 3(c-e) for each sample. As seen in the figures, the  $\epsilon'$  parameters of all samples increased due to the increase in voltage. This increment can be clarified by the regular orientation of both LC and rubrene molecules in the electric field direction with changing voltage. Moreover, it is seen that the  $\epsilon'$  parameters of the samples at 0 V are almost the same 1 kHz-1 MHz frequency range, but decrease rapidly after 1 MHz. Therewithal, for 40 V, it is also observed that the  $\epsilon'$  parameter does not almost change in the 1 kHz-100 kHz frequency range for all samples and reduces after 100 kHz. The results show that samples will show relaxation after these frequency values.

The  $\epsilon'$ - $f$  comparison graphs of the samples at 1 kHz-10 kHz frequency range that changes depending on the rubrene concentration were given in Figure 4(a-b). The  $\epsilon'$  increased for E7+0.5 wt.% Rubrene while it decreased for E7+1.0 wt.% Rubrene. Some interactions are thought to occur in the composites when E7 NLC doped with rubrene: NLC-NLC, rubrene-rubrene and NLC-rubrene. The interactions between E7 NLC and rubrene dye molecules can be dipolar, electrostatic, and van der Waals. In this study,  $\epsilon'$  value increases in the low frequency region given in the graph for E7+0.5 wt.% Rubrene compared to pure E7 NLC for 0 V and 40 V. The reason for this behaviour is the increased dipole moment due to molecular interactions between NLC and rubrene. On the other hand, the number of domains in the composites decreases with increasing rubrene concentration. Thus, the distance between the domains increases and the dipole-dipole interactions decrease. For this reason,  $\epsilon'$  low for E7+1.0 wt.% Rubrene than for E7+0.5 wt.% Rubrene [36].

In Figure 5(a-b), the frequency dependent  $\epsilon''$  comparison graphs of the samples were given for 0 V and 40 V. Similar to the  $\epsilon'$  parameter, it is seen that small changes occur in  $\epsilon''$  values depending on the increasing rubrene concentration. In addition, it was desired to examine the  $\epsilon''$  variation graphs of the samples depending on both voltage and frequency, separately for each sample. For this reason, graphs of the variation of  $\epsilon''$  parameter with voltage were given in

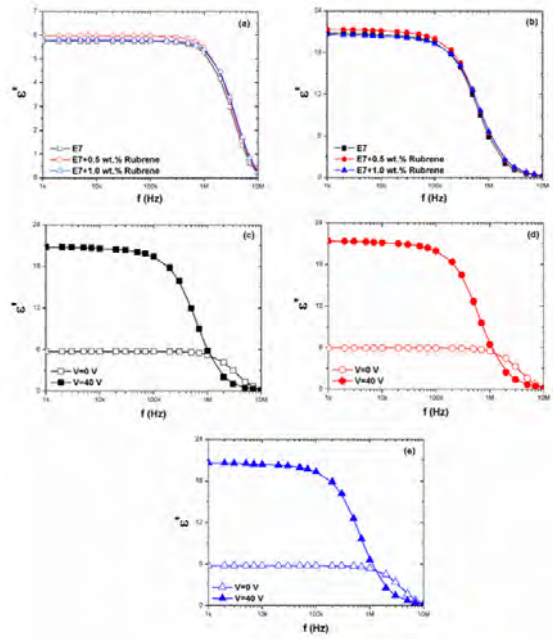


**Figure 3.**  $\epsilon'$ - $f$  comparison graphs of the samples (a)  $V=0$  V and (b)  $V=40$  V. Also,  $\epsilon'$ - $f$  single graphs of (c) E7, (d) E7+0.5 wt.% Rubrene, and (e) E7+1.0 wt.% Rubrene.

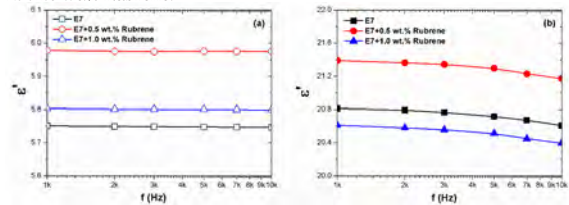


**Figure 4.**  $\epsilon'$ - $f$  comparison graphs of the samples at 1 kHz - 10 kHz frequency range for (a) 0 V and (b) 40 V.

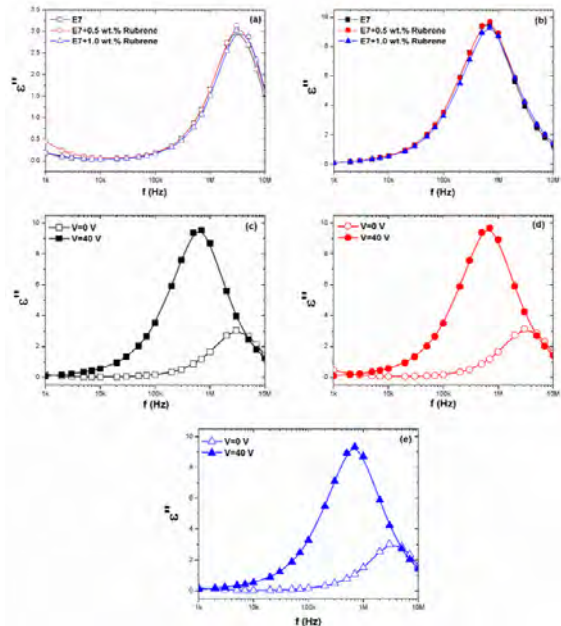


**Figure 5.**  $\epsilon''$ - $f$  comparison graphs of the samples (a)  $V=0$  V and (b)  $V=40$  V. Also,  $\epsilon''$ - $f$  single graphs of (c) E7, (d) E7+0.5 wt.% Rubrene, and (e) E7+1.0 wt.% Rubrene.



Figure 5(c-e) for pure E7 NLC and rubrene doped E7 NLC composites. It is seen that the  $\epsilon''$  values increase in all samples depending on the regular molecular arrangement with increasing voltage. Additionally, a single peak was observed between 1 kHz and 10 MHz for E7 NLC and its rubrene doped composites. This behaviour indicates that the samples have a single relaxation frequency in the examined frequency range. The relaxation frequency ( $f_r$ ) of the samples is determined using the frequencies corresponding to the peak points of the  $\epsilon''$ - $f$  graphs. The  $f_r$  values of E7 NLC and rubrene doped E7 NLC composites were given in Table 1. From the table, it is seen that the  $f_r$  increases with increasing rubrene concentration for 0 V and 40 V. The increase in  $f_r$  values of rubrene doped E7 NLC composites compared to pure E7 NLC may be owing to the increased availability of free space for molecular motion due to the presence of rubrene. Also, it is thought that the reduction in rotational viscosity with the addition of rubrene is also effective in the increase of  $f_r$  [37].

**Table 1.** Relaxation frequency ( $f_r$ ), relaxation time ( $\tau_r$ ), and dielectric strength ( $\delta\epsilon'$ ) parameters of the E7, E7+0.5 wt.% Rubrene, and E7+1.0 wt.% Rubrene for 0 V and 40 V.

	V=0 V			V=40 V		
	$f_r$ (MHz)	$\tau_r$ ( $\mu$ s)	$\delta\epsilon'$	$f_r$ (kHz)	$\tau_r$ ( $\mu$ s)	$\delta\epsilon'$
<b>E7</b>	3.045	0.052	5.581	627	0.254	20.679
<b>E7+0.5 wt.% Rubrene</b>	3.322	0.048	5.773	657	0.242	21.201
<b>E7+1.0 wt.% Rubrene</b>	3.697	0.043	5.541	686	0.232	20.409

The complex dielectric constant is also defined with Cole-Cole equation [38, 39]:

$$\epsilon^* = \epsilon'_\infty + \frac{\epsilon'_s - \epsilon'_\infty}{1 + (i\omega\tau_r)^{1-\alpha}} \quad (4)$$

where,  $\epsilon'_s$  is the low and  $\epsilon'_\infty$  is the high frequency limit of the  $\epsilon'$ ,  $\tau_r$  is relaxation time and  $\alpha$  is relaxation distribution parameter. If  $\alpha=0$ , the Cole-Cole model called as Debye model. In this case, the system has a single relaxation time. And if  $\alpha \neq 0$ , the relaxation behaviour fits non-Debye model and system has a more than one relaxation processes [40, 41].

Figure 6(a-b) indicates the Cole-Cole comparison graphs of E7 NLC and rubrene doped E7 NLC composites for 0 V and 40 V. Moreover, Cole-Cole graphs obtained at 0 V and 40 V for each sample were given in Figure 6(c-e). It has been observed that the samples almost complete the semi-circle and behave according to the Debye model. The  $\tau_r$  of

E7 NLC and rubrene doped E7 NLCs were calculated using the Cole-Cole plots and their values were given in Table 1. It is observed that the  $\tau_r$  increases in both E7 NLC and rubrene doped E7 NLC composites depending on the increasing voltage. The cause for this attitude is that the molecular orientation increases with increasing voltage, thus increasing the time it takes for LC and rubrene to return to their initial state. Besides, it is seen that  $\tau_r$  reduces with increasing rubrene concentration in E7 NLC for 0 V and 40 V. This behaviour can be explained by the fact that the trapping of free ions in the rubrene doped composites. As a result of the decrease in ion concentration, the viscosity of the composites decreases, thus the relaxation time of the system is also reduced [42]. This result is important in that E7 NLC doped with rubrene shows relaxation behaviour in a shorter time.

Dielectric strength ( $\delta\epsilon'$ ) is determined using the Cole-Cole graphs of the samples and calculated by the following equation [37, 41]:

$$\delta\epsilon' = \epsilon'_s - \epsilon'_\infty \quad (5)$$

The  $\delta\epsilon'$  values of the samples were given in Table 1. According to table,  $\delta\epsilon'$  of pure E7 NLC and rubrene doped E7 NLC composites increase depending on the voltage. The main reason for this increase is that  $\epsilon'_s$  increases with increasing voltage. According to the change in rubrene concentration, there is a small increase in E7+0.5 wt.% Rubrene and a small decrease in E7+1.0 wt.% Rubrene when compared with the  $\delta\epsilon'$  value of E7 NLC. The results indicate that rubrene concentration causes a change in the  $\delta\epsilon'$ .

Dielectric anisotropy ( $\Delta\epsilon'$ ) is the significant parameter for LC-based electro-optical devices and defined as the difference between parallel ( $\epsilon'_\parallel$ ) and perpendicular ( $\epsilon'_\perp$ ) components of the  $\epsilon'$  values [23, 38]:

$$\Delta\epsilon' = \epsilon'_\parallel - \epsilon'_\perp \quad (6)$$

In Figure 7, the frequency dependent  $\Delta\epsilon'$  change graph of the samples was given. It is seen from the graph that the  $\Delta\epsilon'$  value of E7+0.5 wt.% Rubrene increases slightly compared to E7 NLC at 1 kHz-100 kHz frequency range. In E7+1.0 wt.% Rubrene, it is observed that there is a small decrease in  $\Delta\epsilon'$  compared to E7 NLC in the same frequency range. In addition, the crossover frequency ( $f_c$ ) of the samples is determined using the  $\Delta\epsilon'$ - $f$  graph. The  $f_c$  values of E7, E7+0.5 wt.% Rubrene, and E7+1.0 wt.% Rubrene were determined in the 1 MHz-2 MHz frequency range where the  $\Delta\epsilon'$ - $f$  graph changed from positive to negative. Using the data inset of the graph, the  $f_c$  values of E7, E7+0.5 wt.% Rubrene, and E7+1.0 wt.% Rubrene were calculated as 1.145 MHz, 1.250

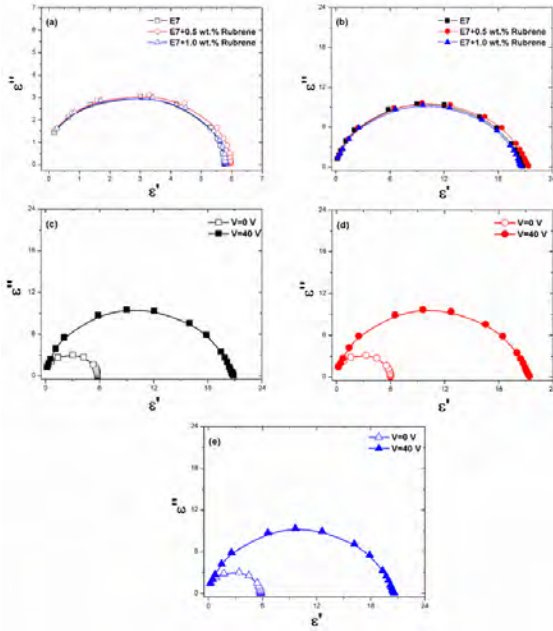


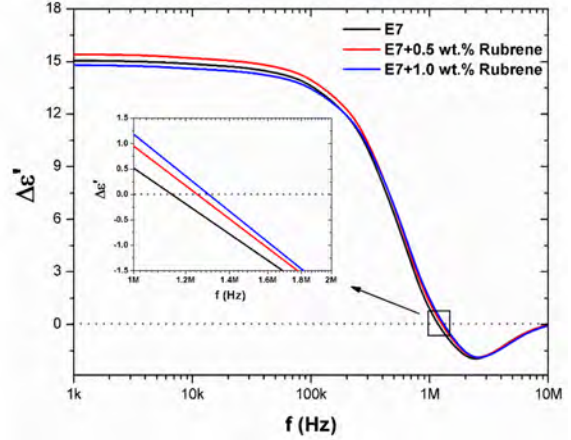
**Figure 6.** Cole-Cole comparison graphs of the samples (a)  $V=0$  V and (b)  $V=40$  V. Also, Cole-Cole single graphs of (c) E7, (d) E7+0.5 wt.% Rubrene, and (e) E7+1.0 wt.% Rubrene.

MHz and 1.298 MHz, respectively. According to the data, it can be seen that the  $f_c$  values of the rubrene doped E7 NLCs increased when compared to E7 NLC. In rubrene doped E7 NLCs, the interactions between rubrene and NLC molecules cause some changes in the molecular structure of the composite. Furthermore, these interactions change with increasing rubrene concentration. Depending on these changes, the interaction of the molecules with the longitudinal and transverse dipole moments in the electric field changes with frequency. Accordingly, it is thought that the increase in the  $f_c$  values of the rubrene doped composites is related to the change in the phase structure.

The ac conductivity of materials is given by the following equation [43, 44]:

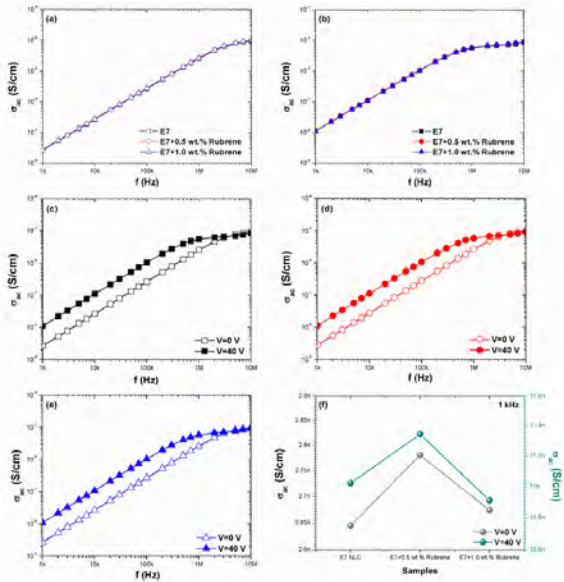
$$\sigma_{ac} = \epsilon_0 \omega \epsilon'' \quad (7)$$

Figure 8(a-b) depicts that frequency dependent  $\sigma_{ac}$  comparison graphs of the E7 NLC and its rubrene doped composites for 0 V and 40 V. The small increases and decreases in the  $\sigma_{ac}$  parameter of the samples with increasing rubrene concentration cannot be clearly seen from the graphs. However, it is seen that the  $\sigma_{ac}$  values of both E7 NLC and rubrene doped E7 NLC composites increase with increasing frequency for 0 V and 40 V. For a more detailed analysis,  $\sigma_{ac}$ - $f$  graphs for each sample were given in Figure 8(c-e). The  $\sigma_{ac}$  values increased with increasing voltage. Moreover, in Figure 8(f),  $\sigma_{ac}$  value of the samples at 1 kHz was given. As seen in the graph, there is a minor increment in the  $\sigma_{ac}$  of the



**Figure 7.**  $\Delta\epsilon'$ - $f$  graph of the E7, E7+0.5 wt.% Rubrene, and E7+1.0 wt.% Rubrene.

E7+0.5 wt.% Rubrene compared to the E7 NLC. This behaviour can be explained by the mobility of NLC and rubrene molecules. However, it is observed that the  $\sigma_{ac}$  value of the E7+1.0 wt.% Rubrene is quite close to the E7 NLC and is less than E7+0.5 wt.% Rubrene. This reduction may be related to the restriction caused by feeble aggregations in E7+1.0 wt.% Rubrene [11].



**Figure 8.**  $\sigma_{ac}$ - $f$  comparison graphs of the samples (a)  $V=0$  V and (b)  $V=40$  V. Also,  $\sigma_{ac}$ - $f$  single graphs of (c) E7, (d) E7+0.5 wt.% Rubrene, and (e) E7+1.0 wt.% Rubrene. And (f)  $\sigma_{ac}$  value of the samples at 1 kHz.

## CONCLUSION

In the current study, the dielectric parameters of rubrene doped E7 NLC were investigated. In order to observe the rubrene effect, two different concentrations were used and the dielectric parameters of the produced E7+0.5 wt.% Rubrene and E7+1.0 wt.% Rubrene composites were

compared with the pure E7 NLC. Dielectric measurements were carried out at 0 V and 40 V, depending on the frequency. As a result of the experimental evaluations, it was concluded that  $f_r$  increases and  $\tau_r$  decreases with increasing rubrene concentration in E7 NLC. In addition, it was observed that the frequency dependent  $\Delta\epsilon'$  of the samples were quite close to each other and  $f_c$  was calculated from the  $\Delta\epsilon'$ -f graphs. It was found that the  $f_c$  increased with rubrene concentration in E7 NLC. Accordingly, rubrene doped E7 NLCs will be considerable for the production of electro-optical devices with low relaxation time that can operate in the high frequency region.

## CONFLICT OF INTEREST

The authors declare that they have no known competing financial interests or personal relationships that could have appeared to influence the work reported in this paper.

## REFERENCES

1. Varshney D, Anu, Prakash J, Singh VP, Yadav K, Singh G. Probing the Impact of Bismuth-titanate Based Nanocomposite on the Dielectric and Electro-Optical Features of a Nematic Liquid Crystal Material. *Journal of Molecular Liquids*. 2022;347:118389.
2. Mani S, Patwardhan S, Hadkar S, Mishra K, Sarawade P. Effect of Polymer Concentration on Optical and Electrical Properties of Liquid Crystals for Photonic Applications. *Materials Today: Proceedings*. 2022;62:7035-7039.
3. Mishra R, Hazarika J, Hazarika A, Gogoi B, Dubey R, Bhattacharjee D, Singh KN, Alapati PR. Dielectric Properties of a Strongly Polar Nematic Liquid Crystal Compound Doped with Gold Nanoparticles. *Liquid Crystals*. 2018;45(11):1661-1671.
4. Oh SW, Ji SM, Han CH, Yoon TH. A Cholesteric Liquid Crystal Smart Window with a Low Operating Voltage. *Dyes and Pigments*. 2022;197:109843.
5. Jinqian L, Zhao Y, Gao H, Wang D, Miao Z, Cao H, Yang Z, He W. Polymer Dispersed Liquid Crystals Doped with CeO<sub>2</sub> Nanoparticles for the Smart Window. *Liquid Crystals*. 2022;49(1):29-38.
6. Li YL, Li NN, Wang D, Chu F, Lee SD, Zheng YW, Wang QH. Tunable Liquid Crystal Grating Based Holographic 3D Display System with Wide Viewing Angle and Large Size. *Light: Science & Applications*. 2022;11:188.
7. Tan G, Huang Y, Li MC, Lee SL, Wu ST. High Dynamic Range Liquid Crystal Displays with a Mini-LED Backlight. *Optics Express*. 2018;26(13):16572-16584.
8. Mulder DJ, Schenning APHJ, Bastiaansen CWM. Chiral-Nematic Liquid Crystals as One Dimensional Photonic Materials in Optical Sensors. *Journal of Materials Chemistry C*. 2014;2:6695-6705.
9. Cachelin P, Green JP, Peijs T, Heeney M, Bastiaansen CWM. Optical Acetone Vapor Sensors Based on Chiral Nematic Liquid Crystals and Reactive Chiral Dopants. *Advanced Optical Materials*. 2016;4(4):92-596.
10. Pathak G, Hegde G, Prasad V. Investigation of Electro-Optical and Dielectric Properties of Nematic Liquid Crystal Dispersed with Biowaste Based Porous Carbon Nanoparticles: Increased Birefringence for Display Applications. *Journal of Molecular Liquids*. 2020; 314:113643.
11. Yadav G, Kumar M, Srivastava A, Manohar R. SiO<sub>2</sub> Nanoparticles Doped Nematic Liquid Crystal System: An Experimental Investigation on Optical and Dielectric Properties. *Chinese Journal of Physics*. 2019;57:82-89.
12. Özgün Ş, Eskalen H, Tapkıranlı Y. The Electrical and Optical Behavior of Graphene Oxide Doped Nematic Liquid Crystal. *Journal of Materials Science: Materials in Electronics*. 2022;33:5720-5729.
13. Yadav G, Agrahari K, Manohar R. Multiwall Carbon Nanotube-Nematic Liquid Crystal Composite System: Preparation and Characterization. *Journal of Dispersion Science and Technology*. 2021;42(5):707-714.
14. Varshney D, Parveen A, Prakash J. Effect of Cobalt Oxide Nanoparticles on Dielectric Properties of a Nematic Liquid Crystal Material. *Journal of Dispersion Science and Technology*. 2022;43(1):42-49.
15. Pandey S, Gupta SK, Singh DP, Vimal T, Tripathi PK, Srivastava A, Manohar R. Effects of Polymer Doping on Dielectric and Electro-Optical Parameters of Nematic Liquid Crystal. *Polymer Engineering & Science*. 2015;55(2):414-420.
16. Kim Y, Jung D, Jeong S, Kim K, Choi W, Seo Y. Optical Properties and Optimized Conditions for Polymer Dispersed Liquid Crystal Containing UV Curable Polymer and Nematic Liquid Crystal. *Current Applied Physics*. 2015;15(3):292-297.
17. Eskalen H, Özgün Ş, Okumuş M, Kerl S. Thermal and Electro-Optical Properties of Graphene Oxide/Dye-Doped Nematic Liquid Crystal. *Brazilian Journal of Physics*. 2019;49: 341-347.
18. Ye L, Hou C, Lv C, Zhao C, Yin Z, Cui Y, Lu Y. Tailoring of Random Lasing Characteristics in Dye-Doped Nematic Liquid Crystals. *Applied Physics B*. 2014;115:303-309.
19. Chemingui M, Singh UB, Yadav N, Dabrowski RS, Dhar R. Effect of Iron Oxide ( $\gamma$ -Fe<sub>2</sub>O<sub>3</sub>) Nanoparticles on the Morphological, Electro-Optical and Dielectric Properties of a Nematic Liquid Crystalline Material. *Journal of Molecular Liquids*. 2020;319:114299.
20. Praseetha KP, Shiju E, Chandrasekharan K, Varghese S. Intense Nonlinear Optical Properties of ZnS Quantum Dot Doped Nematic Liquid Crystal Compounds. *Journal of Molecular Liquids*. 2021;328:115347.
21. Elkhaldi HHM, Khandka S, Singh UB, Pandey KL, Dabrowski R, Dhar R. Dielectric and Electro-Optical Properties of a Nematic Liquid Crystalline Material with Gold Nanoparticles. *Liquid Crystals*. 2018;45(12):1795-1801.
22. Christie RM. Handbook of Textile and Industrial Dyeing Principles, Processes and Types of Dyes. Volume 1 in Woodhead Publishing Series in Textiles; 2011. p. 562-587.
23. Pathak G, Agrahari K, Yadav G, Srivastava A, Strzeczysz O, Manohar R. Tuning of Birefringence, Response Time, and Dielectric Anisotropy by the Dispersion of Fluorescent Dye into the Nematic Liquid Crystal. *Applied Physics A*. 2018;124:463.
24. Liu S, Wu H, Zhang X, Hu W. Research Progress of Rubrene as an Excellent Multifunctional Organic Semiconductor. *Frontiers of Physics*. 2021;16(1):13304.
25. Al-Muntaser AA, Alamri HR, Sharma K, Eltahir S, Makhlof MM. Role of Rubrene Additive for Reinforcing the Structural, Optical, and Dispersion Properties of Polyvinyl Alcohol Films Towards Optoelectronic Applications. *Optical Materials*. 2022;128:112465.
26. Selvaraj P, Li P-Y, Antony M, Wang Y-W, Chou P-W, Chen Z-H, Hsu C-J, Huang C-Y. Rubbing-Free Liquid Crystal Electro-Optic Device Based on Organic Single-Crystal Rubrene. *Optics Express*. 2022;30(6):9521-9533.
27. Ma H, Liu N, Huang J-D. A DFT Study on the Electronic Structures and Conducting Properties of Rubrene and Its Derivatives in Organic Field-Effect Transistors. *Scientific Reports*. 2017;7:331.

28. Podzorov V, Menard E, Rogers JA, Gershenson ME. Hall Effect in the Accumulation Layers on the Surface of Organic Semiconductors. *Physical Review Letters*. 2005;95(22): 226601.
29. Kim K, Kim MK, Kang HS, Cho MY, Joo J, Kim JH, Kim KH, Hong CS, Choi DH. New Growth Method of Rubrene Single Crystal for Organic Field-Effect Transistor. *Synthetic Metals*. 2007;157(10-12):481-484.
30. Wang X, Wang R, Zhou D, Yu J. Study of Organic Light-Emitting Diodes with Exciplex and Non-Exciplex Forming Interfaces Consisting of an Ultrathin Rubrene Layer. *Synthetic Metals*. 2016;214:50-55.
31. Pelicano CM, Yanagi H. Effect of Rubrene:P3HT Bilayer on Photovoltaic Performance of Perovskite Solar Cells with Electrodeposited ZnO Nanorods. *Journal of Energy Chemistry*. 2018;27(2):455-462.
32. Huang J, Yu J, Wang W, Jiang Y. Organic Solar Cells with a Multicharge Separation Structure Consisting of a Thin Rubrene Fluorescent Dye for Open Circuit Voltage Enhancement. *Applied Physics Letters*. 2011;98:023301.
33. Nasri R, Missaoui T, Hbib A, Soltani T. Enhanced Dielectric Properties of Nematic Liquid Crystal Doped with Ferroelectric Nanoparticles. *Liquid Crystals*. 2021;48(10):1429-1437.
34. Jain AK, Deshmukh RR. Effects of Dye Doping on Electro-Optical, Thermo-Electro-Optical and Dielectric Properties of Polymer Dispersed Liquid Crystal Films. *Journal of Physics and Chemistry of Solids*. 2022;160:110363.
35. Tüzün Özmen Ö, Goksen K, Demir A, Durmus M, Köysal O. Investigation of Photoinduced Change of Dielectric and Electrical Properties of Indium (III) Phthalocyanine and Fullerene Doped Nematic Liquid Crystal. *Synthetic Metals*. 2012;162(24):2188-2192.
36. Pathak G, Agrahari K, Roy A, Srivastava A, Strzezysz O, Garbat K, Manohar R. Dispersion of Fluorescent Dye in the Nematic Liquid Crystal: Enhanced Photoluminescence and High Birefringence. *Opto-Electronics Review*. 2018;26:317-324.
37. Mishra S, Sontakke AM, Gupta RK, Kumar S, Manjuladevi V. Dielectric Spectroscopy Studies of Silver Nanorod Doped Nematic Liquid Crystal. *Materials Today: Proceedings*. 2022;50:2587-2591.
38. Manohar R, Pandey KK, Srivastava AK, Misra AK, Yadav SP. Sign Inversion of Dielectric Anisotropy in Nematic Liquid Crystal by Dye Doping. *Journal of Physics and Chemistry of Solids*. 2010;71:1311-1315.
39. Pandey KK, Bawaria AK, Priyadarshi P. Effect of Nano Particles on the Dielectric Anisotropy of Liquid Crystal. *Journal of Scientific Research and Advances*. 2015;2(3):103-107.
40. Deshmukh RR, Jain AK. The Complete Morphological, Electro-Optical and Dielectric Study of Dichroic Dye-Doped Polymer-Dispersed Liquid Crystal. *Liquid Crystals*. 2014; 41(7):960-975.
41. Deshmukh RR, Jain AK. Effect of Anti-Parallel and Twisted Alignment Techniques on Various Properties of Polymer Stabilised Liquid Crystal (PSLC) Films. *Liquid Crystals*. 2016;43(4):436-447.
42. Salah MB, Nasri R, Alharbi AN, Althagafi TM, Soltani T. Thermotropic Liquid Crystal Doped with Ferroelectric Nanoparticles: Electrical Behavior and Ion Trapping Phenomenon. *Journal of Molecular Liquids*. 2022;357:119142.
43. Jayoti D, Khushboo, Malik P, Singh A. Effect of Polymer Concentration on Morphology, Dielectric and Optical Properties in a Polymer-Dispersed Ferroelectric Liquid Crystal. *Liquid Crystals*. 2016;43(5):623-631.
44. Vimal T, Agrahari K, Sonker RK, Manohar R. Investigation of Thermodynamical, Dielectric and Electro-Optical Parameters of Nematic Liquid Crystal Doped with Polyaniline and Silver Nanoparticles. *Journal of Molecular Liquids*. 2019;290:111241.



# Electrochemical Dopamine Detection Using Palladium/Carbon Nano Onion Hybrids

Hasan Huseyin Ipekci<sup>1,2</sup> 

<sup>1</sup>Necmettin Erbakan University, Department of Metallurgical and Materials Engineering, Konya, Türkiye

<sup>2</sup>Necmettin Erbakan University, BITAM, Konya, Türkiye

## ABSTRACT

In the given study, palladium-decorated carbon nano-onion nanostructures (Pd/CNO) were used as an electrochemical catalyst for detecting dopamine (DA). The physicochemical properties of the Pd/SO<sub>3</sub>H/CNO-based catalysts were studied by transmission electron microscopy (TEM), scanning electron microscopy (SEM), X-ray diffraction (XRD), and X-ray photoelectron spectroscopy (XPS) methods. Pd/SO<sub>3</sub>H/CNO inks were dropped cast on a glassy carbon electrode (GCE) to prepare the electrochemical DA sensors. The sensor performance was performed using cyclic voltammetry (CV), differential pulse voltammetry (DPV), and electrochemical impedance spectroscopy (EIS). The electroanalytical results indicated a LOD value of 2.44 μM and the linear range of the sensors were found to be between 10 and 400 μM DA. The enhanced electrocatalytic activity toward DA is attributed to the high active surface area, conductivity of CNO and the high electrocatalytic property of Pd. The results suggest that Pd/SO<sub>3</sub>H/CNO nanostructures can be used to detect electrochemical DA sensors with high selectivity, sensitivity, and low LOD.

## Keywords:

Carbon nano-onion; Palladium; Electrochemical sensor; Dopamine; Differential pulse voltammetry

## INTRODUCTION

Carbon and its allotropes have gained tremendous attention in electrochemical sensing applications owing to their chemical stability, high electrocatalytic activity, biocompatibility, conductivity, low cost, and large surface areas [1, 2]. So far, carbon-related materials including carbon black, carbon nanotubes (CNT), graphene, graphene oxide, amorphous carbon, and carbon nano-onion (CNO) have been used as the sensing materials for different molecules. Among these, CNO shows great potential for electrochemical applications due to having the structure of multiple concentric shells of fullerenes, quasi-spherical and polyhedral-shaped layers. The distance between the polyhedral-shaped layers ranges from 3 to 50 nm [3]. CNOs demonstrate unique chemical and physical properties, such as good biocompatibility, low toxicity, high electronic conductivity, and thermal stability. Besides, the tolerability of the surface functional groups renders the CNO structures highly dispersible in aqueous solutions. CNO and its derivatives have been used in different electrochemical applications such as energy storage [4], bioimaging [5], magnetic storage media [6], fuel cell electrodes [7], and sensing and biomedical applications [8]. For the

case of electrochemical sensing applications, various reports have shown the applicability of CNO-based materials against the detection of different molecules such as glucose [9, 10], dopamine [11, 12] cysteine; methionine [13] epinephrine, and norepinephrine [12], phenoxy herbicides [14].

Although pristine carbon allotropes show electrochemical activity to some extent, the pristine structure does not yield a high electrochemical activity compared to metal and metal oxide-based electrocatalysts. One of the most effective methods to achieve enhanced electrochemical performance in carbon-based catalysts is the decoration of the carbon surface with metal nanoparticles (MNPs). Some MNPs reported in the literature are Ag [15, 16], Pt [17–19], Pd [20, 21], and Au [22]. The incorporation of MNPs in the catalyst structures boosts the electrochemical activity of the electrochemical sensors significantly. MNPs anchored on the carbon surface facilitate electron transfer and can act as electron transfer mediators, which leads to enhanced electrochemical performance. Pd is one of the most exploited noble metals to decorate the carbon surface for enhanced electrochemical activity in different electrochemi-

## Article History:

Received: 2023/01/13

Accepted: 2023/07/05

Online: 2023/09/30

**Correspondence to:** Hasan Huseyin Ipekci, Necmettin Erbakan University, Metallurgical and Materials Engineering, 42090, Konya, TÜRKİYE

E-Mail: hhipekci@erbakan.edu.tr, hsnpkc@gmail.com;

This article has been checked for similarity.



This is an open access article under the CC-BY-NC licence

<http://creativecommons.org/licenses/by-nc/4.0/>

## Cite as:

Ipekci H I, "Electrochemical Dopamine Detection Using Palladium/Carbon Nano Onion Hybrids". Hittite Journal of Science and Engineering 2023;10(3): 201–209.  
doi: 10.17350/hjse19030000308

cal applications such as energy storage [23], medicine [24], oxygen reduction [25], sensing [26] and waste treatment [27].

Dopamine (DA) is a bioactive molecule that plays vital roles in the human body and is a neurotransmitter for the messaging cognitive function and diseases in the central and peripheral nervous system. Hence, the DA level in the blood is the indicator of various diseases, and its detection with high selectivity and sensitivity is of great importance. While a low DA level in the human brain can cause schizophrenia, addiction [28], depression [29], and diseases such as Parkinson's [30] and Alzheimer's [31], a high level of DA may cause hypertension, drug addiction, and heart failure [32]. The level of DA has been determined using conventional methods including colorimetric [33], fluorescence [34], chromatography [35] and electrochemical methods. Those conventional methods, however, pose disadvantages such as complicated sample pre-treatments, time-consuming testing procedures, and the requirement of expensive equipment. Therefore, electrochemical sensors are of great importance because of the advantages of easy operation and low cost, fast response, high stability and selectivity [36]. Brezcko et al. detected DA using CNO/PDDA (poly(diallyl dimethylammonium chloride) nanocomposite in a range of  $5 \times 10^{-5}$  and  $4 \times 10^{-3}$  mol/L [11]. A screen-printed electrode was constructed with CNO and graphite mixture ink and the sensor detected dopamine in the linear range from 10  $\mu$ M to 99.9  $\mu$ M, and the lowest detection concentration was 0.92  $\mu$ M [37]. Carbon nano-onions and their derivatives have been exploited to detect DA electrochemically [12, 38].

The given work depicts the preparation of Pd/SO<sub>3</sub>H/CNO nanocomposites to develop electrochemical DA sensors with high sensitivity and selectivity. Pd nanoparticles were precipitated on the SO<sub>3</sub>H-modified CNO surface using a facile chemical precipitation method. The decoration of CNO surface with SO<sub>3</sub>H groups prevent the agglomeration of the nanoparticles due to acting as a nucleation agent. In the given work, Pd-decorated SO<sub>3</sub>H/CNO nanohybrids were exploited to construct electrochemical DA sensors, for the first time in the literature. The physicochemical properties of the catalysts were studied using TEM, SEM, XPS, XRD, Raman, and FTIR methods. CV and DPV were used to determine the electrochemical performance of Pd/SO<sub>3</sub>H/CNO against DA for sensitivity, selectivity, storage stability, repeatability, and applicability of the sensors in real samples.

## EXPERIMENTAL

### Chemicals

CuCl<sub>2</sub>\*2H<sub>2</sub>O (99%) and CaC<sub>2</sub> (75%) were purchased from Merck an NH<sub>3</sub>\*H<sub>2</sub>O (28%-30%), NaBH<sub>4</sub> (96%), K<sub>2</sub>PdCl<sub>4</sub>, chloroform, Nafion (5 wt.%), and dopamine were purchased from Sigma-Aldrich. The interferents molecules

(hydrogen peroxide, glucose, uric acid, and ascorbic acid) were obtained from Sigma. No additional treatment was applied to the chemicals.

### Synthesis of CNO, SO<sub>3</sub>H/CNO, and Pd/SO<sub>3</sub>H/CNO

Carbon nano-onions were prepared based on a study reported by Han et al. [39]. Briefly; CuCl<sub>2</sub>\*2H<sub>2</sub>O (0.059 mol) and CaC<sub>2</sub> (0.05 mol) were placed in a 30 ml stainless steel autoclave and left in an oven which was hold at 600°C for 10 h. The obtained product was washed with NH<sub>3</sub>\*H<sub>2</sub>O and chloroform to remove the copper residues. After that, the obtained carbon phase was rigorously washed with deionized water and ethanol and left for drying in a vacuum oven overnight. The surface of the obtained CNO powder was modified with SO<sub>3</sub>H groups to enhance the distribution of Pd nanoparticles. It should be emphasized that SO<sub>3</sub>H groups on the carbon surface act as nucleation agents for Pd NPs, which results in an enhancement in the homogeneous distribution of MNPs on the surface [40, 41]. Within this aim, the CNO surface was furnished with SO<sub>3</sub>H groups using a method explained as follows. 1 g of sulfonic acid (99%, Sigma) was dissolved in a solution containing NaOH (2 wt.%), then 0.4 g of sodium nitrate was introduced. After homogenization, the obtained solution was added slowly into 10 ml ultrapure water at ice temperature (0°C) and kept stirring for 30 min. After that, the solution was slowly added to the 30 mL CNO/DI water suspension in an ice bath and stirred for another 5 h. The modified CNO structures were centrifuged, washed with DI, and dried in a vacuum oven. Pd nanoparticles were anchored on SO<sub>3</sub>H/CNO surfaces using a method reported in a previous study [42]. Briefly, a certain amount of SO<sub>3</sub>H/CNO was dispersed in DI containing K<sub>2</sub>PdCl<sub>4</sub> at 55°C for 12 h. Then, freshly prepared NaBH<sub>4</sub> was slowly added to the solution dropwise and Pd nanoparticles were allowed to precipitate on the nanocarbon surface. Solid phase was removed from the liquid phase by centrifugation and dried.

### Characterization of CNO, SO<sub>3</sub>H/CNO and Pd/SO<sub>3</sub>H/CNO

X-ray diffraction (XRD) was used for phase identification by using Rigaku Ultims-IV equipped with Cu K $\alpha$  ( $\lambda=0.15406$  nm) radiation. The diffraction pattern was scanned over 20°–90° 2 $\theta$ , at a scanning speed of 1° 2 $\theta$ /min. The average size and distribution of Pd nanoparticles deposited on carbon nano-onion structures were determined using transmission electron microscopy (TEM, FEI @ 200kV). Morphology, surface properties, and elemental analysis (EDS) of nanostructures were determined by scanning electron microscopy (Zeiss Gemini SEM 500,

SEM). Additionally, the bond structures and the oxidation states of the nanostructures were determined by X-ray photoelectron spectroscopy (XPS, PHI 5000 VersaProbe).

### Preparation of the sensor, electrochemical analyses

The catalyst inks were composed by mixing a certain amount of obtained powder, Nafion solution (5% v/v, 30  $\mu$ l), DI water (0.6 ml), and ethanol (0.4 ml). To homogenize the ink, an ultrasonic bath and probe were used. Before the application of the ink slurries on the GC surface (3mm in diameter), the electrode surface was polished with alumina slurry. The surface of the GC was covered with 5  $\mu$ l of the ink and left for drying. To form a permselective membrane on the sensor surface and improve the stability of the sensors, Nafion solution (0.05 wt.%) was dropped on the Pd/SO<sub>3</sub>H/CNO -modified GC surface. Electrochemical measurements were performed using an Emstat3 Blue (Netherlands) potentiostat. A Pt plate was used as the counter electrode and the reference electrode was Ag/AgCl. In the electrochemical experiments, 0.1 M PBS buffer was used as the electrolyte. Determination of DA was carried out by CV and DPV methods. EIS analysis was performed using a PalmSens 4 potentiostat in an electrolyte containing 5 mM K<sub>3</sub>[Fe(CN)<sub>6</sub>]/ K<sub>4</sub>[Fe(CN)<sub>6</sub>] in 0.1 M KCl. The DPV analysis was carried out between -0.4 and 0.8 V with a pulse amplitude of 25 mV, a pulse width of 70 ms, and a scan rate of 25 mV/s. Frequency range of 82500 and 0.05 Hz was chosen as the EIS para-

eters and the data were recorded with a pulse amplitude of 5mV by using PalmSens4.

## RESULT AND DISCUSSION

### Characterization of the CNO and Pd/SO<sub>3</sub>H/CNO

Representative TEM images of the as-synthesized CNO samples are given in Fig. 1. The images indicated the formation of the carbon structure after the heat treatment of CuCl<sub>2</sub>\*2H<sub>2</sub>O and CaC<sub>2</sub>. The high-magnification TEM image (Fig. 1b) showed carbon fringes and when the obtained results were compared with the literature, it can be suggested that CNO nanoparticles were successfully synthesized. The TEM images of the Pd-modified SO<sub>3</sub>H/CNO structures are also given in Fig. 1c-d. The images suggest that Pd nanoparticles were evenly distributed on SO<sub>3</sub>H/CNO surface without any severe agglomeration. As discussed earlier, the modification of the CNO surface with SO<sub>3</sub>H functionalities improved the Pd distribution, preventing the agglomeration of the MNPs. Additionally, small Pd nanoparticles (< 10 nm) were anchored on the carbon surface.

XRD was used to determine the phase analysis and the recorded XRD diffractograms are displayed in Fig. 2a. The XRD peaks appearing at about the 2 $\theta$  values of 40.3°, 46.6°, 68.2°, and 82.3° are responsible for the planes of (111), (200), (220), and (311), respectively in the face-centered cubic Pd nanoparticles. In addition to metallic Pd, the oxide form

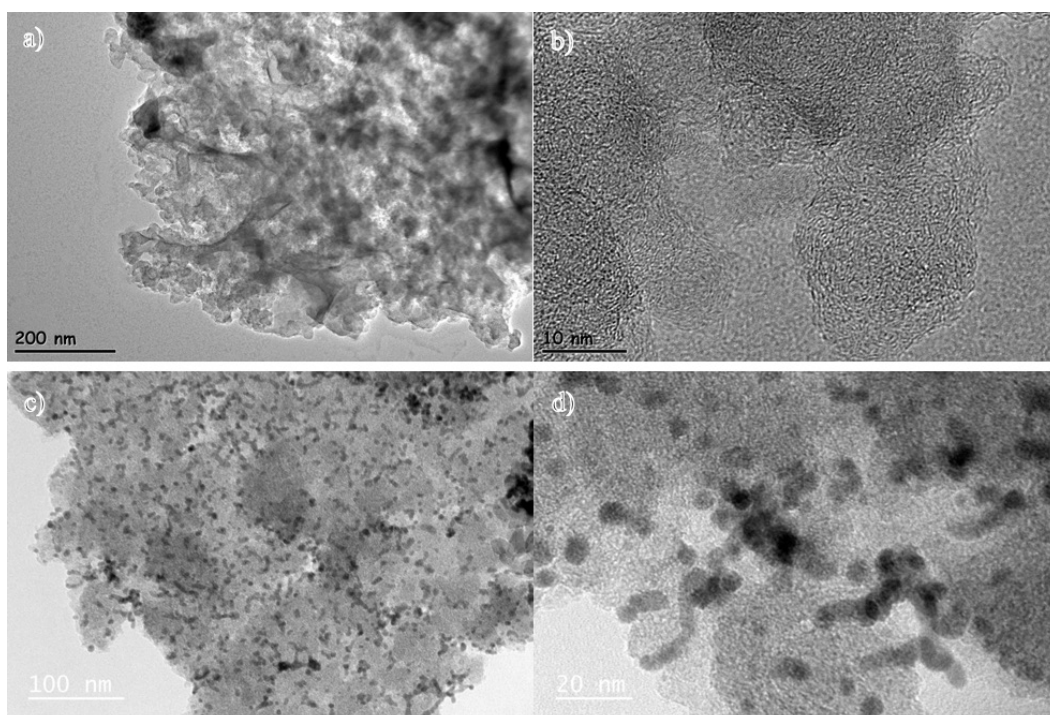


**Figure 1.** TEM images of CNO (a-b) and Pd/SO<sub>3</sub>H/CNO (c-d) at different magnifications.



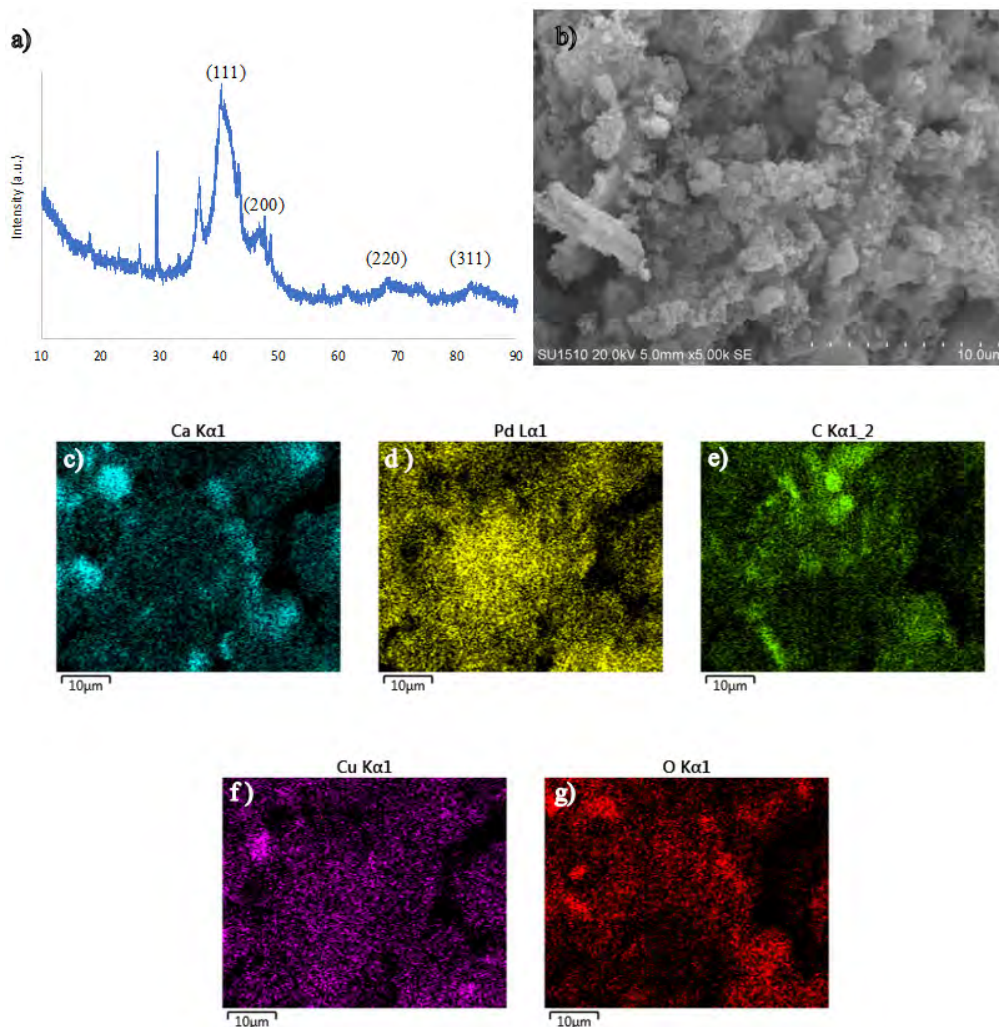


**Figure 2.** The XRD and SEM results of Pd/SO<sub>3</sub>H/CNO.

of Pd (PdO), was observed in the structure, which was also confirmed by the XPS results. The XRD reflections observed at ca. 36.5°, 41.9°, 57.8°, and 60.3° correspond to the presence of the oxide form of Pd nanoparticles. The chemical analysis and the surface morphology of the samples were studied using SEM and EDS methods. The representative SEM image given in Fig. 2b indicates the three-dimensional surface morphology of the samples, which is essential for improved electrochemical activity and enlarged electrochemical active surface area. Furthermore, the elemental analysis results indicated that (Fig. 2c-g) suggested the homogeneous distribution of the Pd nanoparticles on the CNO surface. The presence of the S element, which originated from the sulfonate groups anchored on the CNO surface, was not observed from the EDS results, which may be attributed to the low S content on the CNO surface.

The surface chemistry of the Pd/SO<sub>3</sub>H/CNO samples was studied using XPS analyses. The XPS results indicated O, C, Pd, S, and Cu elements on the sample surface (Fig. 3).

As discussed earlier, the presence of Cu is attributed to the starting materials used to synthesize the CNO powder. Although the CNO samples were washed rigorously, residual Cu could not be removed from the sample. While EDS results did not show the S element on the CNO surface, the XPS results revealed the S element with 1.78 at. % ratio, confirming the successful modification of the CNO surface with SO<sub>3</sub>H groups.

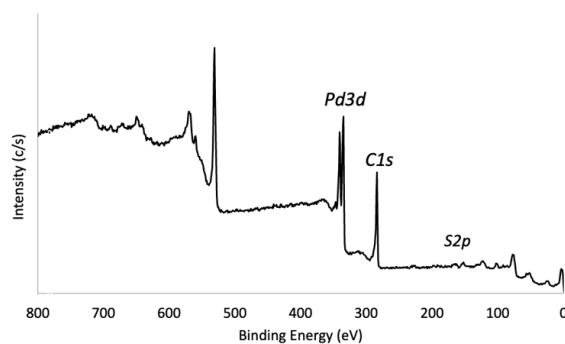


**Figure 3.** XPS survey of Pd/SO<sub>3</sub>H/CNO.

## Electrochemical behavior of the sensors

The CV voltammograms are shown in the with and without DA in 0.01 M PBS in Fig. 4a-c. While no oxidation peak was observed for the CNO and Pd/SO<sub>3</sub>H/CNO in the DA-free electrolyte, upon the introduction of 100 μM DA into the solution, redox peaks appeared at 0.3 V and -0.2V. It is because of the two-electron oxidation of DA, yielding dopamine quinone [43]. Additionally, The oxidation current of Pd/SO<sub>3</sub>H/CNO was much higher than that of CNO, indicating that Pd/SO<sub>3</sub>H/CNO sample had much higher catalytic activity against the oxidation of

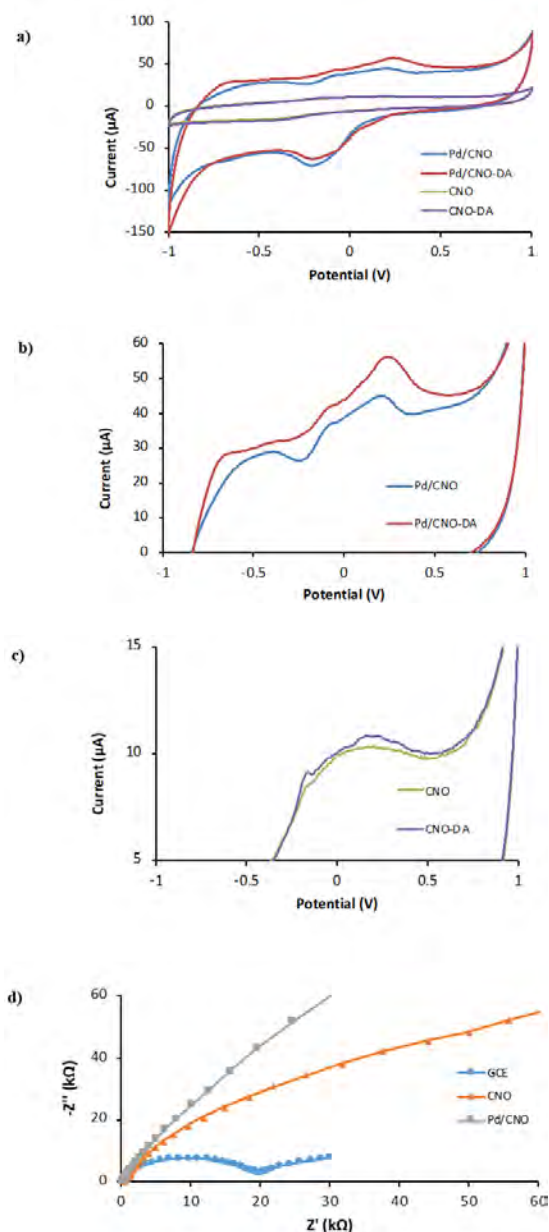


**Figure 4.** a) Electrochemical behavior of sensors in the presence of 100 μM DA, CV curves for b) Pd/CNO, c) CNO, and d) EIS diagrams.

DA. As shown in Fig. 4c, the unmodified CNO sample had a low analytical response. Note that Pd nanoparticles on the CNO surface enhances the electron mobility, improving the electrochemical activity. The EIS results of bare-GCE, GC-CNO, and Pd/SO<sub>3</sub>H-CNO-GC are given in Fig. 4d. The electron transfer resistance ( $R_{ct}$ ) of bare-GCE was found to be about 19 kΩ. The electron charge transfer resistance of the CNO and Pd/SO<sub>3</sub>H/CNO modified GCs were found to be lower than bare-GCE. However, Pd nanoparticles on the CNO surface improved the charge transfer rate, resulting in a lower semi-circle.

The oxidation behavior of DA at various pH was evaluated using CV experiments and the results indicated that the electrolyte pH impacts the electrochemical activity towards DA. With the increase in the pH (Fig. 5a-b), the measured oxidation current decreased. The oxidation current decreased with the increasing pH of the solution. With the participation of protons in the DA oxidation, the peak potentials shifted to smaller values. According to the obtained CV curve, the highest current was obtained at the pH of 3.0. Therefore, further experiments were conducted at this pH value.

Fig. 5c shows the cyclic voltammograms recorded at different scan rates (10 to 400 mV/s) in the presence of 100 μM DA. The results showed that the oxidation current increased at higher scan rates. The relationship between the peak current and the scan rate graphs is shown in Figure 5d. The results show that DA oxidation on Pd/SO<sub>3</sub>H/CNO is a surface-controlled reaction.

DPV measurement was performed between 10 μM and 400 μM of DA in 0.1 M PBS at a pH of 3.0 at a scan rate of 25 mV/s. (Fig. 6a). The oxidation peak appeared at 0.35 V for the sensor. The average linear regression plots and the concentration of DA results are shown in Fig. 6b. DA concentrations in the range of 100 μM to 400 μM ( $y=0.1355x+0.7833$  and  $y=0.0269x+10.959$ ), with a  $R^2$  value 0.9933 and 0.9993, respectively. The results suggested that the Pd modification of CNO enhances the electroactive sites and speed up the rate of electron transfer. Hence, Pd nanoparticles provide a high surface area to volume ratio and act as an effective performance to detect DA. These results showed that our sensor's upper linear range limit of 400 μM. The average sensitivity of the sensor was calculated to be  $1.93 \pm 0.14 \mu\text{A } \mu\text{M}^{-1} \text{ cm}^{-2}$  from three different experiments ( $n=3$ , RSD %: 3.6). The detection limit (LOD) of the sensor was calculated according to the  $\text{LOD}=3s/S$  equation. The LOD of the sensor was found to be  $2.44 \mu\text{M}$  ( $n=3$ ). A low RSD % of 3.06 ( $n=3$ ) was calculated from three different sensors, these results showed that this sensor has a high reproducibility of the fabrication process.

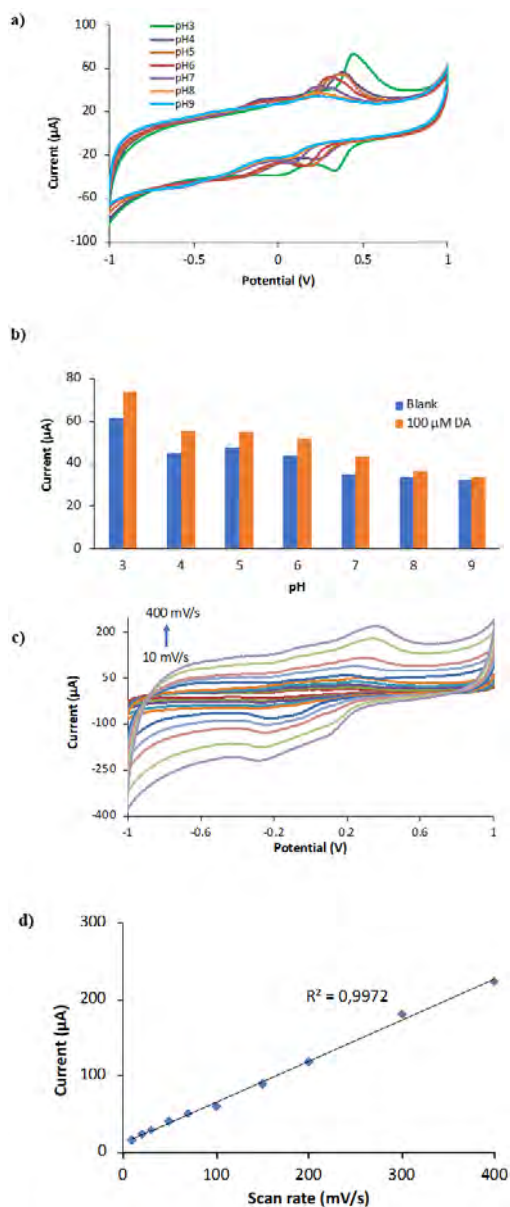


**Figure 5.** a) CV for 0.1 M PBS at different pH, b) the peak current at different pH, c) CV for different scan rates, d) Effect of scan rate on the peak current.

Note that the sensor can be used to detect DA in the linear range between 10  $\mu\text{M}$  and 400  $\mu\text{M}$ , which is wider than the previously published articles [37, 44] and even better than some of the Pd-based electrochemical sensors [45, 46]. The presence of different interferents can affect the sensor response in real samples therefore it is essential to evaluate the sensor response in terms of selectivity. Ascorbic acid (AA), uric acid (UA), glucose (GC), and hydrogen peroxide ( $\text{H}_2\text{O}_2$ ) were used as the interferents. The selectivity study was conducted using DPV to evaluate the response of our sensors against the interferents. DPV measurements were recorded in the presence of 50  $\mu\text{M}$  AA, UA, GC, and 200  $\mu\text{M}$   $\text{H}_2\text{O}_2$  different DA concentrations of 50 and 200  $\mu\text{M}$  (Fig. 7a). When the DA was added to the solution containing the

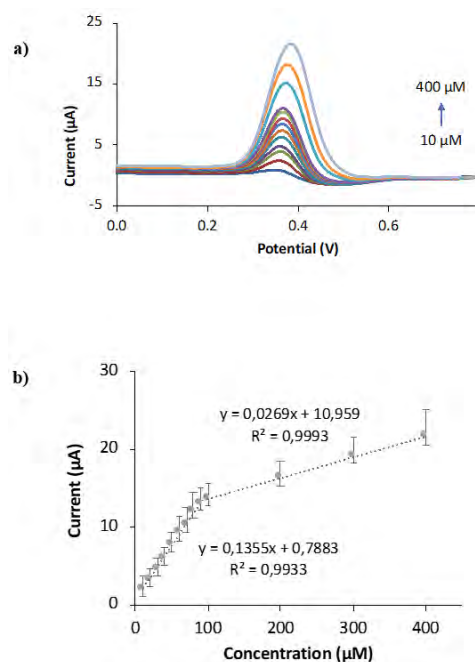


**Figure 6.** a) DPV results of the sensors at different concentrations of DA (10  $\mu\text{M}$  to 400  $\mu\text{M}$ ), b) Linear plots versus concentration of DA and linear regression equations.

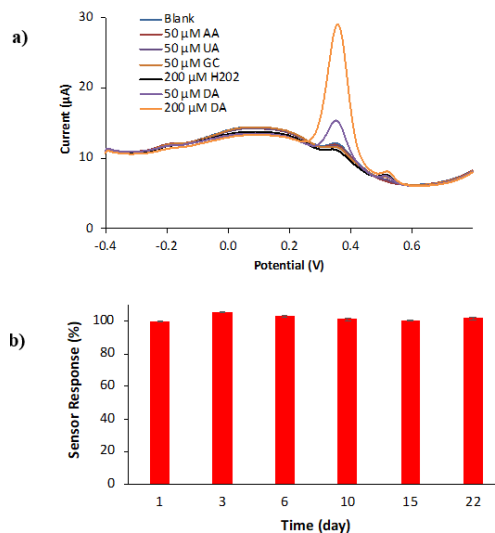


**Figure 7.** a) Interference behavior in the detection of dopamine, b) Storage stability results of the sensor.

interfering molecules, the current increased dramatically due to the detection of DA. Furthermore, no change in the peak current was obtained in the presence of interferents in the electrolyte, confirming a high selectivity. The storage stability of the sensors were studied by measuring the analytical response of the sensors against 20  $\mu\text{M}$  DA for 22 days. The sensors were stored at room temperature throughout the stability experiments. The sensors yielded the analytical responses of  $2.48 \pm 0.28$  (100 %) and  $2.52 \pm 0.57$   $\mu\text{A}$  (101.77 %) for the 1<sup>st</sup> and 22<sup>nd</sup> days, respectively. Fig. 7b shows that the sensor has a good sensor stability over time.

**Table 1.** Comparison of the performances of dopamine electrochemical sensor previously published reports.

Electrode	Linear range ( $\mu\text{M}$ )	LOD ( $\mu\text{M}$ )	Ref
CNO/GRT SPE	10–99.9	0.92	[37]
Graphene-modified GC	4–100	2.64	[44]
RGOh/Pd-NPs	1–150	0.233	[45]
Pd <sub>3</sub> Pt <sub>2</sub> /PDDA-RGO	4–200	0.04	[46]
3D SWNTs–Ppy composite	5–50	5	[47]
NiFe <sub>2</sub> O <sub>4</sub> -AC/GCE	100–700	1	[48]
Au-Cu <sub>2</sub> O/rGO	10–90	3.9	[49]
Pd/SO <sub>3</sub> H/CNO	10–400	2.44	This work

SWNTs: single-wall carbon nanotubes; Ppy: polypyrrole

GC: Glass carbon

AC: Active carbon

CNO: Carbon nano-onion; GRT: Graphite

Pd<sub>3</sub>Pt<sub>2</sub>: Bimetallic nanoparticles Palladium and platinum

PDA: Polydopamine

PDDA: poly (diallyl dimethylammonium chloride)

RGO: Reduced graphene oxide

The electroanalytical performance of the Pd/SO<sub>3</sub>H/CNO-based electrochemical sensors was compared with published other reported DA sensor, as given in Table 1. The linear range of our sensors is much wider and the LOD of the sensor is much smaller than many previously published reports (Table 1). These results can be explained by the large surface area of Pd-doped CNO.

In order to assess the practical feasibility of the sensor, a commercial DA injection solution (Dopadren 200 mg/ml) was purchased from a local pharmacy. The dopamine injection solution was spiked into the PBS solution and DPV was carried out to determine the DA oxidation current. As seen in Table 2, the calculated recovery values were in the range of 97.76 % to 111.23 %. Each measurement was carried out three times (n=3). These results showed that the sensor had acceptable repeatability for the DA in real samples.

## CONCLUSION

In this study, the surface of CNO was modified with SO<sub>3</sub>H functional groups and Pd nanoparticles to achieve high electrochemical activity against DA. The electroanalytical performance analyses were conducted using CV and DPV techniques in PBS. The sensor yielded the highest response against DA at a pH 3.0. The LOD and linear

**Table 2.** Real sample results of the sensor.

Spiked ( $\mu\text{M}$ )	Calculated ( $\mu\text{M}$ )	Recovery (%)	RSD (%)
10	10.09	100.90	10.0
20	22.24	111.23	1.0
30	29.32	97.76	5.48

range of the sensor were 2.44  $\mu\text{M}$ , and 10–400  $\mu\text{M}$ , respectively, and these data were compared with published reports. The TEM, XPS, and XRD results showed that SO<sub>3</sub>H/CNO samples were decorated with Pd nanoparticles successfully. The Pd/SO<sub>3</sub>H-CNO-modified GCs showed higher performance compared to CNO-modified GCs. The Pd/SO<sub>3</sub>H/CNO-based sensors showed high electrochemical sensitivity, selectivity, and storage stability. Additionally, real sample analysis results indicated that our sensors can be used in real samples to detect DA.

## ACKNOWLEDGEMENT

The author acknowledges no financial support.

## CONFLICT OF INTEREST

The author states no conflict of interests.

## DATA AVAILABILITY

The dataset generated and/or analyzed in the current study is available from the corresponding author upon reasonable request.

## References

- Zhao, K. and X. Quan, Carbon-Based Materials for Electrochemical Reduction of CO<sub>2</sub> to C<sub>2</sub>+ Oxygenates: Recent Progress and Remaining Challenges. *ACS Catalysis*, 2021. 11(4): p. 2076–2097.
- Karimi, A., et al., Graphene based enzymatic bioelectrodes and biofuel cells. *Nanoscale*, 2015. 7(16): p. 6909–6923.
- Najafi, A.S.G. and T. Alizadeh, One-step hydrothermal synthesis of carbon nano onions anchored on graphene sheets for potential use in electrochemical energy storage. *Journal of Materials Science: Materials in Electronics*, 2022. 33(10): p. 7444–7462.
- Pallavolu, M.R., et al., A novel hybridized needle-like Co<sub>3</sub>O<sub>4</sub>/N-CNO composite for superior energy storage asymmetric supercapacitors. *Journal of Alloys and Compounds*, 2022. 908: p. 164447.
- Dalal, C., et al., Fluorescent carbon nano-onion as bioimaging probe. *ACS Applied Bio Materials*, 2021. 4(1): p. 252–266.
- Kan, X., et al., 2008. - 112(- 13): p. - 4854.
- Yeon, J.H., et al., Generation of carbon nano-onions by laser irradiation of gaseous hydrocarbons for high durability catalyst support in proton exchange membrane fuel cells. *Journal of Industrial and Engineering Chemistry*, 2019. 80: p. 65–73.
- Camasca, A. and S. Giordani, Carbon nano-onions in biomedical applications: Promising theranostic agents. *Inorganica Chimica Acta*, 2017. 468: p. 67–76.
- Sharma, A., et al., 2022. - 7(- 42): p. - 37756.
- Tripathi, K.M., et al., From the traditional way of pyrolysis to tunable photoluminescent water soluble carbon nano-onions for cell imaging and selective sensing of glucose. *RSC advances*, 2016. 6(44): p. 37319–37329.
- Breczko, J., M.E. Plonska-Brzezinska, and L. Echehoyen, 2012. - 72: p. - 67.
- Yang, J., Y. Zhang, and D.Y. Kim, Electrochemical sensing


- performance of nanodiamond-derived carbon nano-onions: Comparison with multiwalled carbon nanotubes, graphite nanoflakes, and glassy carbon. *Carbon*, 2016. 98: p. 74-82.
13. Babar, D.G., et al., Carbon Nano Onions–Polystyrene Composite for Sensing S-Containing Amino Acids. *Journal of Composites Science*, 2020. 4(3): p. 90.
  14. Sok, V. and A. Frago, Carbon nano-onion peroxidase composite biosensor for electrochemical detection of 2, 4-D and 2, 4, 5-T. *Applied Sciences*, 2021. 11(15): p. 6889.
  15. Aparicio-Martínez, E., et al., Flexible electrochemical sensor based on laser scribed Graphene/Ag nanoparticles for non-enzymatic hydrogen peroxide detection. *Sensors and Actuators B: Chemical*, 2019. 301: p. 127101.
  16. Ipekci, H.H., et al., Ink-jet Printing of Particle-Free Silver Inks on Fabrics with a Superhydrophobic Protection Layer for Fabrication of Robust Electrochemical Sensors. *Microchemical Journal*, 2021: p. 106038.
  17. Mohapatra, J., et al., Enzymatic and non-enzymatic electrochemical glucose sensor based on carbon nano-onions. *Applied Surface Science*, 2018. 442: p. 332-341.
  18. Uzunoglu, A., A.D. Scherbarth, and L. Stanciu, Bimetallic PdCu/SPCE non-enzymatic hydrogen peroxide sensors. 2015: *Sensors and Actuators B: Chemical*. p. 968-976.
  19. Uzunoglu, A. and H.H. Ipekci, The use of CeO<sub>2</sub>-modified Pt/C catalyst inks for the construction of high-performance enzyme-free H<sub>2</sub>O<sub>2</sub> sensors. *Journal of Electroanalytical Chemistry*, 2019. 848: p. 113302.
  20. Wang, J., et al., Dopamine and uric acid electrochemical sensor based on a glassy carbon electrode modified with cubic Pd and reduced graphene oxide nanocomposite. *Journal of colloid and interface science*, 2017. 497: p. 172-180.
  21. Uzunoglu, A., et al., PdAg-decorated three-dimensional reduced graphene oxide-multi-walled carbon nanotube hierarchical nanostructures for high-performance hydrogen peroxide sensing. *Mrs Communications*, 2018. 8(3): p. 680-686.
  22. Sohoul, E., et al., Introducing a novel nanocomposite consisting of nitrogen-doped carbon nano-onions and gold nanoparticles for the electrochemical sensor to measure acetaminophen. *Journal of Electroanalytical Chemistry*, 2020. 871: p. 114309.
  23. Dar, R.A., et al., Performance of palladium nanoparticle–graphene composite as an efficient electrode material for electrochemical double layer capacitors. *Electrochimica Acta*, 2016. 196: p. 547-557.
  24. Kłębowski, B., et al., Applications of noble metal-based nanoparticles in medicine. *International journal of molecular sciences*, 2018. 19(12): p. 4031.
  25. Agostini, G., et al., Effect of pre-reduction on the properties and the catalytic activity of Pd/carbon catalysts: A comparison with Pd/Al<sub>2</sub>O<sub>3</sub>. *ACS Catalysis*, 2014. 4(1): p. 187-194.
  26. Fu, L., et al., Advanced Catalytic and Electrocatalytic Performances of Polydopamine-Functionalized Reduced Graphene Oxide-Palladium Nanocomposites. *ChemCatChem*, 2016. 8(18): p. 2975-2980.
  27. Law, C.K.Y., et al., Electrochemically assisted production of biogenic palladium nanoparticles for the catalytic removal of micropollutants in wastewater treatment plants effluent. *Journal of Environmental Sciences*, 2022.
  28. T, K., et al., - O5.1. Striatal Dopamine and Reduced Reward Prediction Error Signaling In. - *Schizophr Bull*. 2020 May;46(Suppl 1):S11. doi: 10.1093/schbul/sbaa028.024. Epub, (- 0586-7614 (Print)): p. T - ppublish.
  29. Whitton, A.E., et al., Baseline reward processing and ventrostriatal dopamine function are associated with pramipexole response in depression. *Brain*, 2020. 143(2): p. 701-710.
  30. Napier, T.C., A. Kirby, and A.L. Persons, 2020. - 102.
  31. Pan, X., et al., Dopamine and Dopamine Receptors in Alzheimer's Disease: A Systematic Review and Network Meta-Analysis. *Frontiers in Aging Neuroscience*, 2019. 11.
  32. Feng, P., et al., 2018. - 10(- 5): p. - 4368.
  33. Lin, T.-Y., et al., Diagnosis by simplicity: an aptachip for dopamine capture and accurate detection with a dual colorimetric and fluorometric system. *Journal of Materials Chemistry B*, 2018. 6(20): p. 3387-3394.
  34. Zhang, X., et al., A simple, fast and low-cost turn-on fluorescence method for dopamine detection using in situ reaction. *Analytica chimica acta*, 2016. 944: p. 51-56.
  35. Vuorenso, K., H. Sirén, and U. Karjalainen, Determination of dopamine and methoxycatecholamines in patient urine by liquid chromatography with electrochemical detection and by capillary electrophoresis coupled with spectrophotometry and mass spectrometry. *Journal of Chromatography B*, 2003. 788(2): p. 277-289.
  36. Uzunoglu, A. and L. Stanciu, Novel CeO<sub>2</sub>-CuO-decorated enzymatic lactate biosensors operating in low oxygen environments. *Analytica Chimica Acta*, 2016. 909: p. 121-128.
  37. Cumba, L.R., et al., Electrochemical properties of screen-printed carbon nano-onion electrodes. *Molecules*, 2020. 25(17): p. 3884.
  38. Ozoemena, O.C., et al., Electrochemical sensing of dopamine using onion-like carbons and their carbon nanofiber composites. *Electrocatalysis*, 2019. 10(4): p. 381-391.
  39. Han, F.-D., B. Yao, and Y.-J. Bai, Preparation of carbon nano-onions and their application as anode materials for rechargeable lithium-ion batteries. *The Journal of Physical Chemistry C*, 2011. 115(18): p. 8923-8927.
  40. Xin, L., et al., Polybenzimidazole (PBI) Functionalized Nanographene as Highly Stable Catalyst Support for Polymer Electrolyte Membrane Fuel Cells (PEMFCs). *Journal of the Electrochemical Society*, 2016. 163(10): p. F1228-F1236.
  41. Xing, L., et al., Understanding Pt Nanoparticle Anchoring on Graphene Supports through Surface Functionalization. *ACS Catalysis*, 2016. 6(4): p. 2642-2653.
  42. Bozkurt, S., et al., A hydrogen peroxide sensor based on TNM functionalized reduced graphene oxide grafted with highly monodisperse Pd nanoparticles. *Analytica Chimica Acta*, 2017. 989: p. 88-94.
  43. Wu, D., et al., 2014. - 116: p. - 249.
  44. Liu, Q., et al., Electrochemical detection of dopamine in the presence of ascorbic acid using PVP/graphene modified electrodes. *Talanta*, 2012. 97: p. 557-562.
  45. Palanisamy, S., S. Ku, and S.-M. Chen, Dopamine sensor based on a glassy carbon electrode modified with a reduced graphene oxide and palladium nanoparticles composite. *Microchimica Acta*, 2013. 180(11): p. 1037-1042.
  46. Yan, J., et al., Simultaneous electrochemical detection of ascorbic acid, dopamine and uric acid based on graphene anchored with Pd–Pt nanoparticles. *Colloids and Surfaces B: Biointerfaces*, 2013. 111: p. 392-397.
  47. Min, K. and Y.J. Yoo, Amperometric detection of dopamine based on tyrosinase–SWNTs–Ppy composite electrode. *Talanta*, 2009. 80(2): p. 1007-1011.
  48. Aparna, T. and R. Sivasubramanian, Selective electrochemical detection of dopamine in presence of ascorbic acid and uric acid using NiFe<sub>2</sub>O<sub>4</sub>-activated carbon nanocomposite modified glassy carbon electrode. *Materials Today: Proceedings*, 2018. 5(8): p. 16111-16117.

49. Aparna, T., R. Sivasubramanian, and M.A. Dar, One-pot synthesis of Au-Cu<sub>2</sub>O/rGO nanocomposite based electrochemical sensor for selective and simultaneous detection of dopamine and uric acid. *Journal of Alloys and Compounds*, 2018. 741: p. 1130-1141.



# Interaction of GHK Tripeptide with Receptors Targeted in Some Cancer Studies: A Theoretical Approach with Molecular Docking

**Bilge Bicak**  **Serda Kecel Gunduz** 

 Istanbul University, Department of Physics, Istanbul, Türkiye

## ABSTRACT

Cancer, defined as the uncontrolled growth and proliferation of cells, is a serious disease seen in many people around the world. For this reason, a lot of work has been done and continues to be done by scientists for the diagnosis and treatment of cancer. It is known that various receptors are targeted in studies on cancers. In this study, ER, PR, EGFR and HER2 receptors, which are among the most frequently used target receptors, were selected. GHK is a tripeptide that has important benefits such as increasing cancer resistance and reversing cancer cells. In this study, the complex structures formed by the most commonly used target receptors (ER, PR, EGFR and HER2) and the GHK tripeptide were examined. These complex structures were obtained by molecular docking method that is a molecular modeling method used to predict how a receptor interacts with small molecules. As a result of the study, binding affinities, close interactions, and interaction types of GHK and receptors were determined, and interaction profiles with various drugs (such as tamoxifen, erlotinib and neratinib) in the literature were examined comparatively. In the light of the findings obtained in the studies, it was determined that the GHK tripeptide gave similar interaction profiles with the drugs used in cancer treatment.

### Keywords:

Peptide, GHK, EGFR, Cancer, Docking

## INTRODUCTION

Normal cells grow and multiply for new cells needed in the body. When normal cells get old or damaged, they die and are replaced by new cells. With the disruption of this natural process, cancer cells are formed. Cancer is a disease that occurs when some cells in the body grow and multiply uncontrollably. These cells form tumors, which are lumps of tissue. These tumors may begin to spread throughout the body (1).

Breast cancer, which is one of the hormonal cancer types, is one of the most common cancer types in women. Estrogen and progesterone are hormones that are seen as potential risks in breast cancer (2, 3). Overexpression of estrogen and progesterone receptors are prominent distinguishing features in breast cancer cases. Therefore, studies have been made for breast cancer therapeutics to target these receptors (4–6). Estrogen receptor is one of the targets used not only in breast cancer, but also in treatment and prevention studies related to prostate, colon, and ovarian cancer (7, 8). Overexpression of progesterone is associated with

overexpression of estrogen. PR overexpression, observed with estrogen overexpression, plays an important role in better diagnosis of PR+ breast cancer and higher response to hormonal therapy (2). Other important receptors in breast cancer are epidermal growth factor receptor (EGFR/HER1) and epidermal growth factor receptor 2 (EGFR2/HER2) (2, 9, 10). Overexpression of EGFR is also observed in breast cancer (11) and affects cell signaling and play a role in oncogenesis (12). In ER-, PR- and HER2- breast cancer (triple negative breast cancer) studies, EGFR level was found to be increased. Since treatment is limited in triple negative breast cancer, the use of EGFR antagonists is at the forefront of treatment strategies (13, 14). Additionally, more than half of non-small cell lung carcinomas express EGFR. Therefore, EGFR has an important place in lung cancer studies (15). Signaling pathways that occur in EGFR activation in colon cancer are also important (16). Another target used in anti-cancer studies is HER2 (12, 17). Both EGFR (HER1) and HER2 are used as target inhibitors in HER2+ breast cancer. The limitations of single-targeting used in treatment studies are tried to be overcome with

### Article History:

Received: 2023/02/24

Accepted: 2023/06/30

Online: 2023/09/30

Correspondence to: Bilge Bicak,

E-mail: bbicak@istanbul.edu.tr,

Phone: +90 212 455 57 00-13763;

This article has been checked for similarity.



This is an open access article under the CC-BY-NC licence

<http://creativecommons.org/licenses/by-nc/4.0/>

### Cite as:

Bicak B and Kecel Gunduz S, "Interaction of Ghk Tripeptide with Receptors Targeted in Some Cancer Studies: A Theoretical Approach with Molecular Docking" Hittite Journal of Science and Engineering, 10(3):211–217, 2023. doi:10.17350/hjse19030000309



multi-targeted studies. These types of studies have shown that drug therapy is more effective (12, 18). Apart from breast cancer studies, HER2 is also prominent in other cancer types. In non-small cell lung cancer, HER2 is a biomarker of cancer proliferation (19). It has been reported in studies that HER2 gene mutations can be associated with the response to targeted agents in non-small cell lung cancer (20).

GHK is a tripeptide with antioxidant, anti-inflammatory, wound healing, ulcer, anticancer and bone tissue healing properties (21, 22). GHK has many studies on the preservation and repair of tissues (23). In addition to these properties of GHK, it has also proven to be effective in modulating a number of genes. A study with GHK found that it reversed the pathological expression of the gene in metastasis-prone colon cancer and was effective in directing gene expression to healthy remodeling in COPD lungs (24, 25). In a study, it was reported that GHK reduce the viability of glioblastoma cells at higher concentrations while the viability of L929 cells stay the same as the control (21). In a study with GHK-Cu complex, gene effects on MCF-7 breast and PC3 prostate cancer cell lines were investigated (26). It is also known that the GHK-Cu complex provides regeneration of the lung and liver. In addition, studies on human cancer cells (SH-SY5Y, U937 and breast cancer cells) have shown that GHK activates programmed cell death and inhibits cell growth (23, 27, 28).

Molecular docking method is a molecular modeling method frequently used in drug development studies. In this method, it is aimed to predict the complex structure of the drug candidate molecule (ligand) and the selected macromolecule (receptor), and to determine the most stable structure of this complex structure and to find the most appropriate pose of the ligand. That is, the ligand-receptor complex is studied at the atomic level and the interaction profile of the ligand in the active site of the receptor is determined (29, 30). Afterwards, a theoretical background is obtained by comparing the interaction profile of the studied disease-related drug molecules in the active site of the receptor with the interaction profile of the investigated molecule (ligand).

In this study, 4 different receptors (ER, PR, EGFR and HER2), which are known as target receptors in cancer studies, were determined and their interactions with GHK tripeptide were investigated by molecular docking method for the first time. The interaction profiles of GHK tripeptide with these receptors were compared with the interaction profiles of cancer drug molecules such as tamoxifen, erlotinib and neratinib.

## MATERIAL AND METHODS

With the molecular docking study, it was aimed to obtain an estimate of the complex structures of the GHK tripeptide with the receptors targeted in cancer studies. The binding mode of the GHK tripeptide with the binding sites of ER, PR, EGFR and HER2 were determined. Firstly, GHK and all receptors were prepared via AutoDock Tools 1.5.6. Estrogen receptor (PDB ID: 1A52) (31), Progesterone receptor (PDB ID: 2OVM) (32), epidermal growth factor receptor (PDB ID: 1M17) (33) and Receptor tyrosine-protein kinase erbB-2 (HER2) (PDB ID: 3RCD) (34) were downloaded from PDB DataBank (<https://www.rcsb.org/>). Receptors were prepared for molecular docking studies by removing water, ions, and other ligands and adding polar hydrogens. After ligand and receptors were prepared, grid boxes were adjusted as 30Åx30Åx30Å. All molecular docking studies were run using AutoDock Vina (35). After molecular docking studies were completed successfully, initial visualizations were performed with Pymol program (36), then interaction types and distances (Å) of ligand-receptor complexes were determined and visualized by Discovery Studio Visualizer 2019 (37).

## RESULTS AND DISCUSSION

### Estrogen Receptor (PDB ID: 1A52)

ER+ breast cancer constitutes the majority of breast cancers (38). ER $\alpha$ , which is abundant in cancerous tissues, is associated with cancer inhibition, but may also contribute to cancer progression. For these reasons, Estrogen receptor alpha (ER $\alpha$ ) is an important receptor frequently used in theoretical studies on breast cancer (39). In this study, estrogen receptor and GHK tripeptide was docked and determined the binding energy of best docking pose as -6.7 kcal/mol by AutoDock Vina program. GHK in the active site of ER $\alpha$ , close interactions and interaction types of GHK-ER $\alpha$  complex were shown in Figure 1. Additionally, detailed interaction types and distances between GHK-ER $\alpha$  complex were tabulated in Table 1.

Like the drugs (tamoxifen and exemestane), used to treat breast cancer, and estradiol, one of the three naturally produced estrogen hormones in the body, GHK also interacted with the ER $\alpha$ . GHK in the active site of ER $\alpha$  formed hydrogen bonds, pi-alkyl and van der Waals (vdW) interactions. GHK tripeptide formed 3 hydrogen bonds with Thr-347 residue of ER $\alpha$  (~2.71 Å, 2.71 Å and 3.03 Å). The tripeptide also formed carbon hydrogen bond with Gly-521

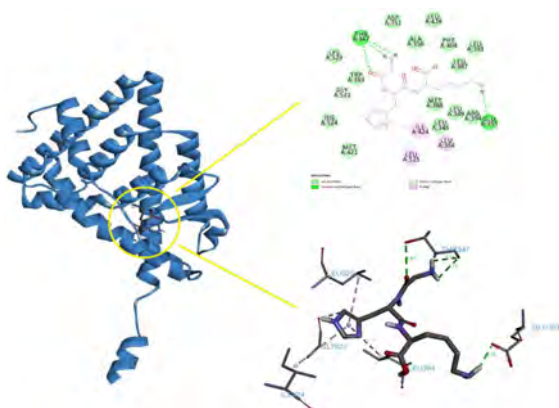


**Figure 1.** The close interactions of GHK tripeptide at ER $\alpha$  active site.

**Table 1.** The interaction types and distances (Å) of GHK- ER $\alpha$  complex.

Receptor ER $\alpha$ PDBID:1A52; with -6.7 kcal/mol Docking Score Energy		
Residue	Interaction Type	Distance (Å)
Thr-347	H-Bond	2.71
		2.71
		3.03
Glu-353	H-Bond	2.15
Gly-521	Carbon Hydrogen Bond	3.38
Leu-384	Pi-Alkyl	5.36
Ile-424	Pi-Alkyl	5.18
Leu-525	Pi-Alkyl	5.16
Leu-346, Leu-349, Ala-350, Asp-351, Trp-383, Leu-387, Met-388, Leu-391, Arg-394, Phe-404, Met-421, Leu-428, His-524, Lys-529	Van der Waals	

residue ( $\sim 3.38$  Å). Looking at other interactions, it was seen that GHK formed pi-alkyl interactions with Leu-384, Ile-424 and Leu-525 residues of ER $\alpha$  and vdW interactions with Leu-346, Leu-349, Ala-350, Asp-351, Trp-383, Leu-387, Met-388, Leu-391, Arg-394, Phe-404, Met-421, Leu-428, His-524 and Lys-529 residues of ER $\alpha$ . Mani et al. reported important residues forming the active site of ER $\alpha$  (9). According to this literature information, GHK tripeptide interacted with some important residues. These residues were Glu-353, Leu-525, Leu-384, His-524, Met-388, Leu-346, Arg-394, Ala-350, Phe-404 and Leu-387. In the study of Mani et al., the close interactions of two important molecules, estradiol and tamoxifen, with ER $\alpha$  residues were presented (9). When the interactions of GHK and these molecules (estradiol and tamoxifen) with the ER $\alpha$  were compared, it was determined that the close interaction residues between the molecules (estradiol and tamoxifen) and the ER $\alpha$  completely interacted with GHK tripeptide. In another docking study mentioned in the literature, exemestane, which is used in the treatment of breast cancer, was docked with the ER $\alpha$

and it was reported that the exemestane made hydrogen bonds with Glu-353, Arg-394 and His-524 residues of ER (40). In this study, GHK tripeptide interacted with these three residues via hydrogen bonding with Glu-353, vdW interactions with Arg-394 and His-524. As a result, when compared with the literature, it was determined that the GHK tripeptide interacts in the active region of the ER and even interacts with the same residues with the molecules used in breast cancer.

### Progesterone receptor (PDB ID: 2OVM)

Progesterone receptors as well as ER are prognostic biomarkers in hormone-dependent breast cancers. Most breast cancers are ER+, PR+ or both positive (9, 41). In this study, progesterone receptor (PR) and GHK tripeptide was docked and determined the binding energy of best docking pose as -6.1 kcal/mol by AutoDock Vina program. GHK in the active site of PR, close interactions and interaction types of GHK-PR complex were shown in Figure 2. Additionally, detailed interaction types and distances between GHK-PR complex were tabulated in Table 2.

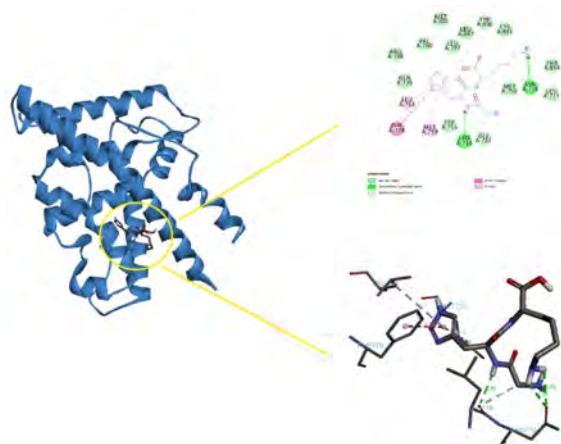


**Figure 2.** The close interactions of GHK tripeptide at PR active site.

As a result of docking of GHK with the progesterone receptor, it was determined that the GHK tripeptide formed hydrogen bonds, pi-alkyl, pi-pi t-shaped and vdW interactions at the determined active site of progesterone. Asoprisnil, a progesterone receptor modulator, (42) and tamoxifen, a drug used in the treatment of breast cancer, (9) interacted with the residues such as Leu-718, Asn-719, Gly-722, Gln-725, Met-756, Met-759, Val-760, Phe-778, Leu-887, Leu-797, Met-801, Tyr-890, Cys-891, Thr-894 in the progesterone active site, commonly. Hydrogen bonds with common residues Leu-718 (2.43 Å and 3.68 Å (carbon hydrogen bond)) and Asn-719 (2.59 Å and 2.69 Å), pi-alkyl interactions with Met-759 (5.15 Å), pi-pi T-shaped interactions with Phe-778 (5.22 Å), and vdW interactions with Gly-722, Gln-725, Met-756, Val-760, Leu-797, Met-801, Leu-887, Tyr-890, Cys-891,

Thr-894 were found in GHK tripeptide. Additionally, GHK interacted with Leu-763 residue of PR via pi-alkyl interaction (4.71 Å) and Trp-755, Arg-766 residues of PR via vdW interaction. In the literature, it was reported that tamoxifen and asoprisnil formed close interaction with Leu-763 (9) and Trp-755;Arg-766 (42), respectively. When the binding energies were compared, it was determined that the tripeptide had a strong binding energy as tamoxifen (-6.1 kcal/mol (9)), although not as strong as asoprisnil (-12.99 kcal/mol (42)).

**Table 2.** The interaction types and distances (Å) of GHK-PR complex.

Receptor PR PDBID: 2OVM ; with -6.1 kcal/mol Docking Score Energy		
Residue	Interaction Type	Distance (Å)
	H-Bond	2.43
Leu-718	Carbon Hydrogen Bond	3.68
Asn-719	H-Bond	2.59 2.69
Met-759	Pi-Alkyl	5.15
Leu-763	Pi-Alkyl	4.71
Phe-778	Pi-Pi T-Shaped	5.22
Leu-715, Gly-722, Gln-725, Trp-755, Met-756, Val-760, Arg-766, Leu-797, Met-801, Leu-887, Tyr-890, Cys-891, Thr-894	Van der Waals	

### Epidermal Growth Factor Receptor ( PDB ID: 1M17)

With the emergence of resistance cases in the treatment of breast cancer, the search for new drugs has become a necessity. Since new drugs are expected to have high anticancer activity and minimal side effects, studies focused on growth factor receptor (GFR) targeting. In studies, it was aimed to develop new drug types with the prediction of epidermal growth factor receptor (EGFR/HER1) signal pathway inhibition. Because overexpression of EGFR can cause uncontrolled cell growth (12, 43). In this study, EGFR and GHK tripeptide was docked and determined the binding energy of best docking pose as -6.2 kcal/mol by AutoDock Vina program. GHK in the active site of EGFR, close interactions and interaction types of GHK-EGFR complex were shown in Figure 3. Additionally, detailed interaction types and distances between GHK-EGFR complex were tabulated in Table 3.

It was determined that the interactions between GHK tripeptide and EGFR consisted of hydrogen bonding, pi interactions and van der Waals interactions. A closer look at the close interactions revealed that GHK forms 3 hydrogen bonds with EGFR through Asp-831. In a docking study of Erlotinib, a drug used in the treatment of lung and pan-

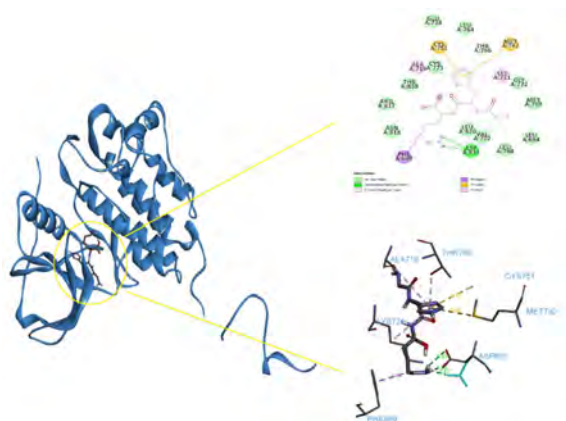


**Figure 3.** The close interactions of GHK tripeptide at EGFR active site.

creatic cancer, and EGFR in the literature, close interactions with Asp-831 were observed (43). The GHK tripeptide made pi-alkyl interactions with Ala-719 and Lys-721 residues of EGFR. Erlotinib drug also made hydrophobic interactions (alkyl/pi-alkyl) interactions with these two residues (12). In other words, it was observed that GHK and Erlotinib have the same interaction types with the residues interacted with. GHK made pi-sigma interaction with Phe-699 and pi-donor hydrogen bond with Thr-766. Erlotinib had van der Waals interactions with these two residues (12). GHK also made pi-sulfur interactions with Cys-751 and Met-742. According to this study, Erlotinib's Val-702 with pi-sigma interaction, Leu-764 with alkyl interaction and Met-769 with hydrogen bonds were determined to have vdW interactions with GHK. GHK had similar vdW interactions with erlotinib and it was determined that the common residues that erlotinib and GHK interacted were Glu-738, Thr-830, Leu-820, Leu-768 and Gly-772. GHK also had vdW interactions with Cys-773, Arg-817, Asn-818 and Leu-694 residues.

**Table 3.** The interaction types and distances (Å) of GHK-EGFR complex.

Receptor EGFR PDBID: 1M17; with -6.2 kcal/mol Docking Score Energy		
Residue	Interaction Type	Distance (Å)
	H-Bond	1.90 2.31 3.01
Phe-699	Pi-Sigma	3.53
Ala-719	Pi-Alkyl	5.24
Lys-721	Pi-Alkyl	4.73
Met-742	Pi-Sulfur	5.04
Cys-751	Pi-Sulfur	4.67
Thr-766	Pi-Donor Hydrogen Bond	3.33
Leu-694, Val-702, Glu-738, Leu-764, Leu-768, Met-769, Gly-772, Cys-773, Arg-817, Asn-818, Leu-820, Thr-830	Van der Waals	

## Receptor tyrosine-protein kinase erbB-2 (PDB ID: 3RCD)

Another important receptor that stands out in studies on breast cancer is HER-2. About 15-20% of breast cancer types are HER-2 positive (18). HER protein family is involved in cell proliferation, differentiation, and migration (12). Overexpression of the HER protein is associated with breast cancer. A linear relationship between the growth of pathological tumor diameter and HER- expression has also been reported in literature studies (44-46). In this study, HER-2 and GHK tripeptide was docked and determined the binding energy of best docking pose as -7.1 kcal/mol by AutoDock Vina program. GHK in the active site of HER-2, close interactions and interaction types of GHK-HER-2 complex were shown in Figure 4. Additionally, detailed interaction types and distances between GHK-HER-2 complex were tabulated in Table 4.

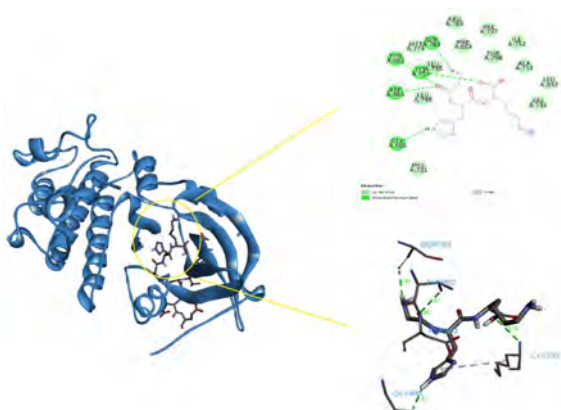


**Figure 4.** The close interactions of GHK tripeptide at HER2 active site.

GHK made hydrogen bond, pi-alkyl and vdW interactions with HER-2. GHK made a hydrogen bond with Gly-865 (2.41 Å). There was a vdW interaction between the reference drug Neratinib and Gly-865 (12). While the reference drugs Neratinib and TAK-285 made Carbon H-bond and vdW interactions with Asp-863, respectively, GHK made a hydrogen bond with this residue (2.99 Å). GHK, which has hydrogen bonding and pi-alkyl interactions with Lys-753, had similar interactions with drugs in the literature (neratinib (alkyl/pi-alkyl), TAK-285 (H-bond)). While GHK made a hydrogen bond with Thr-862 (3.07 Å), reference drugs made vdW interactions with this residue. With Ser-783, with which neratinib interacts with vdW, the GHK tripeptide formed a hydrogen bond (2.62 Å). When looking at the residues that GHK interacts with vdW, it was determined with the help of literature studies that all of them, except Arg-784, have various interactions with Neratinib and/or TAK-285 (12).

**Table 4.** The interaction types and distances (Å) of GHK-HER2 complex.

Residue	Interaction Type	Distance (Å)
Lys-753	H-Bond	3.20
	Pi-Alkyl	5.08
Ser-783	H-Bond	2.62
Thr-862	H-Bond	3.07
Asp-863	H-Bond	2.99
Gly-865	H-Bond	2.41
Phe-731, Val-734, Ala-751, Ile-752, Met-774, Arg-784, Leu-785, Leu-796, Val-797, Thr-798, Leu-852, Phe-864	Van der Waals	

## CONCLUSION

In this study, the interactions of GHK tripeptide with 4 different receptors (ER, PR, EGFR, HER2) selected as targets in cancer studies were theoretically investigated for the first time. The interaction profile of GHK tripeptide with these four receptors is presented in comparison with the interaction profiles of various anticancer drugs. As a result of the investigations, it was determined that the GHK tripeptide has similar interaction profiles with tamoxifen, exemestane and neratinib used in the treatment of breast cancer. GHK had similar interactions with erlotinib, which is used in the treatment of lung and pancreatic cancer. GHK also had similar interaction profiles with asoprisnil, a progesterone receptor modulator, and TAK-285, a novel dual erbB protein kinase inhibitor that specifically targets the human epidermal growth factor receptor (EGFR) and HER2. The result of these theoretical studies has been a pioneering study as a glimmer of hope for investigating the anticancer activity of GHK with experimental methods and examining it in more detail in peptide studies.

## CONFLICT OF INTEREST

The authors stated that did not have conflict of interests.

## AUTHOR CONTRIBUTION

B. Bicak and S. Kecel Gunduz carried out the analyses and analyzed the data. The authors co-wrote the manuscript. All authors contributed to the finalization of the manuscript.

## REFERENCES

1. D'arcy MS. Cell death: a review of the major forms of apoptosis, necrosis and autophagy. *Cell biology international*. 2019;43(6):582-92.
2. Acharya R, Chacko S, Bose P, Lapenna A, Pattanayak SP. Structure based multitargeted molecular docking analysis of selected furanocoumarins against breast cancer. *Scientific reports*. 2019;9(1):1-13.
3. Holst F, Stahl PR, Ruiz C, Hellwinkel O, Jehan Z, Wendland M, et al. Estrogen receptor alpha (ESR1) gene amplification is frequent in breast cancer. *Nature genetics*. 2007;39(5):655-60.
4. Fowler AM, Alarid ET. Amping up estrogen receptors in breast cancer. *Breast Cancer Research*. 2007;9:1-3.
5. Lange CA, Yee D. Progesterone and breast cancer. *Women's Health*. 2008;4(2):151-62.
6. Swargiary G, Mani S. ER and PGR targeting ability of phytocompounds derived from *Centella asiatica* and *Andrographis paniculata*: an in-silico approach. *Journal of Herbal Medicine*. 2022;32:100541.
7. Dhiani BA, Nurulita NA, Fitriyani F. Protein-protein Docking Studies of Estrogen Receptor Alpha and TRIM56 Interaction for Breast Cancer Drug Screening. *Indonesian Journal of Cancer Chemoprevention*. 2022;13(1):46-54.
8. Nilsson S, Gustafsson JÅ. Estrogen receptors: therapies targeted to receptor subtypes. *Clinical Pharmacology & Therapeutics*. 2011;89(1):44-55.
9. Mani S, Swargiary G, Gulati S, Gupta S, Jindal D. Molecular docking and ADMET studies to predict the anti-breast cancer effect of aloin by targeting estrogen and progesterone receptors. *Materials Today: Proceedings*. 2021.
10. Saghiri K, Daoud I, Melkemi N, Mesli F. QSAR study, molecular docking/dynamics simulations and ADME prediction of 2-phenyl-1H-indole derivatives as potential breast cancer inhibitors. *Biointerface Res Appl Chem*. 2022;13(2):154.
11. Sing LC, Roy A, Hui LY, Mun CS, Rajak H, Karunakaran R, et al. Multi-targeted molecular docking, drug-likeness and ADMET studies of derivatives of few quinoline-and acridine-based FDA-approved drugs for anti-breast cancer activity. *Structural Chemistry*. 2022;33(3):649-69.
12. Prabhavathi H, Dasegowda K, Renukananda K, Karunakar P, Lingaraju K, Raja Naika H. Molecular docking and dynamic simulation to identify potential phytocompound inhibitors for EGFR and HER2 as anti-breast cancer agents. *Journal of Biomolecular Structure and Dynamics*. 2022;40(10):4713-24.
13. Costa R, Shah AN, Santa-Maria CA, Cruz MR, Mahalingam D, Carneiro BA, et al. Targeting Epidermal Growth Factor Receptor in triple negative breast cancer: New discoveries and practical insights for drug development. *Cancer treatment reviews*. 2017;53:111-9.
14. Mueller KL, Yang Z-Q, Haddad R, Ethier SP, Boerner JL. EGFR/Met association regulates EGFR TKI resistance in breast cancer. *Journal of molecular signaling*. 2010;5(1):1-8.
15. da Cunha Santos G, Shepherd FA, Tsao MS. EGFR mutations and lung cancer. *Annual Review of Pathology: Mechanisms of Disease*. 2011;6:49-69.
16. de Castro-Carpeño J, Belda-Iniesta C, Sáenz EC, Agudo EH, Batlle JF, Barón MG. EGFR and colon cancer: a clinical view. *Clinical and Translational Oncology*. 2008;10:6-13.
17. Iqbal N, Iqbal N. Human epidermal growth factor receptor 2 (HER2) in cancers: overexpression and therapeutic implications. *Molecular biology international*. 2014;2014.
18. Tripathi S, Srivastava G, Sharma A. Computational Design of Multi-Target Drugs Against Breast Cancer. *Multi-Target Drug Design Using Chem-Bioinformatic Approaches*. 2019:443-58.
19. Landi L, Cappuzzo F. HER2 and lung cancer. *Expert review of anticancer therapy*. 2013;13(10):1219-28.
20. Mar N, Vredenburg JJ, Wasser JS. Targeting HER2 in the treatment of non-small cell lung cancer. *Lung Cancer*. 2015;87(3):220-5.
21. Budama-Kilinc Y, Kecel-Gunduz S, Cakir-Koc R, Aslan B, Bicak B, Kokcu Y, et al. Structural characterization and drug delivery system of natural growth-modulating peptide against glioblastoma cancer. *International Journal of Peptide Research and Therapeutics*. 2021;27(3):2015-28.
22. Kokcu Y, Kecel-Gunduz S, Budama-Kilinc Y, Cakir-Koc R, Bicak B, Zorlu T, et al. Structural analysis, molecular dynamics and docking calculations of skin protective tripeptide and design, characterization, cytotoxicity studies of its PLGA nanoparticles. *Journal of Molecular Structure*. 2020;1200:127046.
23. Pickart L, Vasquez-Soltero JM, Pickart FD, Majnarich J. GHK, the human skin remodeling peptide, induces anti-cancer expression of numerous caspase, growth regulatory, and DNA repair genes. *Journal of Analytical Oncology*. 2014;3(2):79-87.
24. Hong Y, Downey T, Eu KW, Koh PK, Cheah PY. A 'metastasis-prone' signature for early-stage mismatch-repair proficient sporadic colorectal cancer patients and its implications for possible therapeutics. *Clinical & experimental metastasis*. 2010;27:83-90.
25. Lamb J, Crawford ED, Peck D, Modell JW, Blat IC, Wrobel MJ, et al. The Connectivity Map: using gene-expression signatures to connect small molecules, genes, and disease. *science*. 2006;313(5795):1929-35.
26. Pickart L, Margolina A. Modulation of Gene Expression in Human Breast Cancer MCF7 and Prostate Cancer PC3 Cells by the Human Copper-Binding Peptide GHK-Cu. *OBM Genetics*. 2021;5(2):1-18.
27. Matalka L, Ford A, Unlap M. The tripeptide, GHK, induces programmed cell death in SH-SY5Y neuroblastoma cells. *Journal of Biotechnology & Biomaterials*. 2012;2:1-4.
28. Pickart L, Vasquez-Soltero JM, Margolina A. GHK and DNA: resetting the human genome to health. *BioMed research international*. 2014;2014.
29. Bicak B, Gunduz SK. Computer-Aided Drug Design of Plant-Based Compounds. *Isolation, Characterization, and Therapeutic Applications of Natural Bioactive Compounds: IGI Global*; 2022. p. 320-45.
30. Gunduz SK, Bicak B, Ozel AE. Advancements in cancer therapeutics: Computational drug design methods used in cancer studies. *Handbook of research on advancements in cancer therapeutics: IGI Global*; 2021. p. 89-115.
31. Tanenbaum DM, Wang Y, Williams SP, Sigler PB. Crystallographic comparison of the estrogen and progesterone receptor's ligand binding domains. *Proceedings of the National Academy of Sciences*. 1998;95(11):5998-6003.
32. Madauss KP, Grygielko ET, Deng S-J, Sulpizio AC, Stanley TB, Wu C, et al. A structural and in vitro characterization of asoprisnil: a selective progesterone receptor modulator. *Molecular endocrinology*. 2007;21(5):1066-81.
33. Stamos J, Sliwkowski MX, Eigenbrot C. Structure of the epidermal growth factor receptor kinase domain alone and in complex with a 4-anilinoquinazoline inhibitor. *Journal of biological chemistry*. 2002;277(48):46265-72.
34. Ishikawa T, Seto M, Banno H, Kawakita Y, Oorui M, Taniguchi T, et al. Design and synthesis of novel human epidermal growth factor receptor 2 (HER2)/epidermal growth factor receptor (EGFR) dual inhibitors bearing a pyrrolo [3, 2-d] pyrimidine scaffold. *Journal of medicinal chemistry*. 2011;54(23):8030-50.

35. Trott O, Olson AJ. AutoDock Vina: improving the speed and accuracy of docking with a new scoring function, efficient optimization, and multithreading. *Journal of computational chemistry*. 2010;31(2):455-61.
36. DeLano WL. Pymol: An open-source molecular graphics tool. *CCP4 Newsl Protein Crystallogr*. 2002;40(1):82-92.
37. Biovia DS. Discovery studio modeling environment. Release; 2017.
38. Mustarichiei R, Levitas J, Arpina J. In silico study of curcumol, curcumenol, isocurcumenol, and  $\beta$ -sitosterol as potential inhibitors of estrogen receptor alpha of breast cancer. *Medical Journal of Indonesia*. 2014;23(1):15-24.
39. Liu Y, Ma H, Yao J. ER $\alpha$ , a key target for cancer therapy: A review. *OncoTargets and therapy*. 2020;13:2183.
40. Ariazi EA, Leitao A, Oprea TI, Chen B, Louis T, Bertucci AM, et al. Exemestane's 17-hydroxylated metabolite exerts biological effects as an androgen. *Molecular cancer therapeutics*. 2007;6(11):2817-27.
41. Li Z, Wei H, Li S, Wu P, Mao X. The role of progesterone receptors in breast cancer. *Drug Design, Development and Therapy*. 2022:305-14.
42. Pratama MRF, Poerwono H, Siswandono S. Design and molecular docking of novel 5-O-Benzoylpinostrubin derivatives as anti-breast cancer. *Thai Journal of Pharmaceutical Sciences (TJPS)*. 2020;43(4).
43. Kesuma D, Siswandono S, Kirtishanti A. Molecular Docking And Biological Activity Of N-(4-Methoxy)-Benzoyl-N'-Phenylthiourea And N-(4-Trifluoro)-Benzoyl-N'-Phenylthiourea As Antibreast Cancer Candidates. *Rasayan Journal of Chemistry*. 2022;15(2):1503-8.
44. Garcia-Closas M, Brinton L, Lissowska J, Chatterjee N, Peplonska B, Anderson W, et al. Established breast cancer risk factors by clinically important tumour characteristics. *British journal of cancer*. 2006;95(1):123-9.
45. Miše I, Vučić M, Maričević I, Šokčević M, Čurić-Jurić S. Histologic subtypes of invasive lobular carcinoma in correlation with tumor status and hormone receptors. *Acta Clinica Croatica*. 2010;49(3):275-81.
46. Özmen V. Türkiye'de Meme Kanseri: Klinik ve Histopatolojik Özellikler (13.240 Olgunun Analizi). *Meme Sağlığı Dergisi/Journal of Breast Health*. 2014;10(2).



## Use of heat-killed *Aspergillus ochraceus* NRRL 3174 discs as biosorbent for petroleum removal

Nermin Hande Avcioglu  Sezen Bilen Ozyurek  Isil Seyis Bilkay 

Hacettepe University, Department of Biology, Ankara, Türkiye

### ABSTRACT

The purpose of this work was to evaluate the petroleum sorption capacity of heat-killed fungal discs obtained from *Aspergillus ochraceus* strain. Effect of various parameters such as biosorbent dose (0.5g-2.5g/100mL), petroleum concentration (0.5-5%), pH (4.0-8.0), contact time (1-12h) and re-usability of biosorbent (1-6) were investigated. Accordingly, the highest biosorption capacity was obtained with 1% petroleum concentration, 1.5 g/100mL heat-killed fungal discs, 10h contact time at pH: 5.0 and at room temperature. Additionally, each disc was able to actively use for at least 6 more cycles in biosorption experiments. The specific removal rate was calculated as 0.114 day<sup>-1</sup>, the rate constant and half-life period were also 1.609 day<sup>-1</sup>,  $t_{1/2} = 0.431$ , respectively. The kinetic study was described by the pseudo-second order model and the equilibrium modeling was found to be well fitted with Langmuir isotherm. The biosorbent(s) were characterized by Focused Ion Beam Scanning Electron Microscopy (FIB-SEM). Over 80% removal of long-chain *n*-alkanes by the heat-killed fungal discs was confirmed by GC-MS analysis. Since there has been no similar study investigating the sorption of petroleum with heat-killed *Aspergillus ochraceus* discs, this novel bio-based sorbent with its low cost, environmentally friendly and easy-to-apply properties can be used in advanced biosorption studies.

### Keywords:

Petroleum; Biosorption; Heat-killed *Aspergillus ochraceus*; Biosorption Isotherm and Kinetics

### INTRODUCTION

In recent years, vast amounts of petroleum pollutants have been released into the environment due to petrochemical activities. Physical, chemical, physicochemical, and biological methods are used in the treatment of polluted water (1-5). Although, these conventional methods are efficient, most of them are not cost-effective and have limitations (6). The biosorption and bioaccumulation processes which completely remove pollutants, have become remarkable with their low-cost, efficiency potential, high selectivity and easy designed (7, 8). Biosorption is known as physicochemical adsorption and ion exchange that occurs on the surfaces of organisms or biomaterials. Recent studies show that low-cost adsorbents are effective in the removal of organic pollutants and heavy metals from the aquatic ecosystem (9-15). Low-cost adsorbents are also used in the removal of petroleum and polycyclic aromatic hydrocarbons (PAHs) from contaminated areas (16, 17). Adsorbents like corn stack (18), orange peel (19) and pomegranate peel (20) have been used in the biosorption of petroleum hydrocarbons.

The biomass of bacteria, fungi and algae can be used as biosorbent in removing of pesticides, dyes, heavy metals, and organic pollutants from the environment (21, 22). Among them, indigenous microorganisms due to prolonged exposure to these pollutants have higher tolerance with increased adaptive capacity. Fungi, which constitute a large part of biodiversity, play an important role in ecological cycle. Therefore, it is crucial to determine the fungal tolerance and diversity in heavily polluted environments (23). Several filamentous fungi such as *Penicillium* sp., *Aspergillus* sp., *Trichoderma* sp., *Fusarium* sp., *Alternaria* sp., *Geotrichum* sp., *Rhizopus* sp., and *Monilia* sp. have high remediation potential (24). Filamentous fungi, which are ubiquitous in the environment, are among the most economical and bio-friendly biosorbents due to their vegetative properties. They also have advantages such as large-scale biomass production, low cost, and high production capacity when compared to other microorganisms (25, 26). Previous studies have been reported that different *Aspergillus* species as *A. niger*, *A. flavus*, *A. versicolor*, and *A. tamarii* NRC3 were potentially used in biosorption processes (25, 27). Among

### Article History:

Received: 2023/03/13

Accepted: 2023/07/11

Online: 2023/09/30

Correspondence to: Nermin Hande Avcioglu,

E-mail: hurkmez@hacettepe.edu.tr, Phone:

+90 312 297 8024;

Fax: +90 312 299 2028

This article has been checked for similarity.



This is an open access article under the CC-BY-NC licence

<http://creativecommons.org/licenses/by-nc/4.0/>

### Cite as:

B. BİCAK and S. KECEL GUNDUZ, "Interaction of Ghk Tripeptide with Receptors Targeted in Some Cancer Studies: A Theoretical Approach with Molecular Docking" Hittite Journal of Science and Engineering, vol. 10, no. 3, pp. x–x, 2023. doi:10.17350/hjse19030000xxx



them, *Aspergillus ochraceus* is a fungus that can be frequently encountered in decaying vegetation, soils, various agricultural products, and grains. In addition to mycotoxin, antimicrobial agent, and enzyme production that can be used in industrial processes, it has a great capacity to biosynthesize various metabolites (28, 29).

Fungi are also frequently used in the fermentation industry as they can adapt to changes in pH, oxygen levels and temperature, as well as nutrient concentration. So, they are particularly abundant in industrial waste products after fermentation processes (25). The use of high amount of fungal biomass as a biosorbent in the removal of organic pollutants from an aquatic environment is an effective, reliable, and economical method. Since the biosorption process does not involve metabolic activity, it can occur in any living or dead cell. Dead cell is more advantageous to be used as a biosorbent in biosorption processes when compared to living cell as it does not need any other nutrients and can be used in many cycles (30). Similar studies reported that dead fungal biomass has higher sorption efficiency in the removal of toxic organic pollutants (31-33). Raghukumar et al. (34) also reported that a dead fungal biomass of marine fungi NIOCC#312 could rapidly absorb phenanthrene from contaminated aquatic environment. So, organic pollutants can be adsorbed by dead cells by surface absorption, carbon sequestration and chemical reactions (30). Accordingly, the fungal biosorption is based on three basic mechanisms as (1) Extracellular accumulation (2) Intracellular accumulation and (3) Cell surface sorption/precipitation (25). Adsorption capacity of biosorbent vary depending on their porosity, specific surface area and functional groups. An ideal biosorbent should be non-toxic, easily available, reusable, has high affinity, and be used in large scale areas (30).

This study aims to investigate the biosorption capacity of heat-killed *Aspergillus ochraceus* disc with its intriguing structural features. In this context, heat-killed *Aspergillus ochraceus* discs were used as a novel and eco-friendly biosorbent for petroleum biosorption. Although a few studies have been reported on biosorption of organic pollutants using low-cost sorbents, it has not been reported a similar study that investigates the sorption of petroleum with heat-killed *Aspergillus ochraceus* discs. Accordingly, the main objectives of this study are (i) to investigate the efficiency of a new biosorbent in terms of petroleum biosorption; (ii) to optimize the biosorption parameters such as biosorbent dose, petroleum concentration, pH, contact time, and re-usability; (iii) to clarify the biosorption process by studying its kinetic and equilibrium modeling (iv) to characterize the surface morphology of biosorbent, and (v) to approve the biosorption of short-, medium- and long-chain *n*-alkanes in the petroleum with using heat-killed fungal discs.

## MATERIALS AND METHODS

### Fungal strain and cultivation conditions

*Aspergillus ochraceus* NRRL 3174 strain was obtained from Hacettepe University Culture Collection Laboratory, Beytepe, Ankara, Turkey. To enhance fungal spores, *A. ochraceus* was inoculated into Potato Dextrose Broth (PDB, Merck, Millipore, Germany) and incubation was carried out at 30 °C and 150 rpm for 7 days (Miprolab, Turkey). The fungal cultures were stored at 4 °C in the refrigerator for further use.

### Biosorbent preparation

To prepare fungal discs, *A. ochraceus* strain was inoculated on Potato Dextrose Agar (PDA, Merck, Millipore, Germany) and incubation was carried out at 30 °C for 7 days in a static incubator (Miprolab, Turkey). Following this, the fungal culture was cut with a perforator (a diameter of 7 mm) and discs were autoclaved three times to obtain heat-killed fungal discs to be used as biosorbent for further experiments (35).

### Optimization of biosorption capacity

Distilled water (pH=7.0) containing 1% (v/v) Triton X: 100 was sterilized at 121 °C for 15 min (Prior Clave, UK) for petroleum biosorption. Following the cooling, 1% (v/v) of petroleum sterilized with 0.22µm pore size cellulose acetate syringe filter (Millipore, Sartorius, Germany) was added. To determine the optimal parameters for petroleum biosorption, biosorbent dose (0.5g-2.5g/100mL), petroleum concentration (0.5-5%), pH (4.0-8.0), contact time (1-12h) and re-usability of heat-killed discs (1-6) were investigated. The biosorption capacity of heat-killed *A. ochraceus* discs were determined as follows:

$$Q_e = \frac{C_i - C_f}{m} \times V \quad (1)$$

( $Q_e$ : adsorption capacity (g/g),  $C_i$ : initial concentration of petroleum (g/L),  $C_f$ : concentration of petroleum in equilibrium (g/L),  $m$ : mass of biosorbent (g),  $V$ : volume (L)) (36). Experiments were carried out in 3 parallels with abiotic control group.

### Petroleum extraction and gravimetric analysis

Following the sorption of petroleum by heat-killed fungal discs under optimized conditions, the remaining petroleum was extracted with dichloromethane (DCM) ( $\text{CH}_2\text{Cl}_2$ ) (1:2) (Sigma- Aldrich, USA). The flasks were left

at 90 °C for 1 hour to evaporate the solvent (Memmert, Schwabach, Germany). The biosorption of petroleum was also calculated using the following equation:

$$\text{Removal}(\%) = \frac{(p_0 - p_1 - p_2)}{p_0} \times 100 \quad (2)$$

$p_0$  and  $p_1$  indicate the initial and remaining concentrations of petroleum at different incubation periods,  $p_2$  is the abiotic loss of petroleum (35, 37).

### The kinetics of petroleum removal

The specific removal rate was calculated as described before Bilen Ozyurek and Seyis Bilkay (38). The specific rate was expressed by the following formula:

$$d_x / x_0 \times dt \quad (3)$$

$d_x$  shows the change in petroleum concentration (mg/L),  $x_0$  indicates the initial concentration of petroleum (mg/L), and  $dt$  is the time interval (hour<sup>-1</sup>).

The rate constant and half-life period of petroleum was calculated using the following equations:

$$\ln c_t = \ln c_0 - Kt \quad (4)$$

$$t_{1/2} = \ln 2 / k \quad (5)$$

$c_0$  and  $c_t$  denote the initial and remaining concentrations of petroleum (mg/L),  $K$  is rate constant of the change in the petroleum content (hour<sup>-1</sup>), and  $t$  is contact time (hour) (24, 39).

### Re-usability of heat-killed fungal discs

Following the petroleum adsorption, fungal discs were removed from the biosorption medium and dried at 30 °C for 24h. Dried fungal discs were autoclaved three times to be used as biosorbent for re-usability experiments. Biosorption was carried out with re-used fungal discs under optimized conditions (1-6 times).

### Characterization of heat-killed *A. ochraceus* discs with FIB-SEM (Focused Ion Beam Scanning Electron Microscopy)

*A. ochraceus* discs were coated with gold (Leica ACE 600) and FIB-SEM (FIB-SEM GAIA3, Tescan, Czech Republic) was used to observe petroleum biosorption by heat-

killed *A. ochraceus* discs operating at 2 kV and 4 kV with magnifications of 150x, 100x and 1kx.

### GC-MS (Gas Chromatography-Mass Spectrometry)

The GC-MS analysis was carried out to determine the change in the petroleum content according to Bilen Ozyurek et al. (2021) by using TRB-1 GCMS-QP-2020 (Shimadzu, Tokyo, Japan), fitted with a capillary column, 100% Dimethyl polysiloxane, (TRB-1 Teknokroma, Spain) (TR-110132) (30m × 0.25mm × 0.1mm) (length: column ID: film thickness) by the Petroleum Research Center at Middle East Technical University (METU) in Ankara, Turkey. The extraction of residual petroleum was carried out with DCM (1:2). The carrier gas was helium at 1.5 mL/min and the injection temperature was set to 250 °C; the temperature program was adjusted to 40 °C (5 min) to 180 °C at 8 °C/min and then to 320 °C (16 min) at 10 °C/min.

## RESULTS AND DISCUSSION

### Optimization of biosorption capacity

In recent years, researchers have focused on the surface and cell absorption studies with different groups of microorganisms in the removal of petroleum hydrocarbons. So, as the petroleum removal efficiency of live *Aspergillus ochraceus* discs was found as 94% in a previous study, the biosorption capacity of heat-killed *A. ochraceus* discs has also been investigated (35). Due to the ubiquity of this fungi in aquatic ecosystem, there has been a tendency to use heat-killed cells of fungi as biosorbent (30, 40, 41). The biosorption activities of *A. ochraceus* were also reported in a few studies (29, 42). It has been reported that low-cost, environmentally friendly, and easy to scale fungal biomasses are used in biosorption processes (33, 43). However, the environmental factors such as pH, temperature, and salinity should be optimized for the maximum petroleum biosorption (30).

In this study, the biosorption of petroleum with 0.5-2.5 g/100mL (1–5 pieces of disc) heat-killed fungal discs was investigated. Thus, it was determined that the highest biosorption obtained with 1.5 g/100mL heat-killed fungal discs (Figure 1a). Due to the competition and overlap between the heat-killed fungal discs, the increase in the number of discs causes a decrease in petroleum biosorption. Similarly, Kumar and Mukherji (44) reported that 0.1% algae biomass in the range of 0.1-2% (v/v) was used in the sorption of diesel and motor oil.

Biosorption of 0.5% - 5% (v/v) petroleum with heat-kil-

led fungal discs was also investigated. While a maximum biosorption was found with 1% (v/v) (96 mg/L) petroleum, a decrease was observed at values <1% and >1% (Figure 1b). Due to the complex structure of petroleum, there was a decrease in biosorption with the increasing of petroleum concentration. The certain compounds in petroleum are easily adsorbed by heat-killed cells. However, since reversible adsorption occurs in these polar compounds, the adsorbed components are released by dead cells over time (30). Similarly, Al-Hawash et al. (24) reported that petroleum hydrocarbons were adsorbed effectively by heat-killed *Aspergillus* sp. strain. The fungi with high biosorption capacity can adsorb not only petroleum hydrocarbons but also heavy metals. Accordingly, several filamentous fungi have been reported to be effective in the sorption of copper and cobalt (25). Simonescu and Ferdes (45) reported that an increasing copper ion concentration caused an increase in copper uptake, but a decrease in uptake efficiency. They also reported that the specific copper sorption of *Aspergillus oryzae* ATCC 11489, *Aspergillus oryzae* ATCC 20423, *Fusarium oxysporum* MUCL 791, and for *Polyporus squamosus*, and *Aspergillus niger* ATCC 15475 varied between 1.66 mg/g and 7.52 mg/g. Moreover, *Fusarium oxysporum* MUCL 791 showed a maximum specific copper uptake in the presence of 100 mg/L of copper ion concentration. The success of fungi in metal biosorption can be explained by their distinctive features such as solid cell wall composed of mineral ions and nitrogen, and filamentous branching growth habits (25, 46).

It is known that pH affects the biosorption by changing the chemistry of the solution, the competition of sorbate ions and the activity of the functional groups of the biosorbent (47). In this study, the biosorption of petroleum with heat-killed fungal disc was investigated in the range of pH: 4.0-8.0. Thus, a decrease was observed at values pH <5 and >5 (Figure 1c). This can be explained by the increased hydrogen ions preventing the adsorption of petroleum to the cation binding sites (48). Hence adsorption capacity decreases with increasing  $H^+$  ions. Low biosorption capacities of heat-killed fungi were obtained at pH: 4.0 due to the protonation of functional groups on the cell wall (49). Devi et al. (50) reported that pH: 4.0 was found to be optimum for the removal of organic pollutants. Similarly, Mwandira et al. (51) showed that lead removal capacity of *Oceanobacillus profundus* increased with up to pH 5 and then decreased. And another study reported that the maximum petroleum sorption with live fungal pellets of *Aspergillus* RFC-1 was observed at pH: 6.0-7.0, a decreased was detected at pH: 8.0 (24). Additionally, the optimal pH value for copper uptake of *Trametes versicolor* was reported as pH: 5.0 (52) and pH: 6.5 for *Aspergillus niger* (53). While it is known that changes in zeta potentials of petroleum at different pH levels affect biosorption, especially alkaline pH levels cause a decrease

(30, 54). Also, the low amount of adsorption at acidic pH is due to the competition between hydrogen ( $H^+$ ) and hydronium ( $H_3O^+$ ) ions for cation binding sites in the solution, low solubility of petroleum hydrocarbons, and/or precipitation of ions (55).

The biosorption amount and concentration of petrochemical waste varies depending on the contact time, the structure of chemical and the type of microorganism (56). In this study, the biosorption of petroleum with heat-killed fungal discs was investigated at contact time between 1-12 hours. So, it was found that the petroleum biosorption gradually increased over time and reached a maximum value of  $Q_e = 2.45$ . Since various *n*-alkanes, aromatics, resins and asphaltenes in the structure of petroleum were adsorbed more slowly on the surface of heat-killed fungal cells, the amount of adsorption reached equilibrium after 10<sup>th</sup> hour (Figure 1d and Figure 2). In accordance, Xu et al. (57) reported that the adsorption of petroleum on dead biomasses gradually decreases due to the sorption of only certain compounds in the petroleum at a given contact time. Al-Hawash et al. (24) showed that the maximum adsorption of naphthalene, phenanthrene and pyrene by the dead fungal biomass reached maximum level at 10<sup>th</sup> minute, but the maximum adsorption of petroleum by the dead fungal biomass was achieved at 40<sup>th</sup> minute. In addition, *Aspergillus oryzae* ATCC 20423 reached its maximum removal efficiency (88.21%) for copper on the 5<sup>th</sup> day of incubation (45).

To sum up, the optimum conditions were found to be as pH:5.0, 1% for petroleum concentration, 1.5 g/100mL for heat-killed fungal discs, 10h for contact time at room temperature ( $Q_e = 2.45$  g petroleum/g fungal disc) (Figures 1a, 1b, 1c and 1d). Besides, the specific removal rate was 0.114 with 0.004  $h^{-1}$  of abiotic loss for petroleum. The rate constant and half-life period were calculated as 1.609  $h^{-1}$ ,  $t_{1/2} = 0.431$  according to the first-order kinetics model equation. Despite its low half-life, high biosorption efficiency of the fungal strain with high-rate constant has been emphasized in the literature (37, 58). The change in the petroleum concentration with heat-killed fungal disc between 1-12 hours was shown in Figure 2.

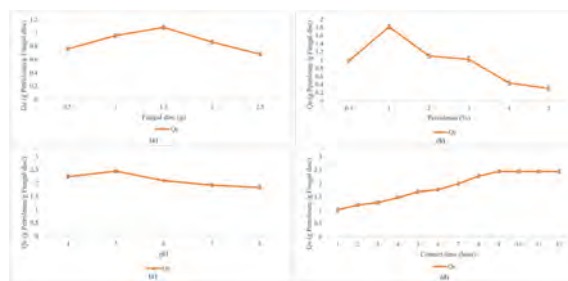


**Figure 1.** Optimization parameters for petroleum biosorption on heat-killed *A. ochraceus* discs, (a) Fungal disc (b) Petroleum concentration, (c) pH and (d) Contact time. \*Each experiment is the mean of three data and the error bars represent the standard deviation

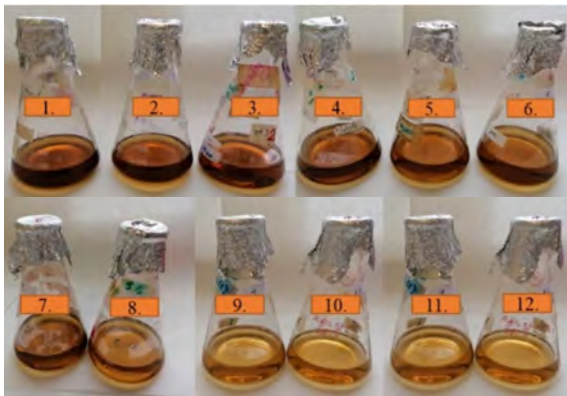


**Figure 2.** The biosorption of petroleum with heat-killed fungal disc at contact time between 1-12 hours. \*The experiments were carried out under the optimum conditions for petroleum biosorption as 1% petroleum concentration, 1.5 g/100mL heat-killed fungal discs, at pH:5.0 and room temperature.

### Kinetic study

To evaluate the rate and the mechanism of petroleum biosorption, kinetic studies were performed in terms of pseudo-first order and pseudo-second-order models with following equations (47);

The pseudo-first-order kinetic model was expressed as;

$$\ln (q_e - q_t) = \ln (q_e) - k_1 t \quad (6) \quad (59)$$

The second-order kinetic model was expressed as;

$$\frac{t}{q_t} = \left( \frac{1}{k_2 q_e^2} + \frac{t}{q_e} \right) \quad (7) \quad (60)$$

$q_e$  is the amount of adsorbed petroleum at equilibrium in g/g,  $q_t$  is the amount of adsorbed petroleum at time  $t$ ,  $k_1$  and  $k_2$  are the first and second order constants, respectively. Additionally,  $k_1$  and  $k_2$  values can be determined from the slopes of the linear plot of  $\log (q_e - q_t)$  versus  $t$  and the linear plot of  $t/q_t$  versus  $t$ , respectively (61).

When the coefficients of  $R^2$  values are examined, it is observed that the biosorption kinetic of petroleum on heat-killed *A. ochraceus* discs was well fitted with the pseudo-second order model (Figure 3). Pseudo-second kinetic model explains the kinetics of this reaction as the chemical interaction between the biosorbent and the sorbent surface in the rate-limiting step (47). Similar to our research, pseudo-second kinetic was found as the most suitable kinetic model to explain heavy metal removal with citric acid functionalized *Bougainvillea spectabilis* (7), Cd (II) removal with *B. spectabilis* (11), Alizarin Red S and Bromophenol blue dyes removal with phthalate-functionalized *Sorghum bicolor*

(8), crude oil with chitosan (62), Cr (III) removal with chemically modified *Trifolium alexandrinum* (14) and heavy metal removal with magnetic adsorbent (15). Kinetic model parameters are shown in Table 1.

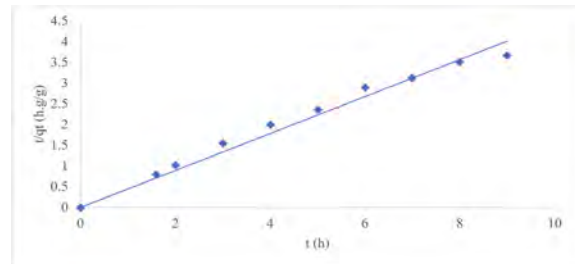


**Figure 3.** Pseudo-second order kinetic model of petroleum biosorption on heat-killed *A. ochraceus* discs. \*The experiments were carried out under the optimum conditions for petroleum biosorption as 1% petroleum concentration, 1.5 g/100mL heat-killed fungal discs, at pH:5.0 and room temperature. Each experiment is the mean of three data.

**Table 1.** Kinetic model parameters for petroleum biosorption by heat-killed *A. ochraceus* discs (pH=5.0, 1.5 g/100mL heat-killed fungal discs, 1% petroleum concentration, contact time: 10h at room temperature,  $Q_e = 2.45$  g petroleum/g fungal disc).

Kinetic model	Parameter
Pseudo-first order	$K_1$ - 0.0034 $R^2$ - 0.7066
Pseudo-second order	$K_2$ - 0.22 $R^2$ - 0.8848

### Biosorption isotherms

Langmuir and Freundlich isotherm models were applied to examine the biosorption mechanism of the petroleum by heat-killed *A. ochraceus* discs. Langmuir isotherm expresses a mono-layer system by means of the interaction between the specific homogeneous sites of the adsorbent surface and the adsorbate (61, 63). The linear form of the Langmuir isotherm is expressed as follows;

$$q_e = \frac{K_L q_m C_e}{1 + K_L C_e} \quad (8) \quad (63)$$

$R_L$  (separation factor) is used as the fundamental features of the Langmuir isotherm and expressed as;

$$R_L = \frac{1}{1 + K_L C_o} \quad (9) \quad (64)$$

The adsorption process is defined as unfavorable if  $R_L > 1$ , linear if  $R_L = 1$ , favorable if  $0 < R_L < 1$  and irreversible if  $R_L = 0$  (64).

Freundlich isotherm model expresses a multilayer sorption by means of the interaction between the heterogeneous surface of the adsorbent and the adsorbate (61). The linear form of the Freundlich isotherm is expressed as fol-

lows;

$$\ln q_e = \ln K_f + \frac{1}{n} \ln C_e \quad (10) \quad (61)$$

$q_e$  is the amount of adsorbed petroleum at equilibrium in (g/g),  $K_L$  is the Langmuir constant ( $Lg^{-1}$ ),  $q_m$  is the maximum adsorption capacity of the adsorbent (g/g) and  $C_e$  is the concentration of the adsorbent under equilibrium (g/L) (63). The slope of the linear plot of the  $(1/q_e)$  versus  $(1/C_e)$  gives  $(1/q_m K_L)$  and the intercept gives  $(1/q_m)$  in Langmuir isotherm (20) and the slope of the linear plots of  $\ln q_e$  versus  $\ln C_e$  gives  $1/n$  and  $K_f$  in Freundlich isotherm (61).

According to the results obtained from isotherm analysis of heat-killed *A. ochraceus* discs it was observed that the isotherm of heat-killed fungal discs is well fitted with the Langmuir model (Figure 4) which describes the reaction as the biosorbent adsorb on the surface of sorbent as a monolayer. Moreover, it also explains the surface of the discs is homogeneous and all sides on its surface have the same adsorption energy (62, 64). Additionally, separation factor ( $R_L$ ) is proved the favorability of this biosorption process (Table 2). Similarly, Langmuir isotherm is well fitted for the explanation of heavy metal, dye, and crude oil removal by using different sorbents in literature (7, 8, 11, 61-63, 65).

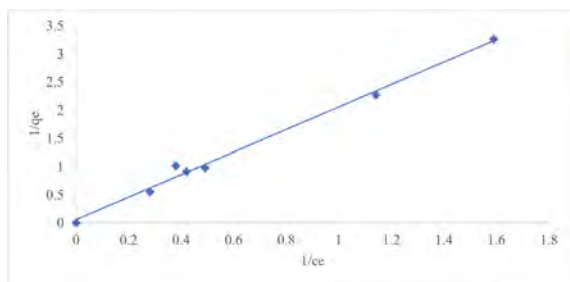


**Figure 4.** Langmuir isotherm model of petroleum biosorption on *A. ochraceus* discs. \*The experiments were carried out under the optimum conditions for petroleum biosorption as 1% petroleum concentration, 1.5 g/100mL heat-killed fungal discs, 10h contact time, at pH:5.0 and room temperature. Each experiment is the mean of three data.

**Table 2.** Isotherm model parameters for petroleum biosorption by heat-killed *A. ochraceus* discs (pH=5.0, biosorbent dose: 1.5g/100mL, 1% petroleum concentration, contact time:10h at room temperature).

Isotherm	Parameter
Langmuir	$q_{max}$ (mg/g)- 6.67
	$K_L$ (l/mg)-0.076
	$R_L$ -0.354-0.845
	$R^2$ - 0.9922
Freundlich	$K_f$ (mg/g)-2.71
	$1/n$ - 1.2069
	$R^2$ - 0.766

## Re-usability of heat-killed fungal discs

Investigating the re-usability of heat-killed fungal discs at laboratory scale is important in terms of determining the suitability of these biomaterials for industrial use. El-Gheriany et al. (19) reported that petroleum sorption decreases with each cycle of the re-usability experiment. Accordingly, although the petroleum sorption of heat-killed fungal discs decreased with each cycle, it was clearly observed that the discs could be used actively in petroleum biosorption for at least 6 more cycles (Figure 5). Similarly, Sasidharan and Kumar (15) reported that MMPSS (magnetically modified pretreated biogas slurry solid) adsorbent can be preserved with less material loss in the continuous adsorption process. In this context, it has been clearly emphasized that heat-killed fungal discs are low-cost biomaterials that can be applied on an industrial scale with their re-usability feature.

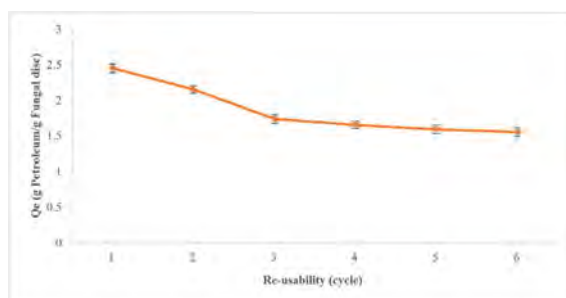


**Figure 5.** Re-usability of fungal discs for petroleum biosorption. \*The experiments were carried out under the optimum conditions for petroleum biosorption as 1% petroleum concentration, 1.5 g/100mL heat-killed fungal discs, 10h contact time, at pH:5.0 and room temperature. Each experiment is the mean of three data and the error bars represent the standard deviation.

## Focused Ion Beam Scanning Electron Microscopy (FIB-SEM)

To better understand the mechanisms involved in the binding of contaminants to the biomass surface, it is important to characterize the structure and chemical properties of the cell surface. Various environmental factors such as temperature, pH, ionic strength, availability of nutrients and natural lights affect the chemical composition of biomass (30). Accordingly, Figure 6 shows the un-treated and treated heat-killed *Aspergillus ochraceus* NRRL 3174 discs with petroleum. Moreover, the petroleum sorption on surface of heat-killed fungal disc was characterized by FIB-SEM images (Figures 6). The hyphae structure of the heat-killed fungal disc was clearly shown in Figure 7a. SEM images of heat-killed fungal discs treated with petroleum showed different morphology due to the attachment of petroleum on the

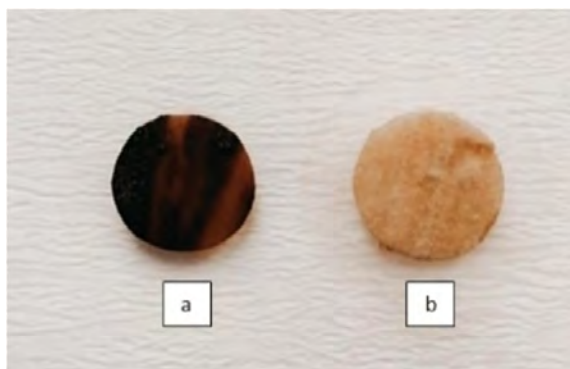


**Figure 6.** Heat-killed *Aspergillus ochraceus* NRRL 3174 discs a. treated b. un-treated form with petroleum

surface of biosorbent (Figures 7a and 7b). The heat-killed fungal discs have various functional groups (-OH, -NH, -COOH) on their surface, which supplied various sites for binding of toxic compounds (33). The adsorption efficiency of the fungal discs was positively affected by increase in the active sites due to heat denaturation operation on the cell wall proteins. It is also suggested that heat increases the hydrophilicity of the fungal biomass by remo-

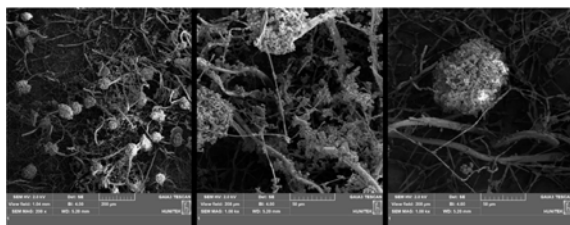


**Figure 7a.** FIB-SEM images of fungal discs before the biosorption of petroleum.

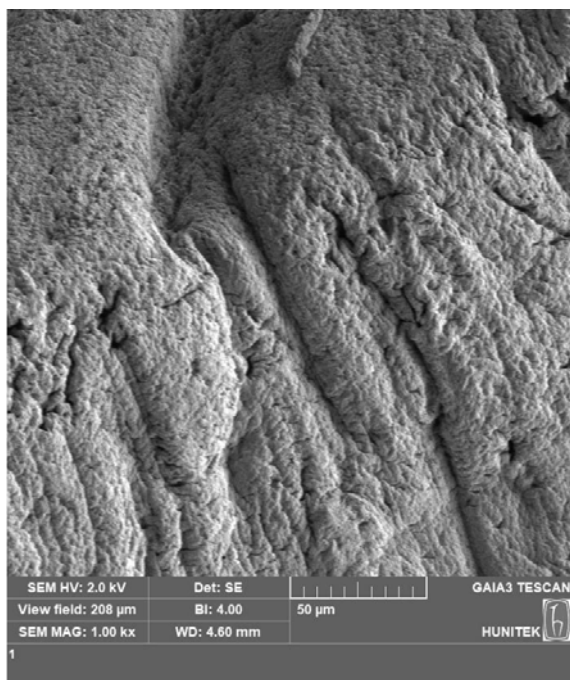


**Figure 7b.** FIB-SEM images of fungal discs after the biosorption of petroleum

ving -CH<sub>3</sub> groups responsible for the hydrophobic nature of the cell wall. Also, autoclaving disrupts the fungal cell integrity, resulting in greater porosity. As a result, more petroleum molecules can be fixed on the enlarged pores of the heat-killed fungal biomass (43).

## GC-MS

Table 3 represents the *n*-alkane concentrations (ppm) of petroleum content before and after biosorption. According to Table 3, the removal of *n*-alkane fractions of petroleum by heat-killed *A. ochraceus* discs was also calculated in Figure 8. Figure 8. clearly shows that the *n*-alkane fractions in the range of C<sub>10</sub> - C<sub>14</sub> were removed above 90%; C<sub>15</sub> - C<sub>21</sub>, C<sub>28</sub> and C<sub>30</sub> - C<sub>36</sub> were removed around and above 80%; C<sub>22</sub> - C<sub>27</sub>, C<sub>29</sub> were also removed approximately 65% - 75%. It was detected that short-chain- and some of medium-chain *n*-alkanes of petroleum were bio-sorbed by heat-killed fungal discs over 90% and 80%, respectively. The most striking result is that the sorption of long-chain *n*-alkanes by heat-killed fungal disc was over 80%. In similar studies, the bio removal of petroleum was approved by GC-MS analysis (66-68). Short and long-chain *n*-alkanes are the most common components of the petroleum. Short-chain *n*-alkanes are highly toxic, while long-chain *n*-alkanes are solid, low soluble, and less bio-available, and persist in the environment for a long time. Therefore, the biosorption of long-chain *n*-alkanes is of great importance for environmental remediation (69, 70).

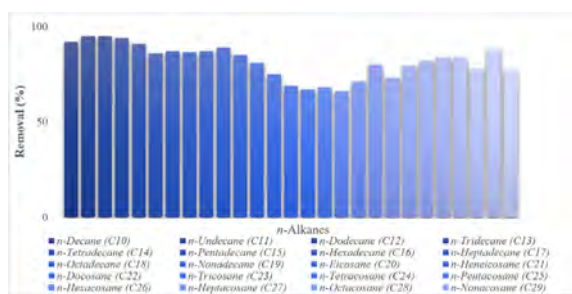


**Figure 8.** The removal of *n*-alkane fractions of petroleum by heat-killed fungal disc. \*The experiment was carried out under the optimum conditions for petroleum biosorption as 1% petroleum concentration, 1.5 g/100mL heat-killed fungal discs, 10h contact time, at pH:5.0 and room temperature.

## CONCLUSION

Fungal biomass has great advantageous to be used as biosorbent due to their high growth and reproduction rates, capability to use various carbon sources, and ability to adapt to adverse environmental conditions. In this context, the heat-killed fungal discs obtained from *Aspergillus ochraceus* were used as biosorbent in the biosorption process of petroleum. For the maximum biosorption, various parameters were optimized as pH:5.0, 1% petroleum concentration, 1.5 g/100mL heat-killed fungal discs, and

**Table 3.** Gas chromatography-mass spectrometry analysis of petroleum

<b>n-Alkane fractions</b>	<b>Initial</b>	<b>*Remaining</b>
<i>n</i> -Decane (C <sub>10</sub> ), ppm	151.3	12.2
<i>n</i> -Undecane (C <sub>11</sub> )	219.4	11.4
<i>n</i> -Dodecane (C <sub>12</sub> )	239.0	12.5
<i>n</i> -Tridecane (C <sub>13</sub> )	246.7	14.5
<i>n</i> -Tetradecane (C <sub>14</sub> )	227.3	20.9
<i>n</i> -Pentadecane (C <sub>15</sub> )	258.7	37.2
<i>n</i> -Hexadecane (C <sub>16</sub> )	225.1	29.4
<i>n</i> -Heptadecane (C <sub>17</sub> )	249.6	33.7
<i>n</i> -Octadecane (C <sub>18</sub> )	195.6	24.9
<i>n</i> -Nonadecane (C <sub>19</sub> )	213.1	22.8
<i>n</i> -Eicosane (C <sub>20</sub> )	187.0	28.5
<i>n</i> -Heneicosane (C <sub>21</sub> )	193.6	36.8
<i>n</i> -Docosane (C <sub>22</sub> )	198.4	50.0
<i>n</i> -Tricosane (C <sub>23</sub> )	222.5	69.1
<i>n</i> -Tetracosane (C <sub>24</sub> )	235.8	78.5
<i>n</i> -Pentacosane (C <sub>25</sub> )	239.2	77.5
<i>n</i> -Hexacosane (C <sub>26</sub> )	181.7	61.5
<i>n</i> -Heptacosane (C <sub>27</sub> )	149.6	43.7
<i>n</i> -Octacosane (C <sub>28</sub> )	111.4	30.1
<i>n</i> -Nonacosane (C <sub>29</sub> )	93.8	22.3
<i>n</i> -Triacontane (C <sub>30</sub> )	70.1	15.1
<i>n</i> -Hentriacontane (C <sub>31</sub> )	67.8	12.3
<i>n</i> -Dotriacontane (C <sub>32</sub> )	56.7	9.28
<i>n</i> -Tritriacontane (C <sub>33</sub> )	49.2	7.70
<i>n</i> -Tetracontane (C <sub>34</sub> )	40.8	8.95
<i>n</i> -Pentatriacontane (C <sub>35</sub> )	30.7	<3.78
<i>n</i> -Hexatriacontane (C <sub>36</sub> )	12.3	<2.81
<i>n</i> -Octatriacontane (C <sub>38</sub> )	<5.73	<5.73
<i>n</i> - Tetracontane (C <sub>40</sub> )	<6.93	<6.93

\* The results show the remaining *n*-alkane fractions of the petroleum  
 \*The values are given in ppm (parts-per million)

10h contact time at room temperature. The interaction of the adsorbent with the petroleum in the aqueous phase followed pseudo-second order kinetics. The Langmuir isotherm, which is the best fit for petroleum biosorption, indicates that physisorption plays a major role in biosorption process. In addition, the reuse of heat-killed fungal disc, which is effective, low-cost, and environmentally friendly, in a wide variety of industrial areas was also emphasized in this study. It should be considered that no similar study has been found investigating the sorption of petroleum with heat-killed *Aspergillus ochraceous* discs. This study pointed out the use of *Aspergillus ochraceous* discs as an efficient biosorbent in the biosorption process of petroleum. The results should be supported by further studies to increase its biosorption capacity and to fill the existing gaps.

## ACKNOWLEDGEMENT

This work is funded by Hacettepe University Scientific Research Projects Coordination Unit (Project number: FHD-2019-17719).

## CONFLICT OF INTEREST

The authors declare that they have no conflict of interest.

## AUTHOR CONTRIBUTION

All authors contributed to the study conception and design. Project administration, Conceptualization, Investigation, Methodology, Writing-original draft, and editing were performed by [Nermin Hande Avcioglu] and [Sezen Bilen Ozyurek]; Resources, Data curation and Software were carried out by [Nermin Hande Avcioglu] and Funding acquisition by [Sezen Bilen Ozyurek]. The first draft of the manuscript was written by [Nermin Hande Avcioglu], [Sezen Bilen Ozyurek], [Isil Seyis Bilkay] and all authors read and approved the final manuscript.

## REFERENCES

- Pi Y, Chen B, Bao M, Zhang B. Microbial degradation of four dispersed crude oils by *Rhodococcus* sp. evaluated using carbon stable isotope analysis. *J Chem Technol Biotechnol* 2019; 94 (6): 1800–7.
- Chen ZK, An C, Boufadel M, Owens E, Chen Z, Lee K, Cao Y, Cai M. Use of surface-washing agents for the treatment of oiled shorelines: Research advancements, technical applications and future challenges. *Chem Eng J* 2020; 391: 123565.
- Liu B, Chen B, Zhang B, Song X, Zen G, Lee K. Photocatalytic ozonation of offshore produced water by TiO<sub>2</sub> nanotube arrays coupled with UV-LED Irradiation. *J Hazard Mater* 2020; 40: 123456.
- Tian Y, Li J, Whitcombe TW, McGill WB, Thring R. Application of oily sludge-derived char for lead and cadmium removal from aqueous solution. *Chem Eng J* 2020; 384: 123386.
- Zhu Z, Zhang B, Cai Q, Ling J, Lee K, Chen B. Fish waste based lipopeptide production and the potential application as a bio-dispersant for oil spill control. *Front Bioeng Biotechnol* 2020; 8: 734.
- Kapahi M, Sachdeva S. Bioremediation options for heavy metal pollution. *J Heal Pollut* 2019; 9 (24): 191203.
- Nazir H, Salman M, Athar M, Farooq U, Wahab A, Akram M. Citric acid functionalized *Bougainvillea spectabilis*: a novel, sustainable, and cost-effective biosorbent for removal of heavy metal (Pb<sup>2+</sup>) from wastewater. *Water Air Soil Pollut* 2019; 230: 1-16.
- Akram M, Salmana M, Farooq U, Saleem U, Tahir S, Nazira H, Arsalan HM. Phthalate-functionalized *Sorghum bicolor* L.; an effective biosorbent for the removal of alizarin red S and bromophenol blue dyes from simulated wastewater. *Desalin Water Treat* 2020; 190: 383-92.
- Shen J, Huang G, An C, Zha S, Rosendahl S. Immobilization of tetrabromobisphenol a by pinecone-derived biochars at solid-liquid interface: synchrotron-assisted analysis and role of inorganic

- fertilizer ions. *Chem Eng J* 2017; 321: 346–57.
10. Cai L, Zhang Y, Zhou Y, Zhang X, Ji L, Song W, Zhang H, Liu J. Effective adsorption of diesel oil by crab-shell-derived biochar nanomaterials. *Materials* 2019;12 (2): 236.
  11. Nazir H, Salman M, Athara M, Farooq U, Akrama M, Saleem N. A novel biosorbent *B. spectabilis* stalks leaves for removal of Cd (II) and Cu (II) from wastewater. *Desalin Water Treat* 2019; 148: 222–28.
  12. Hess BJ, Kolar P, Classen JJ, Knappe D, Cheng JJ. Effects of co occurring species present in swine lagoons on adsorption of copper on eggshell. *Int J Environ Res* 2019; 13: 613–22.
  13. Joseph EE, Azorji, JN, Iheanacho JC, Nwachukwu CU, Iheagwam KS, Okoli CJ. Adsorption of petroleum hydrocarbons from crude oil polluted soil using agro-waste. *J Environ Treat Tech* 2022; 10 (4): 284–89.
  14. Saleem U, Akram M, Salman M, Farooq U, Dar A, Tahir S. Biosorption activity of chemically modified *Trifolium alexandrinum* for the detoxification of Cr (III) contaminated water. *Desalin water Treat* 2022; 246: 212–25.
  15. Sasidharan R, Kumar A. Magnetic adsorbent developed with alkali thermal pretreated biogas slurry solids for the removal of heavy metals: optimization, kinetic, and equilibrium study. *Environ Sci Pollut Res* 2022; 29 (20): 30217–32.
  16. Olivella MÀ, Jové P, Bianchi A, Bazzicalupi C, Cano L. An integrated approach to understanding the sorption mechanism of phenanthrene by cork. *Chemosphere* 2013; 90 (6): 1939–44.
  17. Christensen KM, Rorrer GL. Equilibrium partitioning behavior of naphthalene and phenanthrene with axenic microplantlets of the temperate green seaweed *Acrosiphonia coalita*. *Chemosphere* 2009; 76 (8): 1135–42.
  18. Hussein M, Amer AA, Zahran HF, Ali SM, Elgohary M, Nasr M. Agricultural waste as a biosorbent for oil spills. *Int J Dev* 2013; 2 (1): 127–35.
  19. El Gheriany IA, El Saqa FA, Amer AAER, Hussein M. Oil spill sorption capacity of raw and thermally modified orange peel waste. *Alex Eng J* 2020; 59(2): 925–32.
  20. Al Zubaidi I, Al Zubaidi M, Tajik M, Al Zubaidi M, Al Mutair M, Sheikh M, Chen Y, Al-Yasiri M, Alsudays A. Pomegranate peels powder for the remediation of oil polluted water from waste lubricating oil. *Proceedings of the 5th International Conference of Fluid Flow, Heat and Mass Transfer, Niagara Falls, Canada, 2018.*
  21. Wu J, Yu HQ. Biosorption of 2,4-dichlorophenol from aqueous solution by *Phanerochaete chrysosporium* biomass: isotherms, kinetics, and thermodynamics. *J Hazard Mater* 2006; 137: 498–508.
  22. Chung M, Tsui MT, Cheung K, Tam NF, Wong MH. Removal of aqueous phenanthrene by brown seaweed *Sargassum hemiphyllum*: Sorptionkinetic and equilibrium studies. *Sep Purif Technol* 2007; 54 (3): 355–62.
  23. Crognale S, Annibale AD, Pesciaroli L, Stazi SR. Fungal community structure and as-resistant fungi in a decommissioned gold mine site. *Front Microbiol* 2017; 8: 2202.
  24. Al-Hawash AB, Zhang X, Ma F. Removal and biodegradation of different petroleum hydrocarbons using the filamentous fungus *Aspergillus* sp. RFC-1. *Microbiol Open* 2019; 8 (1): e00619.
  25. Dusengemungu L, Kasali G, Gwanama C, Ouma KO. Recent Advances in Biosorption of Copper and Cobalt by Filamentous Fungi. *Front Microbiol* 2020; 11: 582016.
  26. Shah SS, Palmieri MC, Sponchiado SRP, Bevilacqua D. Enhanced bio-recovery of aluminum from low-grade bauxite using adapted fungal strains. *Braz J Microbiol* 2020; 51: 1909–18.
  27. Oladipo OG, Awotoye OO, Olayinka A, Bezuidenhout CC, Maboeta MS. Heavy metal tolerance traits of filamentous fungi isolated from gold and gemstone mining sites. *Braz J Microbiol* 2018; 49: 29–37.
  28. Chen L, Li E, Wu W, Wang G, Zhang J, Guo X, Xing F. The secondary metabolites and biosynthetic diversity from *Aspergillus ochraceus*. *Front in Chem* 2022; 10: 938626.
  29. Hareeri RH, Aldurdunji MM, Abdallah HM, Alqarni AA, Mohamed SGA, Mohamed GA, Ibrahim SRM. *Aspergillus ochraceus*: metabolites, bioactivities, biosynthesis, and biotechnological potential. *Molecules* 2022; 27 (19): 6759.
  30. Vahabisani A, An C. Use of biomass derived adsorbents for the removal of petroleum pollutants from water: a mini review. *Environ Syst Res* 2021; 10 (1): 1–10.
  31. Rao J, Viraraghavan T. Biosorption of phenol from an aqueous solution by *Aspergillus niger* biomass. *Bioresour Technol* 2002; 85 (2): 165–71.
  32. Kumar R, Bishnoi NR, Bishnoi K. Biosorption of chromium (VI) from aqueous solution and electroplating wastewater using fungal biomass. *Chem Eng J* 2008; 135 (3): 202–8.
  33. Lu N, Hua T, Zhai Y, Qin H, Aliyeva J, Zhang H. Fungal cell with artificial metal container for heavy metals biosorption: Equilibrium, kinetics study and mechanisms analysis. *Environ Res* 2020; 182: 109061.
  34. Raghukumar C, Shailaja M, Parameswaran P, Singh S. Removal of polycyclic aromatic hydrocarbons from aqueous media by the marine fungus NIOCC 312: Involvement of lignin-degrading enzymes and exopolysaccharides. *Indian J Mar Sci* 2006; 35 (4): 373–79.
  35. Bilen Ozyurek S, Avcioglu NH, Seyis Bilkay I. Mycoremediation potential of *Aspergillus ochraceus* NRRL 3174. *Arch Microbiol* 2021; 203: 5937–50.
  36. Mohammadi M, Sedighi M, Hemati M. Removal of petroleum asphaltene by improved activity of NiO nanoparticles supported on green AlPO-5 zeolite: process optimization and adsorption isotherm. *Petroleum* 2020; 6 :182–88.
  37. Benguenab A, Chibani A. Biodegradation of petroleum hydrocarbons by filamentous fungi (*Aspergillus ustus* and *Purpureocillium lilacinum*) isolated from used engine oil contaminated soil. *Acta Ecologica Sinica* 2021; 41 (5): 416–23.
  38. Bilen Ozyurek S, Seyis Bilkay I. Comparison of petroleum biodegradation efficiencies of three different bacterial consortia determined in petroleum contaminated waste mud pit. *SN Appl Sci* 2020; 2: 1–12.
  39. Kachieng'a L, Momba MNB. Kinetics of petroleum oil biodegradation by consortium of three protozoan isolates (*Aspidisca* sp., *Trachelophyllum* sp. and *Peranema* sp.). *Biotechnol Rep* 2017; 15: 125–31.
  40. Cheng Z, Feng K, Su Y, Ye J, Chen D, Zhang S, Zhang X, Dionysiou DD. Novel biosorbents synthesized from fungal and bacterial biomass and their applications in the adsorption of volatile organic compounds. *Bioresour Technol* 2020; 300: 122705.
  41. Kim N, Seo JH, Yun YS, Park D. New insight into continuous recirculation process for treating arsenate using bacterial biosorbent. *Bioresour Technol* 2020; 316: 123961.
  42. Saratale GD, Kalme SD, Govindwar SP. Decolorisation of textile dyes by *Aspergillus ochraceus* (NCIM-1146). *Ind J Biotechnol* 2006; 5: 407–10.
  43. Legorreta-Castañeda AJ, Lucho-Constantino CA, Beltrán-Hernández RI, Coronel-Olivares C, Vázquez-Rodríguez GA. Biosorption of water pollutants by fungal pellets. *Water* 2020; 12 (4): 1155.
  44. Kumar Mishra P, Mukherji S. Biosorption of diesel and lubricating oil on algal biomass. *3 Biotech* 2012; 2: 301–10.
  45. Simonescu CM, Ferdes M. Fungal biomass for Cu (II) uptake from aqueous systems. *Pol J Environ Stud* 2012; 21 (6): 1831–39.



46. Latha JNL, Babu PN, Rakesh P, Kumar KA, Anupama M, Susheela L. Fungal cell walls as protective barriers for toxic metals. *Adv Med Biol* 2012; 53: 181-98
47. Boleydei H, Mirghaffari N, Farhadian O. Comparative study on adsorption of crude oil and spent engine oil from seawater and freshwater using algal biomass. *Environ Sci Pollut Res* 2018; 25: 21024-35.
48. Jalali R, Ghafourian H, Asef Y, Davarpanah S, Sepehr S. Removal and recovery of lead using nonliving biomass of marine algae. *J Hazard Mater* 2002; 92 (3): 253–62.
49. Aracagok YD. Biosorption of lead by a soil isolate *Aspergillus neoalliaceus*. *Arch Microbiology* 2022; 204 (9): 547.
50. Devi MG, Al-Hashmi ZS, Sekhar GC. Treatment of vegetable oil mill effluent using crab shell chitosan as adsorbent. *Int J Environ Sci Technol* 2012; 9: 713–18.
51. Mwandira W, Nakashima K, Kawasaki S, Arabelo A, Banda K, Nyambe I, Chirwa M, Ito M, Sato T, Igarashi T, Nakata H, Nakayama S, Ishizuka M. Biosorption of Pb (II) and Zn (II) from aqueous solution by *Oceanobacillus profundus* isolated from an abandoned mine. *Sci Rep* 2020; 10 (1): 21189.
52. Tsekova T, Todorova D, Dencheva V, Ganeva S. Biosorption of copper (II) and cadmium (II) from aqueous solutions by free and immobilized biomass of *Aspergillus niger*. *Bioresour Technol* 2010; 101 (6): 1727-31.
53. Tsekova T, Todorova D, Ganeva S. Removal of heavy metals from industrial wastewater by free and immobilized cells of *Aspergillus niger*. *Int Biodeterior Biodegrad* 2010; 64 (6): 447-51.
54. Lim MW, Von Lau E, Poh PE A. A comprehensive guide of remediation technologies for oil contaminated soil—present works and future directions. *Mar Pollut Bull* 2016; 109 (1): 14–45.
55. Zhou JL, Kiff RJ. The uptake of copper from aqueous solution by immobilized fungal biomass. *J Chem Technol Biot* 1991; 52 (3): 317–30.
56. Hasan IF. Role of filamentous fungi to remove petroleum hydrocarbons from the environment, In *Microbial Action on Hydrocarbons*, Springer, Singapore; 2019.
57. Xu N, Bao M, Sun P, Li Y. Study on bioadsorption and biodegradation of petroleum hydrocarbons by a microbial consortium. *Bioresour Technol* 2013; 149: 22–30.
58. Barnes NM, Khodse VB, Lotlikar NP, Meena RM, Damare SR. Bioremediation potential of hydrocarbon-utilizing fungi from select marine niches of India. *3 Biotech* 2018; 8: 1-10.
59. Sokker HH, El-Sawy NM, Hassan MA, El-Anadoul BE. Adsorption of crude oil from aqueous solution by hydrogel of chitosan-based polyacrylamide prepared by radiation induced graft polymerization. *J Hazard Mater* 2011; 190 (1-3): 359-65.
60. Singh S, Parveen N, Gupta H. Adsorptive decontamination of rhodamine-B from water using banana peel powder: a biosorbent. *Environ Technol Innov* 2018; 12: 189-95.
61. Peng D, Ouyang F, Liang X, Guo X, Dang Z, Zheng L. Sorption of crude oil by enzyme-modified corn stalk vs. chemically treated corn stalk. *J Mol Liq* 2018; 255: 324-32.
62. Mottaghi H, Mohammadi Z, Abbasi M, Tahouni N, Panjeshahi MH. Experimental investigation of crude oil removal from water using polymer adsorbent. *Journal of Water Process Engineering* 2021; 40: 101959.
63. Mallampati R, Xuanjun L, Adin A, Valiyaveettil S. Fruit peels as efficient renewable adsorbents for removal of dissolved heavy metals and dyes from water. *ACS Sustain Chem Eng* 2015; 3 (6): 1117-1124.
64. Zhang B, Yu S, Zhu Y, Shen Y, Gao X, Shi W, Tay JH. Adsorption mechanisms of crude oil onto polytetrafluoroethylene membrane: kinetics and isotherm, and strategies for adsorption fouling control. *Sep Purifi Technol* 2020; 235: 116212.
65. Yu X, He Y. Optimal ranges of variables for an effective adsorption of lead (II) by the agricultural waste pomelo (*Citrus grandis*) peels using Doehlert designs. *Sci Rep* 2018; 8 (1): 729.
66. Liang J, Cheng T, Huang Y, Liu J. Petroleum degradation by *Pseudomonas* sp. ZS1 is impeded in the presence of antagonist *Alcaligenes* sp. CT10. *AMB Expr* 2018; 8 (1): 1-13.
67. Al-Dhabi NA, Esmail GA, Arasu MV. Enhanced production of biosurfactant from *Bacillus subtilis* strain Al-dhabi-130 under solid-state fermentation using date molasses from Saudi Arabia for bioremediation of crude-oil-contaminated soils. *Int Env Res Pub He* 2020; 17 (22): 8446.
68. Luo X, Chen L, Zhao S, Lei Z, Xia M, Zhang C. Study of the characteristics of two immobilized microbial materials in degradation and evolution of petroleum hydrocarbon. *ACS Omega* 2020; 5 (31): 19402–8.
69. Guo H, Tang S, Xie S, Wang P, Huang C, Geng X, Jia X, Huo H, Li X, Zhang J, Zhang Z, Fang J. The oil removal and the characteristics of changes in the composition of bacteria based on the oily sludge bio electrochemical system. *Sci Rep* 2020; 10 (1): 15474.
70. Liu S, Yuan W, Yang X, Li C, Ji Y, Feng X, Li M, Xie Y. Microbial degradation of petroleum characteristic pollutants in hypersaline environment, emphasizing n-hexadecane and 2,4 di-tert-butylphenol. *Environ Monit Assess* 2023; 195 (6): 771.

# Cobalt boride ( $\text{Co}_2\text{B}$ ) particle synthesis by one-step carbothermic reduction

Levent Kartal 

 Hitit University, Department of Metallurgical and Materials Engineering, Corum, Türkiye

## ABSTRACT

In this study, crystalline  $\text{Co}_2\text{B}$  powder production was carried out by a one-step carbothermic reduction method starting from cheap, easily accessible oxide-based materials. Firstly, to determine the carbothermic  $\text{Co}_x\text{B}$  formation conditions, the decomposition temperatures of the raw materials were analysed by TG/DTA, and the temperature-varying Gibbs free energies of the expected reactions were calculated. Then,  $\text{Co}_2\text{B}$  production was carried out at constant  $\text{CoO/B}_2\text{O}_3/\text{C}$  (3.22/1.5/1.3) weight ratios at temperature (1273-1473 K) and time (30-270 min). Scanning electron microscopy (SEM), X-ray diffraction (XRD), and vibrating sample magnetometer (VSM) were used to characterize the particles. XRD results showed that reaction temperature and time are the primary control on  $\text{Co}_x\text{B}$  formation and single-phase crystalline  $\text{Co}_2\text{B}$  particles with crystallite sizes of 88 nm were successfully produced at 1473 K and 150 min. The permanent magnetization, saturation magnetization, and coercivity values of  $\text{Co}_2\text{B}$  particles were defined as 16.58 Oe, 35.361 emu/g, 0.501 emu/g, respectively.

## Keywords:

Cobalt boride, cobalt, carbothermic reduction, cobalt alloy

## INTRODUCTION

Cobalt is a crucial component used in industrial, military, and medical uses [1-3]. The most crucial utilization parts of cobalt and its alloys are super alloys, batteries, catalysts, magnetic alloys, high-speed steels, and cemented carbides [4]. In recent years, among Co alloys, cobalt borides ( $\text{Co}_x\text{B}$ ) stand out with their high hardness, excellent wear resistance and superior magnetic and catalytic properties. Due to these superior properties, studies have been carried out on using cobalt borides in many areas, such as improving prosthetic alloys' corrosion and wear properties, and catalyst material for hydrogen production systems and fuel cells [5-9].

The production of  $\text{Me}_x\text{B}$  can be accomplished using a variety of processes, such as the direct solid-state reaction of elements [10-12], chemical reduction [13-15], molten salt electrolysis [16-18], mechanochemical [19], and electric arc technique [20]. The corrosion and wear resistance of cobalt-based alloys (CoCrMo) used in producing orthopaedic prostheses is provided by thin boride films formed on the surface. The boride film on the surface of these alloys is formed by a molten salt electrolysis and thermochemical processes [5-7]. Ruiz et al. [21] formed a boride film on the surface of CoCrMo alloys by thermochemical processes and observed

that hardness and tribo-corrosion properties increased.  $\text{Co}_x\text{B}$  compounds are also used to enhance the surface properties of mild steels owing to their high hardness and wear resistance. Baris et al. [22] coated the surface of S235JRC carbon steel with mechanochemically produced  $\text{Co}_2\text{B}$  particles using a laser and investigated its machinability properties. In addition to improving surface properties, it is also used as reinforcing particles in metal matrix composites. Khoshshima et al. [23] used CoB-TiB<sub>2</sub> particles produced by chemical reduction to improve the properties of parts produced from Ti6Al4V particles by additive manufacturing.  $\text{Co}_x\text{B}$  particles have drawn attention in recent years, particularly with their catalytic properties in hydrogen production and storage, and studies in this field have intensified. The production of particles for catalyst applications of hydrogen storage and production systems is carried out using high-temperature solid-state synthesis, chemical reduction and mechanochemical methods starting from elemental Co and B [8-15,19,20, 24, 25].

Most methods used in producing cobalt boride ( $\text{Co}_2\text{B}$ ) particles are unsuitable for industrial production due to limitations such as high raw material cost, multi-step and long experimental procedures, and high-cost specialized equipment requirements. Industrial ma-

## Article History:

Received: 2023/03/31

Accepted: 2023/07/04

Online: 2023/09/30

Correspondence to: Levent Kartal,

E-Mail: leventkartal@hitit.edu.tr

Phone: +90 364 2191200

Fax: +90 364 2191310

This article has been checked for similarity.



This is an open access article under the CC-BY-NC licence

<http://creativecommons.org/licenses/by-nc/4.0/>

## Cite as:

Kartal L, "Cobalt boride ( $\text{Co}_2\text{B}$ ) particle synthesis by one-step carbothermic reduction". *Hittite J Sci Eng.* 2023;10 (3): 229-235. doi:10.17350/hjse19030000311

manufacturing prefers simple, quick synthesis processes with minimal production costs. In producing metal borides, carbothermic reduction stands out with its low cost, one-step, simple and fast production possibilities [26, 27]. The most well-known example of the carbothermic reduction in metal boride production is ferrobor (FeB) production. Ferrobor, used as an additive in the iron and steel industry, has been produced by the carbothermic reduction method for a long time [28, 29]. In this method, metal oxide and a  $B_2O_3/H_3BO_3$  combination are heated with carbon to produce carbothermic metal borides. The most significant parameters in carbothermic metal boride production are the Me:B ratio of the oxide mixture, temperature, and reaction time.

In this study, the synthesis of crystalline single  $Co_xB$  phase particles by a simple, fast and one-step carbothermic reduction process was carried out using  $CoO$ ,  $B_2O_3$  and  $C$ . Thermo-gravimetric/differential thermal analysis (TG/DTA) analysis of the raw material and the Gibbs free energy change graphs of the reactions with temperature were used to determine the mechanism of  $Co_xB$  formation. The phase structure of  $Co_xB$  particles was studied in detail by XRD, morphology by SEM and magnetic properties by VSM.

## MATERIAL AND METHODS

In the synthesis of  $Co_xB$  powder, cobalt oxide ( $CoO$ ) was used as Co resource, diboron trioxide ( $B_2O_3$ ) (>97%) as B resource and carbon (>99%) as a reductant. Stoichiometric weight ratios of constant  $CoO/B_2O_3/C$  were used as 3.22/1.5/1.3 in the experiments. The investigated process parameters are summarized in Table I.

**Table 1.** Experimental parameters of carbothermic  $Co_xB$  synthesis.

Group	Weight ratio ( $CoO/B_2O_3/C$ )	Parameter	Experiment conditions	Variables
I	3.22/1.5/1.3	Temperature	150 min	1273 K, 1373 K, 1473 K
II		Time	1473 K	30 min, 150 min, 270 min

Before the synthesis, the powders constituting the raw material were mixed using agate mortar. Then powder mixture was fed into the furnace in alumina boats. The experiments were conducted under an argon atmosphere, and the argon flow was constant at 0.5 L/min during heating, reaction, and cooling. Each experiment's heating rate was 283 K / minute. The synthesis steps and schematic depiction of the experimental setup are shown in Fig. 1.

After synthesis, the products were leached with hot water to remove unreacted compounds and dried at 353 K for 2 hours.

The analyses of the raw materials and obtained products was carried out using thermo-gravimetric/differential

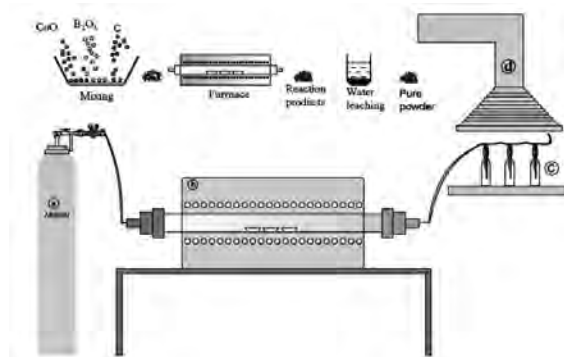


**Figure 1.** Schematic depiction of the experimental setup (a) argon cylinder (b) furnace (c) gas washing bottle (d) fume hood.

thermal analysis (TG/DTA-HITACHI-STA7300), X-Ray diffractometer (XRD-(PANalytical X-Pert3 Powder)), scanning electron microscopy (SEM- ZEISS EVO LS 10) and vibrating sample magnetometer (VSM-Lake Shore 7407). Gibbs free energy ( $\Delta G$ ) values of the predicted reactions obtained with the help of HSC 5.1 software.

To calculate the crystal size of single-phase particles, the Scherrer equation was utilized. Scherrer equation for the calculation of particle crystal size is;

$$D = k\lambda / \beta \cos \theta \quad (1)$$

where  $\beta$  is the Full width at half maximum (FWHM) of the peak,  $\theta$  is the Bragg angle,  $\lambda$  is the wavelength of the used X-ray beam (1.54), and  $K$  is the Scherrer constant [30].

## RESULTS AND DISCUSSION

### Carbothermic synthesis mechanism of $Co_xB$

TG/DTA results and Gibbs free energy ( $\Delta G$ ) values of the predicted reactions were used to determine the carbothermic  $Co_xB$  synthesis mechanism. Firstly, the thermal behaviour of the mixed powders was investigated at a warming rate of 283 K/min to determine the thermal decomposition temperatures. The obtained TG/DTA curve is given in Fig. 2. In the TG graph, a low weight decrease occurred initially due to moisture loss of the powder mixture and then little weight change was observed up to 900 K. Between 900-1173 K the weight change increased compared to the weight change between 473-900 K. Above 1173 K, a sharp weight loss was observed, which may be due to the formation of CO gas. Four typical endothermic peaks were identified in the DTA curve given in Fig. 2. The first endothermic peak occurred at 404 K because of the removal of the water contained in the mixture. Second, endothermic peaks at 1109 K are believed to be caused by the reduction of the powder mixture, such as Co and B from  $CoO$  and  $B_2O_3$ , while the third endothermic peaks at 1172 K are thought to be due to the formation of the  $Co_xB$  phase and fourth peak at 1226 is thought to be due to the formation of the  $CoB$ . TG/DTA analysis reve-

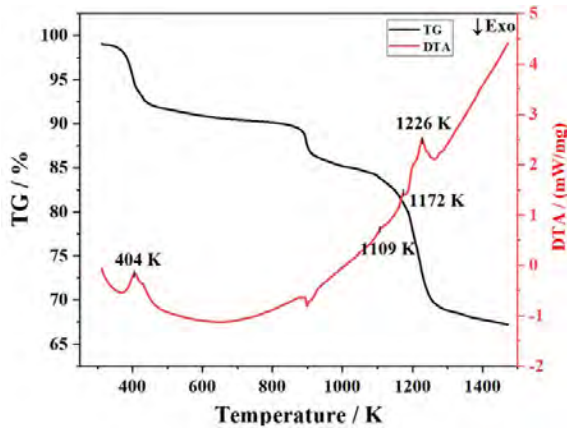
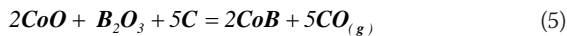
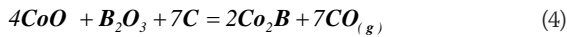
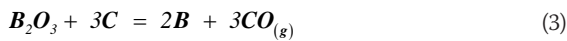
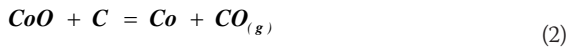


**Figure 2.** TG/DTA curves of CoO/B<sub>2</sub>O<sub>3</sub>/C at warming rate of 20 °C min<sup>-1</sup>.

als that the appropriate carbothermic synthesis temperature for producing Co<sub>x</sub>B using the CoO/B<sub>2</sub>O<sub>3</sub>/C powder mixture is above 1226 K.

In addition to the TG/DTA analysis, the Gibbs free energies of the predicted reactions were calculated to determine the mechanism of Co<sub>x</sub>B formation. The temperature-dependent Gibbs free energy changes of the reactions are given in Fig. 3. Carbothermic CoB production proceeds in the following steps:



When the graph in Fig. 3 is examined, it is seen that CoO can be reduced via C thermodynamically at 773 K, Co<sub>2</sub>B can be produced at 1033 K, and CoB can be synthesized at 1218 K and higher temperatures.

Fig. 3 reveals that CoO will undergo reduction first in accordance with reaction (2). The carbothermic reduction of B<sub>2</sub>O<sub>3</sub> alone (3) is not thermodynamically possible at the

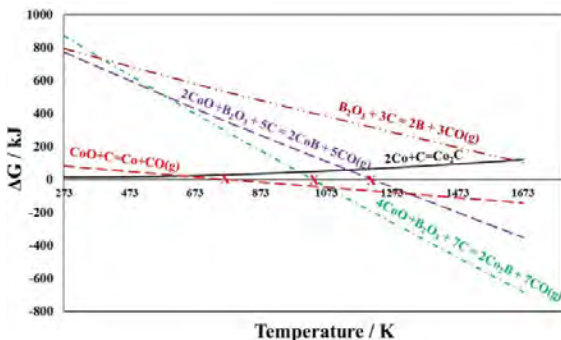


**Figure 3.** Gibbs free energies of reactions (2)–(5) change with temperature.

proposed reaction temperatures. The carbothermic reduction of B<sub>2</sub>O<sub>3</sub> in the presence of CoO to form Co<sub>2</sub>B and CoB according to reactions (4) and (5) appears to occur. Considering the Co-B diagram and the literature, stable Co<sub>x</sub>B compounds were identified, and according to these compounds' formation reactions were deduced [31]. Co<sub>x</sub>B production proceeds in the following steps:



The temperature-varying Gibbs free energy of the formation graph of the proposed reactions is given in Fig. 4. Diffusion-based thermochemical synthesis of Co<sub>x</sub>B occurs by diffusion of B into Co particles with the driving force of B concentration gradient and temperature (equations 6-9). The first product formed on the surface of Co particles by B diffusion is thermodynamically always the boride compound (Co<sub>2</sub>B) with the lowest mole fraction of boron (equation 6). With increased B diffusion on the Co<sub>2</sub>B surface, Co<sub>2</sub>B is converted into CoB (equation 8). With sufficient time allowed for B diffusion, Co<sub>2</sub>B transforms into CoB, while CoB reacting with Co in the particle centre forms Co<sub>2</sub>B again (equation 9).

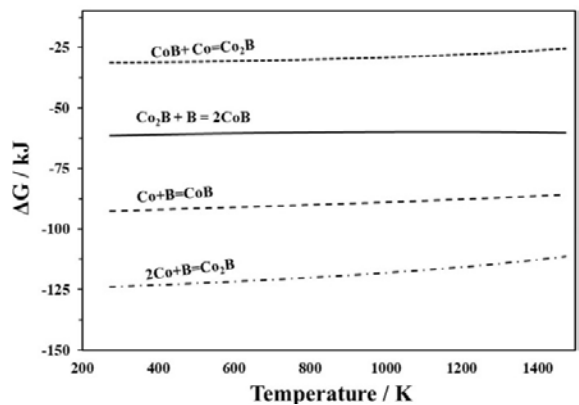


**Figure 4.** Gibbs free energies of reactions (6)–(9) change with temperature.

### Carbothermic synthesis mechanism of Co<sub>x</sub>B

From the TG/DTA analyses given in Fig. 2 and the Gibbs free energy of formation graphs of the reactions given in Fig. 3, it is seen that CoB conversion occurs at 1218 K and above. Therefore, the influence of temperature on Co<sub>x</sub>B synthesis was thermodynamically investigated at temperatures of 1273, 1373 and 1473 K above the CoB formation temperature of 1218 K.

The phase structures of the particles were synthesized at different temperatures for 150 minutes were investigated

by XRD and given in Fig. 5. According to the XRD patterns in Fig. 5, unreacted oxidized phases were found besides Co at 1273 K, while the particles synthesized at 1373 K were found to consist only of the Co phase. When the temperature was boosted to 1473 K, the conversion to  $\text{Co}_x\text{B}$  increased, and  $\text{Co}_2\text{B}$  formed the main phase structure in the particles. Temperature increase improves B diffusion. The Co and  $\text{Co}_x\text{B}$  phases produced at 1173 K on the surface were changed into CoB by raising the temperature to 1273 K, according to Calik et al. [2]. At 1473 K, almost all Co phases obtained at 1273 and 1373 K transformed into  $\text{Co}_2\text{B}$ .

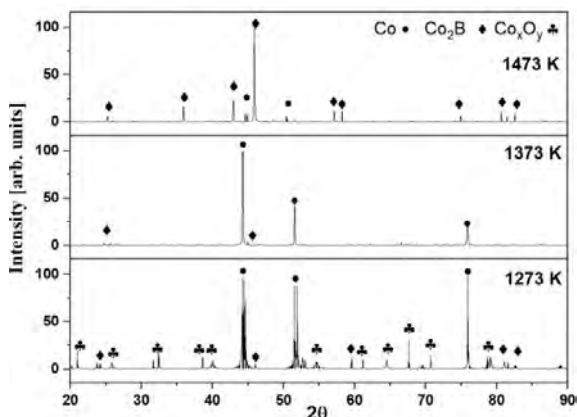


**Figure 5.** XRD patterns of Co-CoxB particles synthesized at different temperatures for 150 min.

SEM was used to investigate effects of temperature on particle morphology. Fig. 6 shows the detailed morphology of Co-CoxB powders obtained at different temperatures. From the images in Fig. 6, it is understood that the particles were formed in a vast size range, spherical morphology and due to agglomeration of fine-grained particles.

Under 1473 K, no significant  $\text{Co}_x\text{B}$  synthesis occurred, and only CoO was reduced. Therefore, the images given in Figs. 6a and 6b represent mainly Co particles. By increasing the temperature to 1473 K, 88 nm crystal size single phase

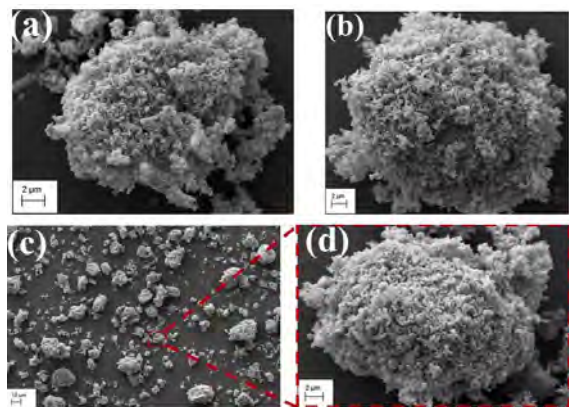


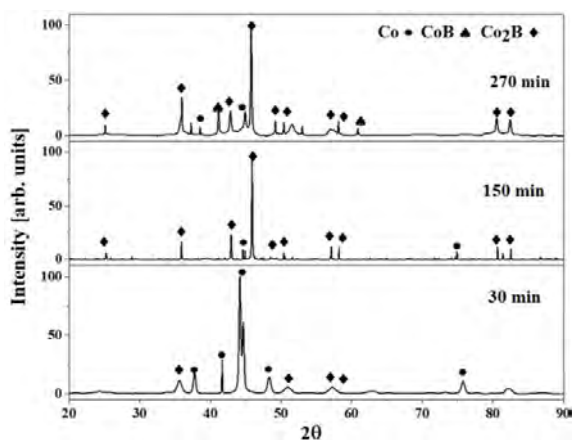
**Figure 6.** SEM images of Co-CoxB particles produced for 150 min at different temperatures: (a) 1273 K, (b) 1373 K, (c) 1473 K.

$\text{Co}_2\text{B}$  particles were synthesized. No significant change in particle morphology was observed with increasing the temperature to 1473 K.

### Effect of process duration on $\text{Co}_x\text{B}$ particles

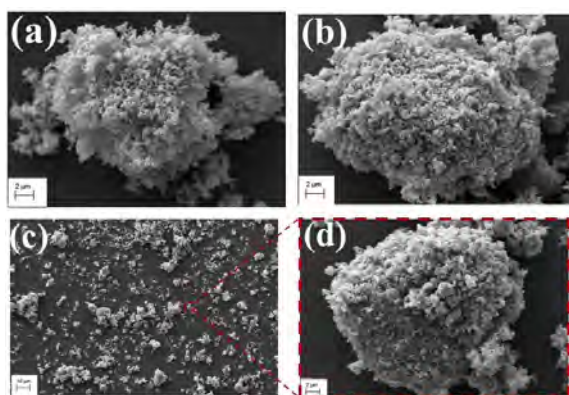
In diffusion-based thermochemical synthesis processes, reaction time and temperature are the most critical parameters. Diffusion of B increases with duration [5]. The effect of reaction time on particle structure and morphology was investigated at 30, 150 and 270 min. To ascertain the phase transition, the investigations were conducted at a constant temperature of 1473 K, where considerable CoxB phase synthesis took place. XRD patterns of particles synthesised at three different times are given in Fig. 7. The results of the XRD analysis confirmed that the particles only contained Co because B diffusion did not take place in adequate amounts in them over a short period of time (30 min). When the time was extended to 150 min to obtain single phase  $\text{Co}_x\text{B}$ , it was determined that the  $\text{Co}_2\text{B}$  phase replaced the main Co phase seen at the end of the 30 min, and the particles contained only the  $\text{Co}_2\text{B}$  phase. Then, to obtain the CoB phase by increasing B diffusion, the time was extended to 270 min. At the end of 270 min reaction time, it was observed that the particles obtained consisted of  $\text{Co}_2\text{B}$  and CoB as expected. At the end of 270 minute, the coexistence of Co,  $\text{Co}_2\text{B}$  and CoB phases in the powder supports the predicted diffusion-based synthesis and indicates that the diffusion-based synthesis takes place in the form of Co- $\text{Co}_2\text{B}$  and CoB [5, 6]. It is estimated that the possible reason for the presence of metallic cobalt, which does not form boride in the structure despite the long test times, is the removal of boron oxide compounds with low evaporation temperature from the system by evaporation.

Fig. 8 shows the morphology of the particles obtained at different times. It was shown that the particles obtained at all times directed similar formation mechanisms, and the accumulation of nanoparticles produced the second-



**Figure 7.** XRD patterns of Co- $\text{Co}_2\text{B}$  powders produced at constant 1473 K for different durations.

dary large-sized particles. It has been seen that single-phase nanocrystalline  $\text{Co}_2\text{B}$  particles with a crystal size below 100 nm can be produced carbothermally in a single step from inexpensive starting materials. It is understood that carbothermic synthesis produces lower sized particles than calciothermic produced  $\text{Co}_2\text{B}$  particles, while chemical reduction processes produce larger sized particles. Simsek et al. [15] reported that  $\text{Co}_2\text{B}$  particles with particle sizes ranging between 30-100 nm were produced by chemical reduction. Baris et al. [33] succeeded in producing nanocrystalline  $\text{Co}_2\text{B}$  particles with a crystal size of approximately 10 nm by mechanochemical method using Co,  $\text{B}_2\text{O}_3$  and Mg. Kartal [16] produced  $\text{Co}_2\text{B}$  particles calciothermally in molten salt medium starting from CoO and  $\text{B}_2\text{O}_3$  and stated that the particle sizes are very variable but above 10 microns.



**Figure 8.** SEM images of Co- $\text{Co}_2\text{B}$  powder synthesized at 1473 K for different durations: (a) 30 min, (b) 150 min, (c) 270 min.

The magnetic behaviour of  $\text{Co}_2\text{B}$  powders were investigated at ambient temperature in the range of  $\pm 20$  kOe using VSM. The magnetization curve given in Figure 9 shows that  $\text{Co}_2\text{B}$  powders show soft magnetic behaviour under a magnetic field and draw ferrimagnetism-like hysteresis. It was defined that the saturation magnetization value of the powder was  $M_s=35.361$  emu/g, the coercive magnetization value was  $H_c=16.58$  Oe, and the permanent magnetization value was  $M_r=0.501$  emu/g. It was observed that  $\text{Co}_2\text{B}$  particles produced by different methods showed similar magnetic properties. Kartal [16] reported the saturation magnetisation, coercivity and permanence values of the particles produced calciothermally starting from  $\text{B}_2\text{O}_3$  and CoO as 30.107 emu/g, 40.210 Oe, 0.764 emu/g, respectively. Baris et al. [33] found that the saturation magnetisation values of the particles produced magnesiothermally using Co and  $\text{B}_2\text{O}_3$  varied between 35 and 50 emu/g. Şimşek et al. [15] observed that the saturation magnetisation values of the particles produced by chemical reduction with the use of high purity starting materials varied between 19 and 68.5 emu/g depending on the calcination medium. Besides the production method, particle size is also effective on magnetic properties. Petit et al. [32] investigated the size-dependent magnetic properties of nanoscale  $\text{Co}_x\text{B}$  particles. The study reported that

the magnetic behaviour could shift from ferromagnetic to superparamagnetic depending on the particle size, and  $M_s$  values increase with decreasing particle size. While the  $M_s$  value of particles with a 2.5 nm size was 70 emu/g, the  $M_s$  value of particles above 10 nm was 35 emu/g, like this study.

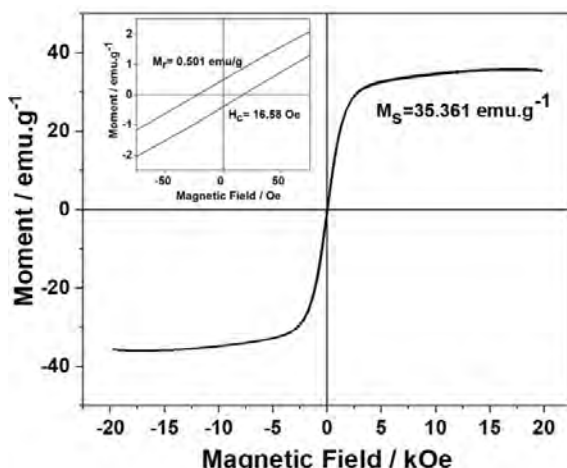


**Figure 9.** Magnetization curves of  $\text{Co}_2\text{B}$  powders produced at constant 1473 K temperature for 150 min.

## CONCLUSION

This study investigated single-phase, nanocrystalline  $\text{Co}_2\text{B}$  particles production by carbothermic reduction using low-cost, oxide-based starting materials. The effect of temperature (1273-1473 K) and time (30-270 min) on  $\text{Co}_2\text{B}$  production was investigated at constant weight ratios of  $\text{CoO}/\text{B}_2\text{O}_3/\text{C}$  (3.22/1.5/1.3). The experimental results obtained are summarised as follows;

- XRD analyses showed that the synthesis of  $\text{Co}_x\text{B}$  occurred in the form of  $\text{Co-Co}_2\text{B-CoB}$  as predicted by thermodynamic calculations.
- As a result of XRD results, it was determined that B diffusion increased with the rise in temperature and time, and the production of single  $\text{Co}_2\text{B}$  phase particles occurred at 1473 K temperature and 150 min time.
- SEM images showed that micron-sized secondary particles with irregular morphology were formed due to the agglomeration of nano-sized primary particles.
- Single-phase nanocrystalline  $\text{Co}_2\text{B}$  particles with a crystal size of 88 nm showed high agglomeration tendencies.
- Saturation magnetisation, permanent magnetisation and coercivity values of  $\text{Co}_2\text{B}$  particles were determined as 35.361 emu/g, 16.58 Oe, 0.501 emu/g, respectively.

## CONFLICT OF INTEREST

The author deny any conflict of interest.

## REFERENCES

1. Fisher KG. Cobalt Processing Developments, in: The Southern African Institute of Mining and Metallurgy. Paper presented at 6th South African Base Metals Conference, Marshalltown, 21-22 July, SAIMM, Rosebank, pp. 237–258, 2011.
2. Crundwell FK, Moats MS, Ramachandran V, Robinson TG, Davenport WG. Cobalt – Occurrence, Production, Use and Price, in: Crundwell FK, Moats MS, Ramachandran V, Robinson TG, Davenport WG (Eds.) Extractive Metallurgy of Nickel, Cobalt and Platinum Group Metals, Elsevier, Amsterdam, pp. 357–63, 2011
3. Mégret A, Vitry V, Delaunois E Study of the processing of a recycled WC–Co powder: can it compete with conventional WC–Co powders *Journal of Sustainable Metallurgy* 7 (2021) 448–458.
4. Roberts S, Gunn G. Cobalt, in: Gunn G. (Eds). Critical metals handbook, Wiley, New York, pp. 122–49, 2013.
5. Campos-Silva I, Franco-Raudales O, Meda-Campaña JA, Espino-Cortés FP, Acosta-Pavón JC. Growth kinetics of CoB-Co2B layers using the powder-pack boriding process assisted by a direct current field. *High Temperature Materials and Processes* 38 (2019) 158–67.
6. Çalik A, Karakas MS, Ucar N, Ünüvar F. Boriding kinetics of pure cobalt. *Kovove Materialy* 52 (2014) 107–12.
7. Rodríguez-Castro GA, Reséndiz-Calderon CD, Jiménez-Tinoco LF, Meneses-Amador A, Gallardo-Hernández EA, Campos-Silva IE. Micro-abrasive wear resistance of CoB/Co2B coatings formed in CoCrMo alloy. *Surface and Coatings Technology* 284 (2015) 258–63.
8. Lv J, Wang Q, Zhao J, Liu W, Chen P, Liu H. The difference in the improvement of electrochemical hydrogen storage performance between two methods of coating copper on the surface of Co2B alloy. *Chemical Physics Letters* 754 (2020) 137697.
9. Altuntaş Z, Khoshima S, Schmidt M, Bobnar M, Burkhardt U, Somer M, et al. Evolution of magnetic properties of crystalline cobalt-iron boride nanoparticles via optimization of synthesis conditions using hydrous metal chlorides. *Journal of Magnetism and Magnetic Materials* 523 (2021) 1–8.
10. Oh JH, Kim M, Lee YH, Hong SH, Park SS, Kim TH, et al. Synthesis of cobalt boride nanoparticles and h-BN nanocage encapsulation by thermal plasma. *Ceramics International* 46 (2020) 28792–9.
11. Lv J, Wang Q, Chen P, Liu H, Su Z, Zhao J, et al. Effect of ball-milling time and Pd addition on electrochemical hydrogen storage performance of Co2B alloy. *Solid State Sciences* 103 (2020) 106184.
12. Niu X, Wang X, Guan K, Wei Q, Liu H. Preparation, and electrochemical hydrogen storage application of mesoporous carbon CMK-3 coated Co2B alloy composite. *Chemical Physics Letters* 778 (2021) 138762.
13. Ghafar FA, Etherton D, Liu S, Buckley CE, English NJ, Silvester DS, et al. Tuning the catalytic activity of bifunctional cobalt boride nanoflakes for overall water splitting over a wide pH range. *Journal of The Electrochemical Society* 169 (2022) 096507.
14. Masa J, Weide P, Peeters D, Sinev I, Xia W, Sun Z, et al. Amorphous cobalt boride (Co2B) as a highly efficient nonprecious catalyst for electrochemical water splitting: oxygen and hydrogen evolution. *Advanced Energy Materials* 6 (2016) 1502313.
15. Simsek T, Barış M. Synthesis of Co2B nanostructures and their catalytic properties for hydrogen generation. *Journal of Boron* 2(1) (2017) 28–36.
16. Kartal L. Synthesis of cobalt boride particles by molten salt assisted calciothermic reduction. *Transactions of the Indian Institute of Metals* 76(3) (2022) 757–764.
17. Kartal L. Single Fe2B Phase Particle Production by Calciothermic Reduction in Molten Salt. *Hittite Journal of Science and Engineering* 9(2)(2022) 145–50.
18. Kartal L. Single step calciothermic synthesis of nickel boride particles in molten salt. *Journal of the Australian Ceramic Society* (2023) <https://doi.org/10.1007/s41779-023-00893-9>.
19. Sharifi H, Rabiei Faradonbeh S, Tayebi M. Production, and characterization of cobalt/vanadium boride nanocomposite powder by mechanochemical method. *Materials Chemistry and Physics* 202 (2017) 251–257.
20. Wu C, Bai Y, Wang X, Wu F, Zhang C. Comparisons of Co-Balloys synthesized via different methods for secondary alkaline batteries. *Solid State Ionics* 179 (2008) 924–927.
21. Doñu-Ruiz MA, López-Perrusquia N, Renteria-Salcedo A, Flores-Martinez M, Rodriguez-De Anda E, Muhl S, et al. Tribocorrosion behavior of boride coating on CoCrMo alloy produced by thermochemical process in 0.35% NaCl solution. *Surface and Coatings Technology* 425 (2021) 127698.
22. Simsek T, Barış M, Akkurt A. Co2B nanopartikülleri ile kaplanmış S235JRC karbon çelik malzemelerin farklı kesme yöntemleri ile işlenebilirlik özelliklerinin araştırılması. *Journal of Polytechnic* 22(1) (2019) 169–177.
23. Khoshima S, Altuntaş Z, Burkhardt U, Schmidt M, Prashanth KG, Somer M, et al. CoB-TiB2 crystalline powders: Synthesis, microstructural analysis and their utilization as reinforcement agent. *Advanced Powder Technology* 31 (2020) 2964–2972.
24. Altuntaş Z, Khoshima S, Somer M, Balcı Ö. The synthesis of binary and ternary cobalt-based metal borides by inorganic molten salt technique. *Journal Boron* 5(1) (2020) 12–22.
25. Yolcular S, Karaoglu S. Hydrogen generation from sodium borohydride with cobalt boride catalysts. *ALKU Fen Bilim Dergisi* 2(2) (2020) 84–96.
26. Yılmaz D, Savacı U, Koç N, Turan S. Investigation of Boro/ carbothermic and carbothermic reduction synthesized calcium hexaborides. *Journal of Boron* 3(2) (2018) 103–108.
27. Balcı, Özge AD. Borür-Karbür esaslı kompozit tozların öşütme destekli karbotermik redüksiyon yöntemi ile ekonomik yoldan üretimi. *Metallurji* 178 (2016) 40–44.
28. Verma PC, Mishra SK. Synthesis of iron boride powder by carbothermic reduction method. *Materials Today: Proceedings* 28 (2019) 902–906.
29. Yucel O, Addemir O, Tekin A. The optimization of parameters for the carbothermic production of ferrobore. Paper presented at proceedings of the 6th international ferroalloys congress, Cape Town, pp. 285–289, 1992.

30. Ross JRH. Catalyst Characterization in: Ross JRH (Eds) Contemporary Catalysis fundamentals and current applications, Elsevier, Amsterdam, pp.121–132, 2019.
31. Faria MIST, Leonardi T, Coelho GC, Nunes CA, Avillez RR. Microstructural characterization of as-cast Co-B alloys. *Materials Characterization* 58 (2007) 358–62.
32. Petit C, Pileni MP. Nanosize cobalt boride particles: Control of the size and properties. *Journal of Magnetism and Magnetic Materials* 166 (1997) 82–90.
33. Baris M, Simsek T, Akkurt A. Mechanochemical synthesis and characterization of pure Co<sub>2</sub>B nanocrystals. *Bulletin of Materials Science* 39(4) (2016) 1119–1126.





# Nanoscale Liposome Synthesis for Drug Delivery Applications via Ultrafast Acoustofluidic Micromixing

Ali Pourabdollah Vardin<sup>1,2</sup>  Gurkan Yesiloz<sup>1,2</sup> 

<sup>1</sup> Bilkent University, National Nanotechnology Research Center (UNAM), Ankara, Türkiye

<sup>2</sup> Bilkent University, Institute of Material Science and Nanotechnology, Ankara, Türkiye

## ABSTRACT

Nowadays, lipid nanoparticles have gained profound interest in chemical and biomedical engineering. The rapid development of therapeutic nanosystems has led to a need to design suitable approaches to synthesize bio-carriers for efficient drug delivery. Microfluidic methods provide an excellent opportunity to acquire desirable nanoparticle properties, including stability, size, shape, and size distribution, which are often challenging to obtain using conventional bulk synthesis methods. Rapid mixing is a crucial factor in the nanoprecipitation process as it influences the size and size distribution of the nanoparticles. Within this regard, in this work, we report an ultrafast acoustofluidic micromixer to synthesize liposome nanoparticles, which have been widely investigated in the literature as drug carriers due to their biocompatibility and biodegradability. This research has also investigated the influence of glycerol addition to the solvent to control the size of the liposomes. Our findings indicate that utilizing the acoustofluidic platform resulted in the production of nanoscale liposomes with small mean sizes compared to the hydrodynamic flow-focusing (HFF) method. Furthermore, the inclusion of glycerol led to a significant reduction in liposome size. These results emphasize the potential of the proposed approach for the efficient and precise synthesis of liposome nanoparticles with improved characteristics, which can be utilized in various biomedical and drug delivery applications.

### Keywords:

Acoustofluidics; Liposome synthesis; Acoustic micromixers; Microfluidics

## INTRODUCTION

Lipid nanoparticles (NPs) have garnered significant attention in a wide range of chemistry, medicine, and drug delivery studies due to their unique properties [1,2]. Organic nanoparticles are excessively employed as drug carriers in the literature owing to their biocompatibility, biodegradability, and stability [3]. Liposomes are a kind of organic nanoparticle that gain undeniable attention as drug carriers due to their unique characteristics. These nanoscaled spherical structures are composed of a biodegradable lipid bilayer, making them a practical and preferred candidate for delivering drugs. Also, their lipid bilayer structure can encapsulate both hydrophilic and hydrophobic drugs, which makes them versatile vehicles for drug delivery [4-9]. However, in order to leverage these features, liposome nanoparticles need to be produced in a more controlled size and polydispersity manner. The characteristics of nanoparticles, such as size, morphology, and stability, are directly affected by the approach used to synthesize them [10,11]. Conventional

bulk synthesis methods often face challenges in generating NPs with controllable size and low polydispersity index (PDI) [12]. Nevertheless, to address these limitations, microfluidic technologies offer an attractive platform for synthesizing NPs with desirable properties, including various sizes and narrower size distributions [13]. Moreover, with microfluidic platforms, multiple operations on the nanoparticles can be done on a single chip, which is not applicable in conventional methods.

Microfluidic-based nanoparticle synthesis can generally be classified into two types: droplet-based (two-phase) and mixing-based (single-phase) microfluidics. Droplet-based microfluidics enables the formation of monodisperse microparticles with larger sizes, providing an opportunity to load them with more drugs or cargo [14,15]. Mixing-based nanoparticle synthesis aims to achieve maximum solvent and solute mixing performance to facilitate homogeneous nanoparticle

### Article History:

Received: 2023/05/07

Accepted: 2023/08/08

Online: 2023/09/30

**Correspondence to:** Gürkan Yeşilöz,  
E-mail: gurkan@unam.bilkent.edu.tr,  
Phone: +90 312 290 8985;  
Fax: +90 312 266 4365

This article has been checked for similarity.



This is an open access article under the CC-BY-NC licence

<http://creativecommons.org/licenses/by-nc/4.0/>

### Cite as:

Vardin A P and Yesiloz G, "Nanoscale Liposome Synthesis for Drug Delivery Applications via Ultrafast Acoustofluidic Micromixing" Hittite Journal of Science and Engineering, 10(3): 237–241, 2023. doi:10.17350/hjse19030000312

nucleation. This method can be divided into hydrodynamic flow focusing and active micromixers to form nanoparticles. Hydrodynamic flow focusing (HFF) merely relies on diffusion for mixing to produce nanoparticles [16-19]. On the other hand, active methods employ external forces such as acoustic [20,21], electrical [22], or magnetic fields to facilitate the synthesis of nanoparticles. Active micromixers offer rapid and efficient mixing in a shorter time and length, making them an ideal and preferred option for achieving controllable nanoprecipitation and tunable size of nanoparticles (NPs).

In this study, we introduce an ultrafast acoustofluidic micromixer device that enables the production of nanoscale liposome synthesis for drug delivery applications. We utilized a piezoelectric transducer that generates bulk acoustic waves capable of penetrating deep into the material. These generated waves cause oscillatory motion of sharp edges to induce strong microstreaming within the microchannel, consequently reaching higher mixing efficiency. Additionally, the study evaluated the influence of glycerol concentration in the solvent on the liposome nanoparticle properties.

## MATERIALS AND METHODS

### Materials and Experimental Setup

Glycerol, 98% sn-3-phosphocholine from Sunflower (non-GMO) phospholipid and ethanol were used to synthesize liposome nanoparticles. Also, distilled water and fluorescein dye were utilized for mixing characterization.

The experimental setup used in this work consists of a microfluidic chip integrated with a piezoelectric transducer, a signal generator (Agilent 33220A/ Arbitrary Waveform Generator), a syringe pump (New Era Syringe Pump NE-4000), an amplifier and an inverted microscope (Zeiss, Axio Observer 7) mounted with a CCD camera. The syringe pump allows the injection of fluids at a specific flow rate into the channel. The signal generator produces a square wave signal at the resonance frequency, and this signal's voltage can be increased up to 95 V by the power amplifier. Later, this signal was fed to the piezoelectric transducer, which delivers the acoustic streaming to the microfluidic chip. Moreover, the flow pattern was captured by the inverted microscope and the mounted CCD camera.

### Device Fabrication

The standard soft-lithography method was employed to produce microchannels composed of polydimethylsiloxane (PDMS) material with sharp-edge patterns on their sidewalls. The PDMS base was mixed with a curing agent in a ratio of 10:1 and subsequently poured onto the SU-8/silicon master, which was fabricated in the fashion developed in our previous work [23]. The resulting mold was

then cured for a day at room temperature, peeled off from the master, and bonded to a glass substrate using plasma treatment. The channel has a width of 600  $\mu\text{m}$  and a depth of 50  $\mu\text{m}$ , and the sharp edges of the channels have a tip angle of 15°, a length of 225  $\mu\text{m}$ , and a width of 60  $\mu\text{m}$ .

### Mechanism of Acoustofluidic Micromixing Platform

As shown in the schematic in Fig. 1, both the PDMS and the piezoelectric transducers are bonded to the glass substrate.

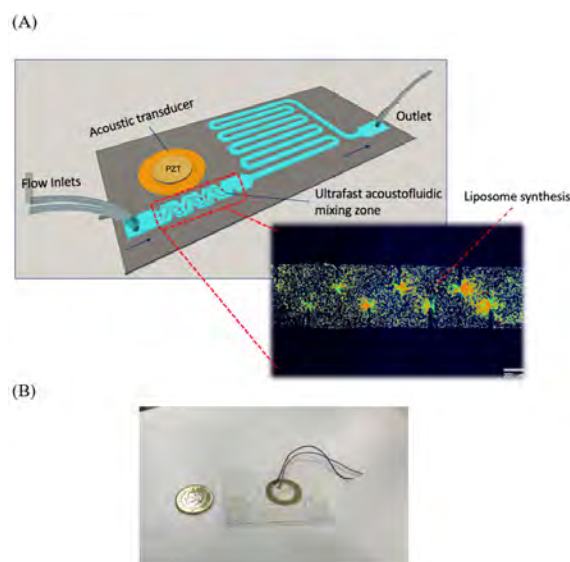


**Figure 1.** A) Schematic of description of the acoustofluidic micromixer, microstreaming, and the liposome production in the microfluidic platform. B) An image of the acoustofluidic micromixer device.

When the driving voltage is applied to the piezoelectric transducer, the vibration of its membrane is transferred to the PDMS chip, causing the sharp-edge patterns to oscillate. This oscillation generates powerful vortices in the microchannel located near the sharp edges, thereby facilitating the mixing of the two parallel flow streams. The resulting acoustic streaming can enable faster and more efficient mixing, improving liposome nanoparticle synthesis. Overall, the acoustofluidic platform offers a promising tool for enhancing the efficiency and reproducibility of liposome synthesis processes.

### Liposome Synthesis and Characterization

To synthesize nanoscale liposomes, a solution of 70% ethanol containing 98% sn-3-phosphocholine was introduced through one inlet of the microfluidic channel, while a mixture of distilled water and glycerol at three different concentrations of 15%, 30%, and 45% were introduced through the other inlet. The injection process was carried out using a syringe pump, and the flow rate ratio of the two inlets was maintained at 1:1. Average diameter

and size distributions of the liposomes were analyzed by a dynamic light scattering (DLS) device (Zetasizer Nano ZS). All the collected samples were loaded into the cuvette and put into the DLS instrument for measurement.

## RESULTS AND DISCUSSION

### Mixing Characterization

To trace the mixing performance, two fluids with distinct colors were used; diluted fluorescein dye and distilled water. The flow streams were monitored by an inverted microscope. To capture the fluorescence images, we utilized the FITC channel of the microscope with an exposure time of 100 ms. By monitoring the channel with the inverted microscope, visually, it is possible to capture incomplete or complete mixing. However, mixing efficiency has to be obtained numerically to get precise results. Mixing indexes were calculated across the width of the channel based on the following equation [24]:

$$\text{Mixing Index (MI)} = 1 - \frac{\sqrt{\frac{1}{n} \sum (I_i - I_{avg})^2}}{I_{avg}}$$

where  $I_i$ ,  $I_{avg}$ , and  $n$  are the light intensity value of each point, the average intensity value, and the total number of pixels, respectively. A MI of 0 and 1 indicate unmixed and completely mixed scenarios, respectively.

### Effect of the Frequency on Mixing Index

The frequency of a signal is a critical parameter that profoundly impacts the intensity of acoustic streaming. It is essential to determine the resonance frequency of the piezoelectric transducer to achieve optimal efficiency. While every piezoelectric transducer has a unique resonance frequency specified by the manufacturer within a range, it should be determined precisely through visual and quantitative observation during the experiment to locate its exact value to gain better performance. To ob-

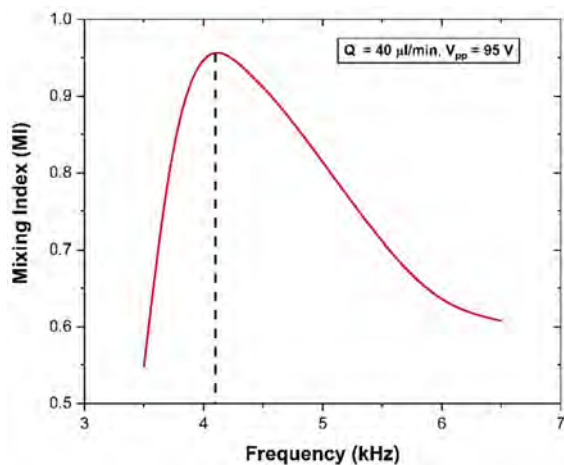


Figure 2. Mixing index at different operating frequencies.

tain an accurate resonance frequency, the frequency varied within the range of 3.5-6.5 kHz, with increments of 100 Hz. The captured images were used to calculate the mixing index at the outlet for different frequencies while maintaining a constant total flow rate of 40  $\mu\text{l}/\text{min}$  and voltage of 95V. The results revealed that the resonance frequency of the piezoelectric transducer was 4.3 kHz, as depicted in Fig. 2.

### Effect of the Flow Rate and Voltage on the Mixing Index

To explore the impact of flow rate and input voltage on the mixing performance, the frequency was set at 4.3 kHz. The channel was observed under different voltages and flow rates using the inverted microscope, and the resulting images were analyzed to quantify the mixing index. Fig. 3 displays the results, which indicate that at low voltage values (up to 20V) and high flow rates, the acoustic streaming was not sufficiently strong to disrupt the background flow and induce chaotic flow, resulting in incomplete mixing.

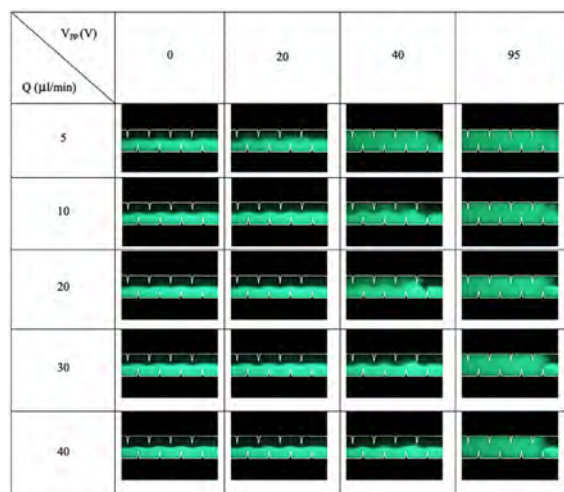


Figure 3. Comparison of mixing performance for different voltages and flow rates.

However, step-wise increasing voltage to higher values, complete mixing was achieved even at high flow rates. Fig. 4 demonstrates that complete mixing occurs for all flow rates when the input voltage is set at 95V. Moreover, it is important to note that since the mixing index varies along the channel, three distinct cross-sectional areas were chosen for the calculation of the mixing index.

### Liposome Characterization

The diameter and size distribution of liposome nanoparticles are critical factors for their therapeutic application [25], and these parameters can be controlled by regulating the mixing time during the nanoprecipitation process in microfluidic systems. The proposed acoustof-

fluidic system provides direct control over the size of liposomes by adjusting the total flow rate, input voltage, and glycerol percentage in the solvent. Three distinct glycerol concentrations of 15%, 30%, and 45% were utilized.

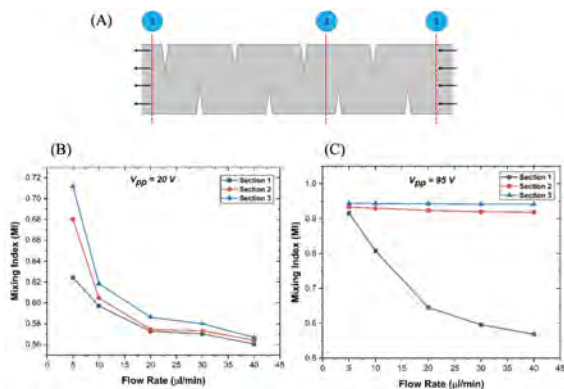


**Figure 4.** Comparison of mixing performance for different voltages and flow rates.

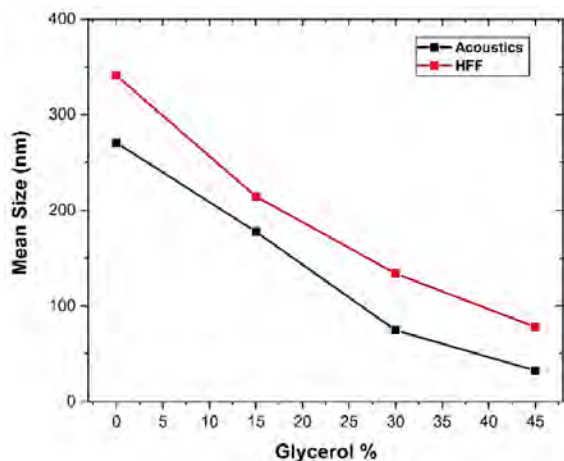


**Figure 5.** Effect of acoustic micromixer and glycerol percentage on the mean size.

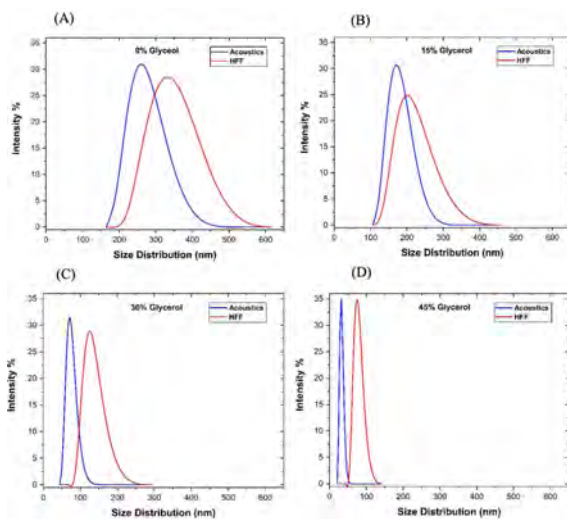


**Figure 6.** Effect of acoustic micromixer and glycerol percentage on the size distribution (A to D demonstrating the effect of glycerol from 0% to 45%).

To evaluate the size-tuning ability of the acoustofluidic platform, the average diameter of the liposomes was measured using a dynamic light scattering device (DLS) at a total flow rate of 40 µl/min and an input voltage of 95 V for different concentrations of glycerol, with Acoustic and HFF methods. To achieve high throughput, a total flow rate of 40 µl/min was selected as the optimal choice for the synthesis of liposome nanoparticles. As shown in Fig. 5, the mean average size of the liposomes decreased with the implementation of acoustic pressure compared to the HFF method (i.e., in the acoustic-off case). It is worth noting that adding glycerol to the solvent reduced the average size of the liposome nanoparticles, and a greater reduction in the liposome's average diameter was observed with increasing glycerol concentration.

Furthermore, the size distribution of liposomal nanoparticles was analyzed using Dynamic Light Scattering (DLS), as demonstrated in Fig. 6. It can be inferred that the utilization of the acoustic micromixer results in the production of nanoparticles with a lower polydispersity index in comparison to the scenario without acoustic mixing, which indicates its advantageous potential for drug delivery applications.

## CONCLUSION

In this study, we report a practical acoustofluidic platform that achieves ultrafast and efficient mixing performance, enabling us to synthesize nanoscale liposome nanoparticles with a high degree of control over particle size compared to the hydrodynamic flow focusing and conventional methods. This acoustofluidic platform leverages sharp-edge patterns that oscillate and vibrate when subjected to acoustic pressure generated by the piezoelectric transducer. This vibration creates strong and powerful vortices in the flow stream, which effectively disturb the fluids, leading to complete mixing in merely a few milliseconds. At the resonant frequency of 4.3 kHz and a voltage of 95 volts, acoustic microstreaming exhibited a remarkable ability to achieve complete mixing of fluids with a total flow rate of 40 µl/min, which is a notably higher flow rate compared to the literature. The results indicate that the implementation of an acoustic micromixer in liposome synthesis resulted in the production of highly uniform nanoparticles with reduced size when compared to the acoustic-off condition. Moreover, the impact of adding glycerol to the solvent was explored, revealing a significant reduction in liposome size upon its inclusion, producing monodispersed liposomes with an average diameter down to 30 nm.

## ACKNOWLEDGEMENT

Dr. Gurkan Yesiloz gratefully acknowledges the support from the Scientific and Technological Research Council of Türkiye (TUBITAK) (2232-Grant No: 118C263) and (1001-Grant No: 221M575). However, the entire responsibility of the publication/article belongs to the owner of the publication/article. The financial support received from TUBITAK does not mean that the content of the publication is approved in a scientific sense by TUBITAK.

## CONFLICT OF INTEREST

Authors approve that to the best of their knowledge, there is not any conflict of interest or common interest with an institution/organization or a person that may affect the review process of the paper.

## AUTHOR CONTRIBUTION

**Ali Pourabdollah Vardin** performed the experiments and analyzed the results.

**Gurkan Yesiloz** conceived the idea, fabricated the chip, supervised the experimental progress, analyzed the structure of the work and the results. Both authors drafted and wrote the manuscript.

---

## REFERENCES


---

1. Kohane DS. Microparticles and nanoparticles for drug delivery. *Biotechnology and Bioengineering*. 96(2) (2007):203-9.
2. Torchilin, Vladimir P. Nanoparticulates as drug carriers. Imperial college press, (2006).
3. Mitragotri, Samir and Patrick Stayton. Organic nanoparticles for drug delivery and imaging. *Mrs Bulletin* 39.3 (2014): 219-223.
4. Immordino, Maria Laura, Franco Dosio, and Luigi Cattel. Stealth liposomes: review of the basic science, rationale, and clinical applications, existing and potential. *International journal of nanomedicine*. 1.3 (2006): 297.
5. Çağdaş, Melis, Ali Demir Sezer and Seyda Bucak. Liposomes as potential drug carrier systems for drug delivery. *Application of nanotechnology in drug delivery 1* (2014): 1-50.
6. Brandl, M. Liposomes as drug carriers: a technological approach. *Biotechnol Annu Rev* (2001): 59-85.
7. Mallick, Sudipta, and Joon Sig Choi. Liposomes: versatile and biocompatible nanovesicles for efficient biomolecules delivery. *Journal of nanoscience and nanotechnology* 14.1 (2014): 755-765.
8. Laouini, Abdallah, et al. Preparation, characterization and applications of liposomes: state of the art. *Journal of colloid Science and Biotechnology* 1.2 (2012): 147-168.
9. Akbarzadeh, Abolfazl, et al. Liposome: classification, preparation, and applications. *Nanoscale research letters* 8.1 (2013): 1-9.
10. Tian, Fei, et al. Microfluidic technologies for nanoparticle formation. *Lab on a Chip* (2022) 22, 512-529.
11. Valencia, Pedro M., et al. Microfluidic technologies for accelerating the clinical translation of nanoparticles. *Nature nanotechnology* 7.10 (2012): 623-629.
12. Ma, Junping, et al. Controllable synthesis of functional nanoparticles by microfluidic platforms for biomedical applications—a review. *Lab on a Chip* 17.2 (2017): 209-226.
13. Zhang, Guo, and Jiaming Sun. Lipid in chips: a brief review of liposomes formation by microfluidics. *International Journal of Nanomedicine* 16 (2021): 7391.
14. Tan, Yung-Chieh, et al. Controlled microfluidic encapsulation of cells, proteins, and microbeads in lipid vesicles. *Journal of the American Chemical Society* 128.17 (2006): 5656-5658.
15. Yu, Bo, Robert J. Lee, and L. James Lee. Microfluidic methods for production of liposomes. *Methods in enzymology* 465 (2009): 129-141.
16. Michelon, Mariano, et al. High-throughput continuous production of liposomes using hydrodynamic flow-focusing microfluidic devices. *Colloids and Surfaces B: Biointerfaces* 156 (2017): 349-357.
17. Hood, Renee R. and Don L. DeVoe. High-Throughput Continuous Flow Production of Nanoscale Liposomes by Microfluidic Vertical Flow Focusing. *Small* 11.43 (2015): 5790-5799.
18. Han, Jung Yeon, Joseph N. La Fiandra and Don L. DeVoe. Microfluidic vortex focusing for high throughput synthesis of size-tunable liposomes. *Nature Communications* 13.1 (2022): 6997.
19. Shan, Han, et al. One-Step Formation of Targeted Liposomes in a Versatile Microfluidic Mixing Device. *Small* 19.7 (2023): 2205498.
20. Rasouli, M. Reza, and Maryam Tabrizian. An ultra-rapid acoustic micromixer for synthesis of organic nanoparticles. *Lab on a Chip* 19.19 (2019): 3316-3325.
21. Zhao, Shuaiguo, et al. Fabrication of tunable, high-molecular-weight polymeric nanoparticles via ultrafast acoustofluidic micromixing. *Lab on a Chip* 21.12 (2021): 2453-2463.
22. Modarres, Paresa, and Maryam Tabrizian. Electrohydrodynamic-driven micromixing for the synthesis of highly monodisperse nanoscale liposomes. *ACS Applied Nano Materials* 3.5 (2020): 4000-4013.
23. Yesiloz, Gurkan, Muhammed Said Boybay and Carolyn L. Ren. Label-free high-throughput detection and content sensing of individual droplets in microfluidic systems. *Lab on a Chip* 15.20 (2015): 4008-4019.
24. Yesiloz, Gurkan, Muhammed S. Boybay and Carolyn L. Ren. Effective thermo-capillary mixing in droplet microfluidics integrated with a microwave heater. *Analytical chemistry* 89.3 (2017): 1978-1984.
25. Danaei, M., et al. Impact of particle size and polydispersity index on the clinical applications of lipidic nanocarrier systems. *Pharmaceutics* 10.2 (2018): 57.



# Energy, Exergy, and Environment Performance Evaluation of Cascade Refrigeration System with Natural Refrigerants

Meltem Koşan 

 Kahramanmaraş İstiklal University, Department of Energy systems Engineering, Kahramanmaraş, Türkiye

## ABSTRACT

Cascade refrigeration systems are preferred in applications where low temperature cooling is required, such as in some special industrial and laboratory applications. Since, in these systems, the energy consumed by the compressors is less and the compressor outlet temperature is lower. Due to environmental problems, the use of natural refrigerants in cascade refrigeration systems has become to be of great importance. In this study, two cascade systems consisting of R744/R290 (System 1) and R1270/R290 (System 2) natural refrigerant pairs were designed and thermodynamically examined. In the analyzes performed according to different evaporator temperatures, the highest coefficient of performance (COP) value was 3.66 at  $-20^{\circ}\text{C}$  evaporating temperature was obtained in the cascade system consisting of the R1270/R290 refrigerant pair. Moreover, it was considered that there was a 17.95% enhancement in exergy efficiency with the use of R1270 refrigerant in the low temperature cycle. By the rise in the evaporator temperature, energy consumption decreases and as a result, the amount of carbon dioxide emissions reduced was attained.

### Keywords:

Cascade refrigeration system; R744; R1270; R290; COP

## INTRODUCTION

The effective use of the energy and the improvement of systems becomes an important issue because the world's energy resources are limited and gradually decreasing. Nowadays, approximately 17% of the total electricity used in the world is consumed in refrigeration cycles (1,2). In order to use energy efficiently, studies such as reducing energy consumption values, increasing the performance of the system, and selecting the appropriate refrigerant are carried out. On the other hand, when considering system improvements, it should be adapted to human health and the surrounding, and the ozone layer depletion (ODP) and global warming potential (GWP) values of the refrigerants used should be low (3-5).

Low temperature refrigeration processes are widely preferred in various fields, including industrial, medical applications, and scientific research. Cascade refrigeration systems are generally used in low temperature applications because of their better performance and lower operating costs. Luiz et al. (6) evaluated the thermodynamic performance of the refrigerant pairs R744/R1270, R744/R717, and R744/RE170 in the cascade refrigeration system consisting of two vapor compression systems.

14% enhancement in the coefficient of performance (COP) over values obtained with natural refrigerants, the R744/RE170 mixture indicated the best results with a COP of 2.34 and increased exergetic efficiency by up to 30%. In another similar study, Kasi and Cheralathan (7) numerically investigated a cascade refrigeration system in which R170 refrigerant was employed as the low temperature cycle and R32, R515B, and R466A refrigerants were used as the high temperature cycle. R515B/R170 refrigerant pair was shown to offer the best performance than the other refrigerant pairs. As a result, the COP enhanced from 3.626 to 3.781, and the compressor work reduced from 2.757 to 2.645 kJ/s when the evaporation temperature rised from raised 45 K. Mofrad et al. (8) researched the thermodynamic simulation and analysis of the heat recovery cascade refrigeration systems. Energy and exergy analyses of the cascade system using R744 and R744A refrigerants were carried out. It was concluded that it increased COP by 7.6% and exergy efficiency by 12.5% with the heat recovery cascade cooling system.

Soni et al. (9) performed the thermodynamic analysis of the cascade refrigeration system consisting of R134a/R744, R1234yf/R744 and R1234ze/R744 ref-

### Article History:

Received: 2023/05/25

Accepted: 2023/08/29

Online: 2023/09/30

Correspondence to: Meltem Koşan,

E-Mail: meltem.kosan@istiklal.edu.tr

Phone: +90 552 202 4940

This article has been checked for similarity.



This is an open access article under the CC-BY-NC licence

<http://creativecommons.org/licenses/by-nc/4.0/>

### Cite as:

Koşan M, "Energy, Exergy, and Environment Performance Evaluation of Cascade Refrigeration System with Natural Refrigerants". *Hittite J Sci Eng.* 2023;10 (3): 243-248. doi:10.17350/hjse19030000313



rigerants with low global warming potential by creating a mathematical model. The R1234yf/R744 refrigerant pair was found to be the most efficient, with a system efficiency of 58%. Ozyurt et al. (10) carried out a theoretical analysis of a cascade refrigeration cycle using R717 and R744 refrigerants. It was deduced that there was a decrease in exergy destruction by increasing the condenser temperature in the carbon dioxide cycle at  $-25\text{ }^{\circ}\text{C}$  evaporation and  $-10\text{ }^{\circ}\text{C}$  condenser temperature, and accordingly, the COP value and the second law efficiency increased. Sun et al. (11) presented a comparative analysis of the thermodynamic performance of R41/R404A and R23/R404A cascade refrigeration systems. The results showed that the input power of the R41/R404A refrigeration system was lower than the R23/R404A system, and the COP was higher than the R23/R404A system. The exergy efficiency of the R41/R404A and R23/R404A systems was obtained as 44.38% and 42.98%, in the same order. According to the theoretical analysis result, it was seen that the R41/R404A system was a more potential refrigerant couple than R23/R404A. Silva et al. (12) suggested a cascade refrigeration system with R744-R404A refrigerant instead of refrigeration systems with R404A and R22 refrigerants for supermarket applications. As a result of the evaluation, when the cascade refrigeration cycle using R744 was compared with the other two systems, it was indicated that the electrical energy consumption was reduced by 24-13%, and the life of the R744 compressor was extended with the low compression ratio.

Huang et al. (13) recommended mechanical subcooling and cascade recooling cycles, which they used as R744 sub-cycles. It was found that R744 was suitable for these systems and the compressor work was reduced by 28.5%. Chi et al. (14) developed the mathematical model of the R717/R744 ejector subcooled cascade system and performed its thermodynamic analysis. Compared to the conventional cascade system of in this system, 5.4% and 4.8% higher COP and exergy efficiencies were obtained. Yan et al. (15) carried out simulations of the R290/R600A cascade system for domestic freezers. It was observed that the cooling capacity increased by 10.2-17.1% with this refrigeration pair. Cabello et al. (16) compared the performance of R290, R1270, R600A and R1234ze(E) alternatives instead of R134A in the R134A/R744 cascade system. The best results were achieved in the cooling capacity of the R290 and R1270 refrigerants. Zhu et al. (17) studied the low and high temperature circuits in the R744/R717 cascade system and the multi-target temperature cascade system in which the R1270 refrigerant was used. With the multi-target temperature cascade system, 25% and 10% improvement in COP and 19% and 5% rise in exergy efficiency were obtained according to low and high temperature cycling, respectively.

Recently, the use of natural refrigerants, which are found in nature and do not have harmful effects on the envi-

ronment, has become widespread instead of synthetic refrigerants. Considering the literature survey, the use of natural refrigerants in cascade refrigerant systems provides great advantages. In this study, two different cascade systems are proposed using three different natural refrigerants. The performance of these two systems under the same conditions was compared. Energy, exergy and environmental analyzes were carried out. The novelty of this study is the use of R744/R290 and R1270/R290 refrigerant pairs, which have very low GWP values, in the cascade system.

## SYSTEM DESCRIPTION

The cascade refrigeration system including two basic vapor compression refrigeration cycles, one the low temperature cycle (LTC) and the other the high temperature cycle (HTC). The LTC cycle and HTC cycle are connected to each other via a cascade condenser. Fig. 1 depicts the schematic representation of the typical cascade refrigeration system. On the other hand, the P-h diagram of the cascade cooling system is demonstrated in Fig. 2.

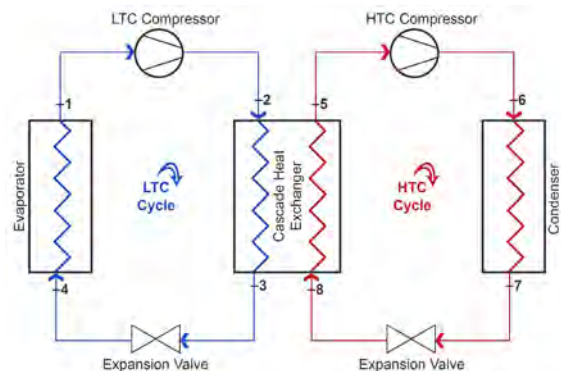


Figure 1. Schematic illustration of cascade cooling system

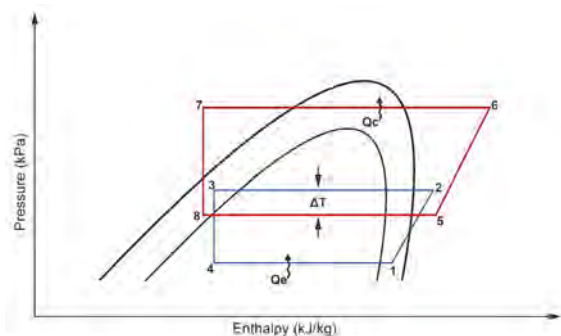


Figure 2. P-h diagram of the cascade cooling system

In this study, two different cascade refrigeration systems using three different natural refrigerants were investigated thermodynamically. Refrigerants R744 and R1270 were chosen for LTC cycles whereas R290 was chosen for the HTC cycle. Moreover, the R744/R290 refrigerant pair was called System 1, and the R1270/R290 refrigerant pair was as System 2. Table 1 demonstrates the properties of the commonly used natural refrigerant.

**Table 1.** The properties of some natural refrigerants (18)

Refrigerants	Chemical Formula	Flammability Classification	Global Warming Potential (GWP)	Ozone Depletion Potential (ODP)	Critical Temperature (°C)	Critical Pressure (MPa)	Normal Boiling Temperature (°C)
R744	CO <sub>2</sub>	A1	1	0	30.98	7.38	-78.46
R290	C <sub>3</sub> H <sub>8</sub>	A3	3	0	96.74	4.25	-42.11
R1270	C <sub>3</sub> H <sub>6</sub>	A3	1.8	0	92.42	4.55	-47.62
R600a	C <sub>4</sub> H <sub>10</sub>	A3	4	0	134.66	3.83	-11.75
R717	NH <sub>3</sub>	B2L	0	0	132.25	11.33	-33.33
R170	C <sub>2</sub> H <sub>6</sub>	A3	6	0	32.12	48.72	-88.7

The necessary assumptions are given in Table 2 to determine the performance parameters of the system. The following reasonable assumptions were made in the energy, exergy and environmental analyzes of the cascade cooling system:

- Pressure and heat losses and gains in the system were neglected.
- It was assumed that all components in the system were in a steady state.
- Compressors, expansion valves, and phase changes in a cascade condenser were adiabatic.
- Evaporation and condensation processes were isobaric.

**Table 2.** Assumptions required for analyses

Parameters	Value
Cooling Capacity	15 kW
Evaporator Temperature, $T_{evap}$	-20°C, -25°C, and -30°C
Condenser Temperature, $T_{con}$	45°C
Ambient Temperature, $T_o$	25°C
Mechanical efficiency of compressors, $\eta_{mec}$	90%
Electrical efficiency of compressors, $\eta_{el}$	93%
Superheating (in LTC and in HTC)	5°C
Refrigerants	R744, R1270, R290

## THEORETICAL ANALYSIS

The basic vapor compression refrigeration cycles consist of compressor, condenser, expansion valve and evaporator. The required heat is provided by the HTC condenser of the cascade system including HTC and LTC cascade cycles. The heat supplied by the condenser is expressed in the following equation (19):

$$\dot{Q}_{con} = \dot{m}_{r,HTC} (h_{con,i} - h_{con,o}) \quad (1)$$

The evaporator capacity of the cascade system is given as follows:

$$\dot{Q}_{evap} = \dot{m}_{r,LTC} (h_{evap,o} - h_{evap,i}) \quad (2)$$

The energy equation for the cascade condenser (heat exchanger of cascade system) can be defined as (20):

$$\dot{m}_{r,LTC} (h_{hx(LTC),i} - h_{hx(LTC),o}) = \dot{m}_{r,HTC} (h_{hx(HTC),o} - h_{hx(HTC),i}) \quad (3)$$

The compressors power of LTC and HTC refrigeration cycles can be given as:

$$\dot{W}_{comp,LTC} = \dot{m}_{r,LTC} (h_{comp(LTC),o} - h_{comp(LTC),i}) / \eta_{is} \eta_{mec} \eta_{el} \quad (4)$$

$$\dot{W}_{comp,HTC} = \dot{m}_{r,HTC} (h_{comp(HTC),o} - h_{comp(HTC),i}) / \eta_{is} \eta_{mec} \eta_{el} \quad (5)$$

The isentropic efficiency of the compressors is (21):

$$\eta_{is} = 1 - (0.04 x PR) \quad (6)$$

Total compressor power requirement:

$$\dot{W}_{comp,total} = \dot{W}_{comp,LTC} + \dot{W}_{comp,HTC} \quad (7)$$

The COP value of the cascade refrigeration system can be found as follows:

$$COP_{system} = \frac{\dot{Q}_{evap}}{\dot{W}_{comp,total}} \quad (8)$$

While calculating the exergy efficiency of the cascade refrigeration system, the exergy destruction equations of the cooling components are used. These equations are given below (22):

$$\dot{E}x_{d,evap} = \left( \dot{E}x_{evap,o} - \dot{E}x_{evap,i} \right) + \dot{Q}_{evap} \left( 1 - \frac{T_o}{T_{evap}} \right) \quad (9)$$

$$\dot{E}x_{d,con} = \left( \dot{E}x_{con,i} - \dot{E}x_{con,o} \right) + \dot{Q}_{con} \left( 1 - \frac{T_o}{T_{con}} \right) \quad (10)$$

$$\dot{E}x_{d,hx} = \left( \dot{E}x_{hx(LTC),i} - \dot{E}x_{hx(LTC),o} \right) + \left( \dot{E}x_{hx(HTC),i} - \dot{E}x_{hx(HTC),o} \right) \quad (11)$$

$$\dot{E}x_{d,comp(LTC)} = \dot{E}x_{comp(LTC),o} - \dot{E}x_{comp(LTC),i} \quad (12)$$

$$\dot{E}x_{d,comp(HTC)} = \dot{E}x_{comp(HTC),o} - \dot{E}x_{comp(HTC),i} \quad (13)$$

$$\dot{E}x_{d,ex(LTC)} = \dot{E}x_{ex(LTC),i} - \dot{E}x_{ex(LTC),o} \quad (14)$$

$$\dot{E}x_{d,ex(HTC)} = \dot{E}x_{ex(HTC),i} - \dot{E}x_{ex(HTC),o} \quad (15)$$

$$\eta_{\dot{W}} = \frac{\dot{E}x_{evap,o} - \dot{E}x_{evap,i}}{\dot{W}_{comp,total}} \quad (16)$$

Another exergy performance criterion is the exergetic performance coefficient (EPC). EPC is the ratio of exergy output to total exergy destruction. The EPC of this proposed cascade refrigeration system can be defined as follows (23, 24):

$$EPC = \frac{\dot{Q}_{evap} (1 - T_0 / T_{evap})}{\dot{E}x_{d,total}} \quad (17)$$

The calculation of CO<sub>2</sub> emissions for the cascade refrigeration system based on the power consumption of the compressor is given in the equation below:

$$\Phi_{CO_2} = \Psi_{CO_2} \times \dot{W}_{comp,total} \quad (18)$$

where  $\Phi_{CO_2}$  is the amount of CO<sub>2</sub> (kg CO<sub>2</sub>/h) reduced per hour and  $\Psi_{CO_2}$  denotes the average amount of CO<sub>2</sub> emissions (2.08 kg CO<sub>2</sub>/kWh) obtained during power generation from coal (25). For example, if the energy consumption of the total compressors in a cascade system is 5 kW, the amount of CO<sub>2</sub> is 10.4 kg, and the annual CO<sub>2</sub> emission is 3.79 tons.

## RESULTS AND DISCUSSION

In this study, R744 was chosen as the refrigerant in the LTC cycle in the System 1 cascade system, and R1270 as the refrigerant in the LTC cycle in the System 2 cascade system. In both systems, R290 was used as a refrigerant in the HTC cycle. Total energy consumption graph according to -20°C, -25°C, and -30°C evaporator temperatures for System 1 and System 2 is given in Fig. 3. When R744 was used in the LTC cycle, it was observed that the total energy consumption was 5.93 kW, which was the highest at -30°C evaporator temperature. However, when R1270 was used in the LTC

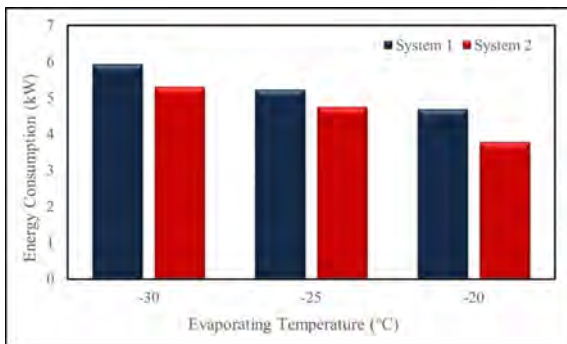


**Figure 3.** The energy consumption values according to evaporator temperatures

cycle in System 2, it was deduced that it had the lowest total energy consumption. As the evaporator temperature decreases, the compressor work increases even more. Therefore, the energy consumption of both systems had increased proportionally.

The performance of a refrigeration cycle is determined by the COP given in Eq. (8). COP values calculated for System 1 and System 2 are demonstrated in Fig. 4. COP values in System 1 and System 2 were obtained as 2.53, 2.86, 3.19 and 2.83, 3.16, 3.66 at -20°C, -25°C, and -30°C evaporator temperatures, respectively. As COP is the evaporator capacity provided in response to the work done by the compressor, it appears to be inversely proportional to energy consumption. In other words, the increase in the evaporator temperature causes a decrease in the compressor power in both systems, thus increasing the performance. It was observed that System 2 was 12.84% more efficient than System 1 at -20°C evaporator temperature.

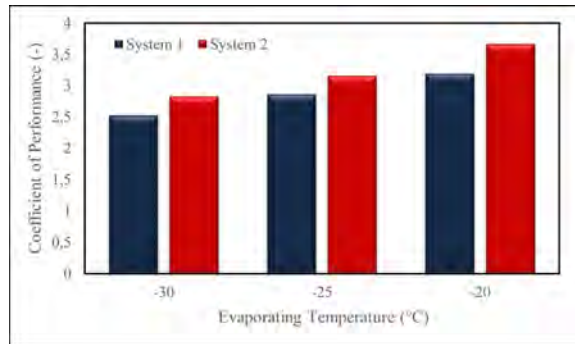


**Figure 4.** The COP values according to evaporator temperatures

The maximum useful energy value in refrigeration systems is defined by the exergy efficiency, which is the second law, and is calculated as given in Eq. (16). The exergy efficiency values of the System 1 and System 2 cascade refrigeration systems for the same operating conditions are given in Fig. 5. The exergy efficiency values for System 1 and System 2 were determined as 15.5%, 17.6%, 20.1%, and 21.2%, 22.6%, 24.5% respectively, according to -30°C, -25°C, -20°C evaporator temperatures. According to every 5°C evaporator

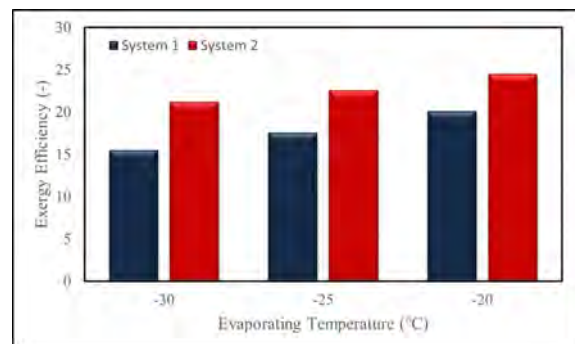


**Figure 5.** The exergy efficiency values according to evaporator temperatures

temperature rise, exergy efficiency increased by 11.93% and 12.44% for System 1 and 6.19%, 7.75% for System 2, in the same order.

The EPC values of System 1 and System 2 are given in Fig. 6. In both systems, it was observed that EPC values decreased as the evaporating temperature reduced. EPC values in System 2 were higher than in System 1 at all evaporating temperatures. The highest EPC value was obtained in System 2 at 0.28 to  $-30^{\circ}\text{C}$  evaporating temperature. On the other hand, the lowest EPC value was found as 0.20 in System 1 at an evaporating temperature of  $-20^{\circ}\text{C}$ .

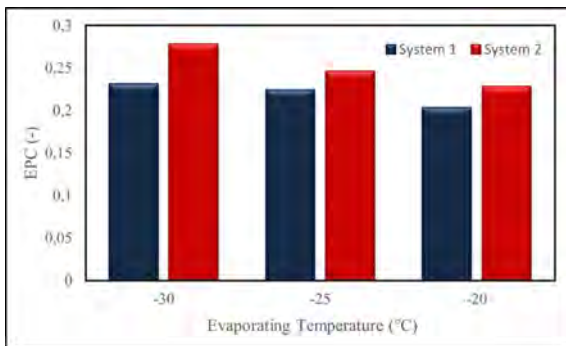


Figure 6. The EPC values according to evaporator temperatures

The annual total amount of  $\text{CO}_2$  released according to three different evaporator temperatures for System 1 and System 2 is shown in Fig. 7. It was considered that coal fuel was used in electricity generation. The amount of  $\text{CO}_2$  released by the burned coal fuel against the amount of energy consumed (kWh) was calculated separately for both systems. Accordingly, the annual total maximum  $\text{CO}_2$  amount was calculated as 4.5 and 4.03 tons $\text{CO}_2$ /year for System 1 and System 2 at  $-30^{\circ}\text{C}$  evaporator temperature. On the other hand, the lowest total annual  $\text{CO}_2$  amount was obtained as 2.82 tons $\text{CO}_2$ /year at  $-20^{\circ}\text{C}$  evaporator temperature in System 2.

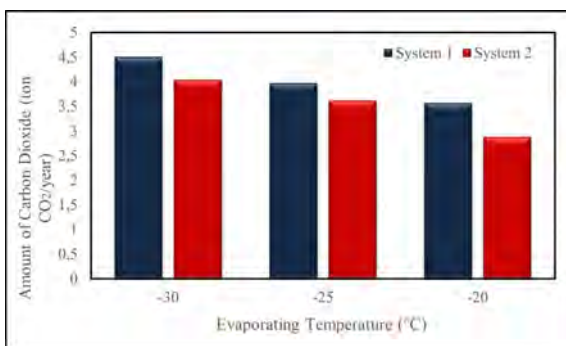


Figure 7. The amounts of  $\text{CO}_2$  released according to evaporator temperatures

## CONCLUSION

In this study, energy, exergy, and environmental analyzes of the cascade refrigeration system containing diffe-

rent refrigerants were made and the results were discussed. Moreover, natural refrigerants were used instead of synthetic refrigerants that cause global warming and ozone layer depletion in the cascade refrigeration system. R744 and R1270 natural refrigerants were selected in the LTC and R290 in HTC. The results obtained as a result of the thermodynamic analysis for two different systems designed using different refrigerants can be summarized:

- It was attained that the energy consumption of System 1 was 9.2% higher than System 2.
- In System 2, the best COP with 3.66 and the best exergy efficiency with 24.5% were determined at  $-20^{\circ}\text{C}$  evaporator temperature.
- The highest EPC value of 0.28 was achieved in System 2.
- It was seen that  $\text{CO}_2$  emissions were reduced by 19.4% with the use of R1270.
- It was obtained that the variation of the evaporator temperature was much more effective on the cooling performance of the whole system. In addition, the use of R1270 refrigerant in the LTC cycle was found to be more efficient than R744.

As a result, it was observed that the R1270/R290 refrigerant pair was determined thermodynamically more efficient for the cascade refrigerant system. Therefore, it is important to experimentally examine this system and verify it with theoretical results in future studies. This study will make a great contribution to industrial refrigeration systems that care about environmental problems.

## CONFLICT OF INTEREST

The author deny any conflict of interest.

## REFERENCES

1. Coulomb A, Dupon D, Pichard JL. The Role of Refrigeration in the Global Economy-29th Informatory Note on Refrigeration Technologies. International Institute of Refrigeration, Paris, France (2015).
2. Catalan-Gil Jesús, Sanchez LR, Andres D, Ramon LC. Energy analysis of dedicated and integrated mechanical subcooled  $\text{CO}_2$  boosters for supermarket applications. International Journal of Refrigeration 101 (2019) 11–23.
3. Nicola GD, Polonara F, Stryjek R, Arteconi A. Performance of Cascade Cycles Working with Blends of  $\text{CO}_2$  Natural Refrigerants. International Journal of Refrigeration 34 (2011) 1436-1445.
4. Demirci E, Ozkaymak M, Kosan M, Akkoc AE, Aktas M. Doğal Soğutucu Akışkan Kullanımında Gelişmeler. Gazi Journal of Engineering Sciences 6(3) (2020) 184-199.
5. Abas N, Kalair AR, Khan N, Haider A, Saleem Z, Saleem MS. Natural and synthetic refrigerants, global warming: a review. Renewable Sustainable Energy Reviews 90 (2018) 557–569.
6. Luiz HPM, Raiza BCN, Stella MRC, Hugo VA, José VHA.

- Thermodynamic performance evaluation of a cascade refrigeration system with mixed refrigerants: R744/R1270, R744/R717 and R744/RE170. *International Journal of Refrigeration* 106 (2019) 201-212.
7. Kasi P, Cheralathan, M. Performance analysis of cascade refrigeration system with alternative refrigerants to reduce carbon emission. *Journal of Thermal Analysis and Calorimetry* 148 (2023) 4389–4399.
  8. Mofrad KG, Zandi S, Salehi G, Manesh MHK. 4E analyses and multi-objective optimization of cascade refrigeration cycles with heat recovery system. *Thermal Science and Engineering Progress* 19 (2020) 100613.
  9. Soni S, Mishra P, Maheshwari G, Verma DS. Theoretical estimation of efficiency defect in cascade refrigeration system using low global warming potential refrigerant pair. *Materials Today: Proceedings* 59(1) (2022) 1040-1044.
  10. Ozyurt A, Erdonmez N, Yılmaz B, Yılmaz D, Sevindir MK, Mancuhan E. CO<sub>2</sub>/NH<sub>3</sub> kaskat soğutma sisteminin termodinamik analizi ve performans değerlendirmesi. 12. Ulusal Tesisat Mühendisliği Kongresi, İzmir, (2015) 1101-1110.
  11. Sun Z, Liang Y, Liu S, Ji W, Zang R, Liang R, Guo Z. Comparative analysis of thermodynamic performance of a cascade refrigeration system for refrigerant couples R41/R404A and R23/R404A. *Applied Energy* 184 (2016) 19-25.
  12. Silva AD, Filho EPB, Antunes AHP. Comparison of a R744 Cascade Refrigeration System with R404A and R22 Conventional Systems or Supermarkets. *Applied Thermal Engineering* 41(2012) 30-35.
  13. Huang C, Li Z, Ye Z, Wang R. Thermodynamic study of carbon dioxide transcritical refrigeration cycle with dedicated subcooling and cascade recooling. *International Journal of Refrigeration* 137 (2022) 80-90.
  14. Chi W, Yang Q, Chen X, Liu G, Zhao Y, Li L. Performance evaluation of NH<sub>3</sub>/CO<sub>2</sub> cascade refrigeration system with ejector subcooling for low-temperature cycle. *International Journal of Refrigeration* 136 (2022) 162-171.
  15. Yan G, Hu H, Yu J. Performance evaluation on an internal auto-cascade refrigeration cycle with mixture refrigerant R290/R600a. *Applied Thermal Engineering* 75 (2015) 994-1000.
  16. Cabello R, Andreu-Nácher A, Sánchez D, Llopis R, Vidan-Falomir F. Energy comparison based on experimental results of a cascade refrigeration system pairing R744 with R134a, R1234ze(E) and the natural refrigerants R290, R1270, R600a. *International Journal of Refrigeration* 148 (2023) 131-142.
  17. Zhu YD, Peng ZR, Wang GB, Zhang XR. Thermodynamic analysis of a novel multi-target-temperature cascade cycle for refrigeration. *Energy Conversion and Management* 243 (2021) 114380.
  18. Calm JM, Hourahan GC. Refrigerant data summary. *Eng Syst* 18 (2001)74–78.
  19. Kilicarslan A, Hosoz M. Energy and irreversibility analysis of a cascade refrigeration system for various refrigerant couples. *Energy Conversion Management* 51 (2010) 2947–54.
  20. Alhamid MI, Syaka DR. Exergy and energy analysis of a cascade refrigeration system using R744+ R170 for low temperature applications. *International Journal of Mechanical and Mechatronics Engineering*. 10(6) (2010) 1-8.
  21. Erten S, Koşan M, Işgen F, Demirci E, Aktaş M. Thermodynamic Analysis of Industrial Cooling Systems with the Usage of Different Types of Evaporators: Experimental Study. *Gazi University Journal of Science*. 34(4) (2021) 1145-1161.
  22. Arora A, Kaushik SC. Theoretical analysis of a vapour compression refrigeration system with R502, R404A and R507A. *International Journal of Refrigeration* 31(6) (2008) 998–1005.
  23. Ust Y, Karakurt AS. Analysis of a Cascade Refrigeration System (CRS) by Using Different Refrigerant Couples Based on the Exergetic Performance Coefficient (EPC) Criterion. *Arabian Journal for Science and Engineering* 39 (2014) 8147–8156.
  24. Ust Y, Karakurt AS, Gunes U. Performance Analysis of Multipurpose Refrigeration System (MRS) on Fishing Vessel. *Polish Maritime Research* 23(2) (2016) 48-56.
  25. Tripathi R, Tiwari G, Dwivedi V. Overall energy, exergy and carbon credit analysis of N partially covered photovoltaic thermal (PVT) concentrating collector connected in series. *Solar Energy* 136 (2016) 260-267.

# Investigation of Deep Learning Approaches for Identification of Important Wheat Pests in Central Anatolia

Tolga Hayit<sup>1</sup>  Sadik Eren Kose<sup>2</sup> 

<sup>1</sup>Yozgat Bozok University, Department of Computer Engineering, Yozgat, Türkiye

<sup>2</sup>Yozgat Bozok University, Department of Computer Technology, Yozgat, Türkiye

## ABSTRACT

Artificial intelligence-based systems play a crucial role in Integrated Pest Management studies. It is important to develop and support such systems for controlling wheat pests, which cause significant losses in wheat production is of strategic importance, particularly in Turkey. This study employed various pre-trained deep learning approaches to identify key wheat pests in the Central Anatolia Region, namely *Aelia* spp., *Anisoplia* spp., *Eurygaster* spp., *Pachytychius hordei*, and *Zabrus* spp. The models' classification success was determined using open and original datasets. Among the models, the ResNet-18 model outperformed others, achieving a classification success rate of 99%. Furthermore, each model was tested with original images collected during field studies to assess their effectiveness. The results demonstrate that pre-trained deep learning models can be utilized for the identification of important wheat pests in Central Anatolia as part of Integrated Pest Management.

### Keywords:

Important wheat pests; Insect classification; Deep learning; CNN; Transfer learning; ResNet-18

## INTRODUCTION

For human beings to survive, there are basic needs such as breathing, shelter, and nutrition [1]. Agricultural production holds strategic importance in meeting the nutritional requirement of these needs. However, agricultural production faces various risks from production to marketing. The ability of agriculture to effectively meet nutritional needs is directly linked to controlling these risks. Crop losses caused by diseases, weeds, and pests are significant risks in production. Effective measures are required to mitigate these risks, which are considered plant protection issues. Failure to combat diseases, pests, and weeds results in an average yield loss of 36.5% (10.2% caused by insects) [2]. Integrated Pest Management (IPM) studies, incorporating the use of the least harmful methods to humans and the environment, are crucial in preventing losses caused by pests. Artificial intelligence-based fields such as computer vision, data mining, and expert systems play a pivotal role in IPM.

Artificial intelligence-based systems developed for plant health protection are particularly valuable for

the production of economically significant cereal crops. Among these crops, wheat holds the top position globally as well as in Turkey in terms of cultivation area and production volume, highlighting its strategic importance. According to Polat [3], data from the United States Department of Agriculture (USDA) indicates that wheat production accounts for 28% of the world's grain production, totaling 2.7 billion tons. The same study also highlights Turkey's crucial role in global wheat exports, ranking ninth during the 2019-2020 production season. Compared to other cereal crops, wheat, which occupies the top position among 162 crops worldwide, is an indispensable commodity due to its substantial production volume and trade value [4]. These facts underscore the significance of wheat for the global economy, particularly for Turkey.

In order to sustain wheat production, it is crucial to develop production techniques that increase the yield per unit area and effectively mitigate product losses. Wheat pests have garnered the attention of researchers due to their detrimental impact on wheat production, resulting in economic challenges and yield reductions.

### Article History:

Received: 2023/05/26

Accepted: 2023/09/13

Online: 2023/09/30

**Correspondence to:** Tolga Hayit,  
Yozgat Bozok University, Computer  
Engineering, 66900, Yozgat, TÜRKİYE  
E-Mail: [tolga.hayit@bozok.edu.tr](mailto:tolga.hayit@bozok.edu.tr);  
Phone: +90 354 217 8991/1120;  
Fax: +90 354 217 8991.

This article has been checked for similarity.



This is an open access article  
under the CC-BY-NC licence

<http://creativecommons.org/licenses/by-nc/4.0/>

### Cite as:

Hayit T, Kose S E. Investigation of Deep Learning Approaches for Identification of Important Wheat Pests in Central Anatolia. Hittite Journal of Science and Engineering 2023;10(3): 249–257. doi:10.17350/hjse19030000314



**Figure 1.** The important wheat pests in Central Anatolia, a: *Aelia* spp., *Anisoplia* spp., *Eurygaster* spp., *Pachytychius hordei*, *Zabrus* spp. [7].

There exist significant wheat pests that adversely affect both the yield and quality of wheat. In regions with a high population density, these pests, if left uncontrolled, can cause crop losses of up to 100% [5]. The Agricultural Control Technical Instructions provide a clear overview of the definition, life cycle, economic significance, distribution, and control measures for wheat pests [6]. Researchers and producers rely on these instructions to effectively manage major wheat pests. Fig. 1 presents images of these key wheat pests.

In recent years, significant progress has been made in using Machine Learning (ML) for pest detection and identification for crop protection. These works encompass both traditional approaches and modern Deep Learning (DL) techniques, such as Convolutional Neural Networks (CNN). CNN, being a prominent DL method, has gained extensive popularity, particularly in object identification tasks involving images [8-10]. CNN models possess a deep neural architecture comprising convolutional, pooling, and connected layers. Current agricultural studies based on deep learning provide evidence that CNN can effectively recognize diseases and pests in plant protection [11-22].

The successful outcomes of deep learning-based studies have served as the motivation for this research. However, the development of a successful and high-quality CNN model necessitates a well-curated dataset. Unfortunately, limited data availability and insufficient open access datasets pose as restricting factors when training CNN models.

This study employed modern deep learning approaches to identify crucial wheat pests in the Central Anatolia, including *Eurygaster* spp., *Aelia* spp., *Anisoplia* spp., *Pachytychius hordei*, and *Zabrus* spp. The classification success of the models was evaluated using pre-trained deep learning

models, namely AlexNet, ResNet-18, and InceptionV3 CNN networks. Open access datasets containing images of these significant wheat pests were utilized to train the models. The contributions of this study are evident in its application of modern deep learning techniques, its emphasis on identifying crucial wheat pests, the evaluation of deep learning models, its utilization of open-access and original datasets, and its potential to enhance agriculture and advance agricultural research in the Central Anatolia.

The remainder of the paper is organized as follows: the second section provides a detailed description of the dataset and methodology employed, the third section discusses the findings and presents a comparative performance analysis, and the final section presents the concluding remarks on the study.

## MATERIAL AND METHODS

### Dataset

The Agricultural Control Technical Instructions [6] provide a comprehensive overview of the definition, life cycle, economic significance, distribution, and control measures for wheat pests. Through field surveys, original images of the *Eurygaster* spp. pest were obtained and used for the final testing of the best model. However, the limited quantity and diversity of the original data hindered the ability to train and validate the models effectively. To address this issue, open data sets have been employed.

The Global Biodiversity Information Facility (GBIF) is an international data network funded by governments, aiming to provide open access to various life-related data [23]. GBIF encompasses numerous data sets. In this study,

**Table 1.** The raw dataset statistics [24-28].

<i>Aelia</i>	<i>Anisoplia</i>	<i>Eurygaster</i>	<i>Pachytychius</i>	<i>Zabrus</i>	TOTAL
333	301	310	108	183	1235



**Figure 2.** Sample images from the dataset, (a): *Aelia* [24], (b): *Anisoplia* [25], (c): *Eurygaster* [26], (d): *Pachytychius* [27], (e): *Zabrus* [28].

**Table 2.** Final dataset statistics.

	<i>Aelia</i>	<i>Anisoplia</i>	<i>Eurygaster</i>	<i>Pachytychius</i>	<i>Zabrus</i>	TOTAL
Training	350	350	350	350	350	1750
Validation	50	50	50	50	50	250
Test	100	100	100	100	100	500
<b>TOTAL</b>	<b>500</b>	<b>500</b>	<b>500</b>	<b>500</b>	<b>500</b>	<b>2500</b>



**Figure 3.** Augmented forms of a sample *Aelia* image: (a) original image, (b) brightness modified, (c) contrast modified, (d) horizontal flipped, (e) vertical flipped, (f) random rotated.

the raw data utilized for training, validation, and testing of the models were obtained from GBIF open data sets. Table 1 presents the statistics of the raw data set, while Fig. 2 shows sample images for each pest species. In the experimental studies, each pest was denoted by its scientific name.

The number of data sets was sufficient for training the deep learning models. However, in order to avoid issues such as overfitting and underfitting, it was necessary to balance the amount of data in each class. Particularly, due to the disparity in the amount of data between the *Pachytychius* and *Zabrus* classes, data augmentation techniques were employed, which are widely used in such cases [29-31]. This approach helped equalize the number of images in each class and achieve a balanced distribution of data across classes.

The final data set, created through data augmentation, was divided into three groups: training (70%), validation (10%), and test (20%). The models developed during the training and validation process were subsequently tested using the independent test dataset (20%), and the results were compared with the validation outcomes. Table 2 provides details regarding the number of final datasets generated as a result of the data augmentation process, while Fig. 3 shows augmented versions of a sample *Aelia* image.

In addition, a total of 423 original *Eurygaster* images were collected through field surveys conducted in March 2022. These images served as the original dataset for the study and were used for testing the models, in addition to

the designated test dataset. Note that due to field and weather conditions, only images of *Eurygaster* could be acquired. Sample images from the original *Eurygaster* dataset are presented in Fig. 4.

### Convolutional Neural Networks and Transfer Learning

A Convolutional Neural Network (CNN) is a deep learning model composed of interconnected layers that can automatically learn features from images within different classes. CNNs are extensively utilized, particularly in multi-class image classification tasks. Recent research demonstrates that CNN approaches can mimic human learning from images, achieving performance on par with or even surpassing human capabilities.

A CNN network can be trained from scratch or use "pre-trained" models that have been trained on large-scale datasets for specific tasks. This technique, known as "Transfer Learning," allows for improved performance with reduced training time, especially for tasks that require extensive datasets [32]. Numerous pre-trained CNN models, such as AlexNet [33], ResNet-18 [34], and InceptionV3 [35], are available, each suitable for identifying important wheat pests. In this study, we employed the AlexNet, ResNet-18, and InceptionV3 models.

AlexNet, introduced by Krizhevsky et al. [33], demonstrated superior performance in the ImageNet image classifi-

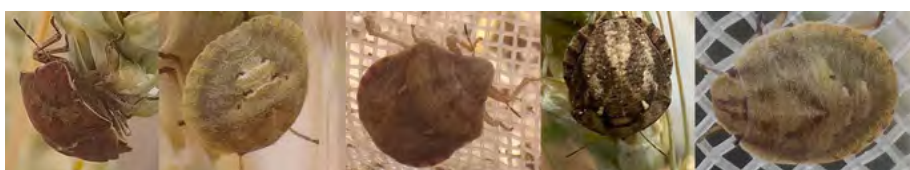


**Figure 4.** Sample images of the *Eurygaster* original dataset.



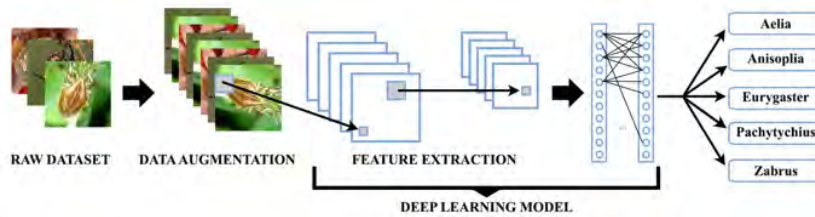


**Figure 5.** Proposed model workflow: pest images are passed to the CNN (Deep Learning Model), which automatically learns features and classifies pests.

cation task. AlexNet achieved victory in the 2012 ImageNet competition by attaining a top-5 error rate of 15.3%, surpassing the second-place error rate of 26.2%. It has a total of 8 learned layers. These layers include 5 convolutional layers and 3 fully connected layers. The activation function used on the AlexNet network is ReLU (Rectified Linear Unit), and maximum pooling is employed to reduce the dimensionality of the hidden layers. The output of the last fully connected layer is fed into the SoftMax function for class prediction.

ResNet [34], introduced by He et al., achieved first place in the ImageNet classification with a top-5 error rate of 3.57% in 2015. ResNet-18 consists of 18 layers in total, out of which 16 layers are trainable. The other two layers are the input layer and the final fully connected layer. ResNet-18, an enhanced version of the basic model.

Inception [36], also known as GoogLeNet, outperformed other models in the ImageNet classification task, achieving a top-5 error rate of 6.67% in 2014. InceptionV3 [35], an improved and optimized version of GoogLeNet, and it has a total of 48 trained layers. These layers include convolutional layers, pooling layers, fully connected layers, and auxiliary classifiers. InceptionV3 offers higher efficiency compared to previous models and requires less computational cost.

### Freezing Layers

During training, specific layers' weights within the CNNs are immobilized, remaining unchanged throughout the fine-tuning process. This technique is commonly employed for the initial layers, which primarily capture fundamental features. In opposition, the upper layers concentrate on extracting task-specific discriminative features and therefore remain unfrozen.

### The Proposed Model

This paper presents a deep learning model based on transfer learning, utilizing pre-trained CNN models. The task involves the identification of important wheat pests in the Central Anatolia region. The pre-trained CNN models used in this study include AlexNet, ResNet-18, and InceptionV3. Data augmentation was performed

using the Python programming language and the OpenCV (Open Computer Vision) library, while MATLAB software was employed for training, validation, and testing of the models.

The training process involved utilizing 1750 pest images of significant wheat pests obtained from open datasets. During training, each model was validated using 250 images. The final models were created upon completion of the training process. Fig. 5 provides a visual representation of the main steps in the workflow of the proposed deep learning-based classification model.

### Performance Metrics

To assess the performance of the CNN models, a confusion matrix was computed to evaluate both the average and classwise performance. As the proposed model predicts one of the five pest types, the resulting confusion matrix, denoted as  $C(m,n)$ , is a  $5 \times 5$  matrix. Based on the confusion matrix, various performance metrics were measured to determine the accuracy, precision, sensitivity, and F1-Score values of the models, providing insights into their overall performance and class-specific performance.

## RESULTS

Throughout the experiments, the AlexNet, ResNet-18, and InceptionV3 CNN models were trained and validated using the open dataset. However, it was observed that the models based on ResNet-18 and InceptionV3 achieved the highest accuracy values. The validation accuracy of these models is presented in Table 3.

From the analysis of Table 3, it is evident that the ResNet-18 and InceptionV3 models performed comparably well. However, in this case, the focus shifts towards the complexi-

**Table 3.** The validation accuracy rates (%).

Model	Accuracy
AlexNet	97.6
<b>ResNet-18</b>	<b>99.6</b>
InceptionV3	99.2

**Table 4.** Hyperparameters of the models: Hyperparameters were defined such as the learning rate was assigned 0.00001, and also *Adam* was used as an optimizer.

Optimizer	Adam
Loss function	Categorical cross entropy
Momentum	0.9
Initial Learning rate	1.0000e-05
Early stopping patience	10
Maximum epoch	20
Mini batch size	8
Shuffle	Every epoch

ties of the models and the associated workloads rather than their success rates. Despite InceptionV3's strong performance in previous studies, it possesses a more complex structure when compared to the ResNet-18 architecture. Additionally, considering the number of layers (ResNet-18 has 18 layers, while InceptionV3 has 48 layers), ResNet-18 offers a lightweight architecture. Herein, it is worth noting that the training of the ResNet-18 model was completed in approximately 12 minutes, whereas the InceptionV3 model required around 84 minutes for training. Thus, despite the close average accuracy values between the models, the ResNet-18 model is considered more successful due to its shorter training time and lightweight architecture.

The parameter settings of the learners used for training and testing in this study are presented in Table 4. The main parameters employed for configuring the learners' settings include InitialLearnRate, MaxEpoch, and MiniBatchSize. In the domain of machine learning and statistics, the learning rate serves as a critical tuning parameter within optimization algorithms, governing the magnitude of each step taken during iterations to approach the minimum of a loss function. One MaxEpoch entails a complete iteration of a training algorithm across the entire training dataset. Con-

versely, a MiniBatchSize refers to the number of images processed within each individual iteration.

Following multiple rounds of experimentation, the chosen MaxEpoch for this research is 20. Given the limited quantity of training datasets, the mini-batch size is typically opted to be small, falling between 4 to 64, preferably in powers of 2. This selection aims to ensure effective utilization of the datasets while minimizing wastage. As a result, the MiniBatchSize designated for this study is 8.

After each fully connected layer, batch normalization and dropout techniques are implemented. Hyperparameters, including a learning rate of 0.00001, along with the utilization of the Adam optimizer, were defined. While the initial 12 convolutional and separable convolution layers remained unchanged (frozen) throughout the training process, the upper layers underwent fine-tuning.

Both training and validation accuracy graphs were plotted using categorical cross-entropy as the loss function for ResNet-18, see Fig. 6.

During the training process, it was observed that both the training and validation accuracy consistently improved over time. Furthermore, a loss graph was generated to visualize the training process, as depicted in Fig. 7. The training loss and validation loss graphs demonstrate a decreasing trend throughout the training iterations, and their behavior closely resembles each other.

Relying solely on average accuracy is not sufficient to determine the success of CNN models. To address this limitation, a separate test was conducted for each model using 500 pest images (20% of the total dataset) listed in Table 2. These images were not encountered by the models during the training process. It was observed that the test performance of all models closely aligned with their average accu-

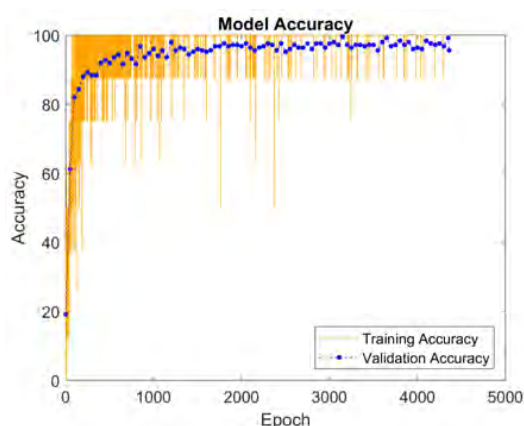


**Figure 6.** The ResNet-18 model was trained for 20 epochs and the training-validation accuracies were presented after each epoch.

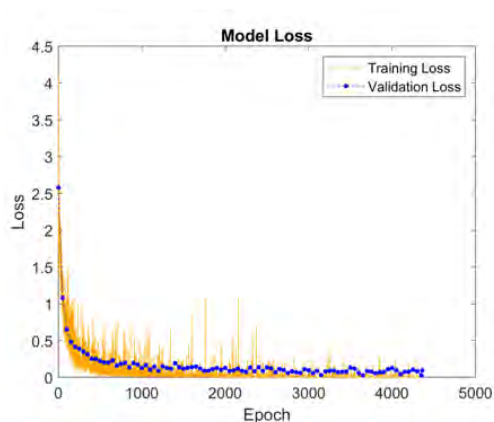


**Figure 7.** The ResNet-18 model was trained for 20 epochs and the training-validation loss values were presented after each epoch.

**Table 5.** The test accuracy rates (%).

Model	Accuracy	Precision	Recall	F1-Score
AlexNet	97.6	0.97	0.98	0.97
<b>ResNet-18</b>	<b>99.4</b>	<b>0.99</b>	<b>0.99</b>	<b>0.99</b>
InceptionV3	99.0	0.99	0.99	0.98

racy performance (Table 5). This result indicates that each model exhibited good generalization capabilities for the given problem. Note that the ResNet-18 model, which demonstrated the best performance in terms of training time, achieved an average test accuracy (99.4%) that was almost identical to the average accuracy.

The confusion matrix, is a table commonly used to visualize the performance of supervised learning algorithms in ML. Each row of the matrix corresponds to instances in a true class, while each column represents instances in a predicted class. For classification problems, the confusion matrix summarizes the count or percentage of correct and incorrect predictions. The term 'confusion' in the name arises from the matrix's ability to reveal whether the system is causing confusion between classes.

In Fig. 8, we present the confusion matrix, providing a detailed analysis of the performance of the most successful models for each class. The diagonal cells, highlighted in blue within the confusion matrix, indicate the number of accurate classifications made for each respective class. Note that

the InceptionV3 model misclassified 3 images belonging to the *Eurygaster* pest class. However, both models achieved 100% accuracy in recognizing the *Aelia* pest class.

On the other hand, the confusion matrix was utilized to calculate the average test accuracy, as well as metrics such as precision, recall, and F1-Score. These metrics, along with the average accuracy, consistently supported the notion that the models were capable of effectively classifying the important wheat pests. A comprehensive breakdown of the performance of the ResNet-18 model for each class can be found in Table 6.

The models were subsequently subjected to testing using the original dataset of 423 Eurygaster images (see 'Dataset' section). The experimental results revealed that the best-performing models, ResNet-18 and InceptionV3, achieved accuracies of 97% and 92% respectively. These findings demonstrate that the models exhibit robust generalization capabilities and can be effectively applied to real-world scenarios.

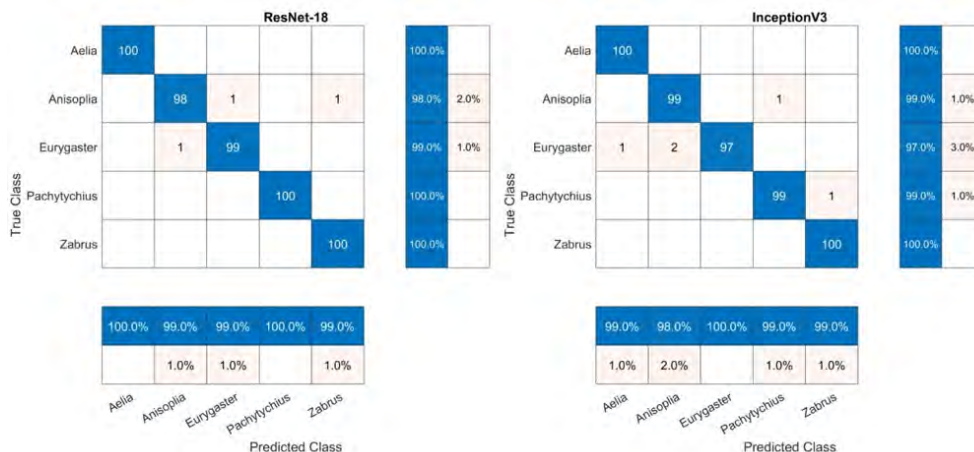


**Figure 8.** The confusion matrix for the best models trained on the dataset, on the left by ResNet-18 and on the right by InceptionV3.

**Table 6.** Classwise performance comparison for ResNet-18.

Metric	<i>Aelia</i>	<i>Anisoplia</i>	<i>Eurygaster</i>	<i>Pachytychius</i>	<i>Zabrus</i>	TOTAL
Precision	1.0	0.98	0.99	1.0	1.0	0.99
Recall	1.0	0.99	0.99	1.0	0.99	0.99
F1-Score	1.0	0.98	0.99	1.0	1.0	0.99

## DISCUSSION

Based on the experimental results, it is evident that the pre-trained CNN models successfully identified significant wheat pests in Central Anatolia. The dataset, comprising five crucial pests, was utilized across all methodologies. The best performance achieved was 99.4%. The same hyperparameters were employed for all classifications to ensure a fair comparison.

The confusion matrix provided a detailed analysis of the performance of the models for each class. Therefore, it can be concluded that the models successfully classify each class.

Utilizing transfer learning (TL) as a deep learning technique involves employing a pre-trained model from an extensive dataset for a specific task within a certain domain. This pre-trained model serves as a foundation for tackling a different task within a similar domain, even when there is limited labeled data available. Models based on transfer learning (pre-trained) require a shorter training duration when compared to models trained entirely from scratch [32]. The popular pre-trained CNN classification models are documented in the literature [37], including AlexNet, ResNet, and Inception. These models are robust methods for image classification and effective object identification [33-36]. It has also been demonstrated that these models exhibit better accuracy and computational efficiency compared to other CNN models in some studies. The pre-trained CNN models most frequently employed in pest classification studies [11-22] serve as the foundation of our deep learning strategy.

Finally, the results of this paper and related studies are presented in Table 7. The contribution of deep models to classification performance is evident in both other studies as the study. Consequently, CNN models can serve as a fo-

undational component of a portable system integrated with hardware, which can be utilized by farmers or researchers to identify various pest species in real-world environments.

Pest classification is a novel and increasingly popular field within the realm of computer vision. While there exist methodological similarities, our study exhibits notable distinctions when considering the dataset employed. Importantly, we assert that our research carries national significance, as it identifies critical pest species within the Central Anatolia region. Furthermore, the chosen pest species are those that impose the most substantial damage upon wheat.

## CONCLUSION AND SUGGESTIONS

This study demonstrated the effectiveness of pre-trained CNN models for the identification of important wheat pests in Central Anatolia. The results of the analysis, which involved a five-way classification task using transfer learning, indicated an average test accuracy of approximately 99% (see Table 5). Furthermore, metrics such as precision, recall, and F1-Score, provided in Table 6, further supported the success of the models.

Comparing the accuracy and loss graphs, as well as considering the performance on the original dataset, it can be concluded that CNN models integrated into mobile systems for real-world applications can be reliably employed to identify significant wheat pests in Central Anatolia. Future works could involve testing and comparing the performance of these models using original datasets that include other pests. Additionally, it would be valuable to explore the use of traditional models alongside deep learning models and compare their performances. Encouraging the continuation of similar research endeavors is crucial for effectively managing factors that pose a serious threat to wheat production.

**Table 7.** Related work and accuracy results (%) summary.

Study	Other CNN	AlexNet	ResNet	Inception	Class
<b>Proposed work</b>	-	<b>97.6</b>	<b>99.4</b>	<b>99</b>	<b>5</b>
Zhu et al. [11]	99.60	100	-	-	22
Xia et al. [13]	89.22	-	-	-	24
Thenmozhi and Reddy [16]	97.47	94.23	95.95	-	24
Nanni et al. [18]	92.10	92.43	-	90.77	10
Ayan et al. [19]	98.81	-	92.18	97.06	40
Visalli et al. [20]	98.39	-	-	-	11
Kasinathan et al. [21]	91.5	-	-	-	9
Kasinathan et al. [21]	90	-	-	-	24
Zheng et al. [22]	98.4	89.0	92.0	-	30

Note: Best results of the studies were represented; models (if used) and their performance are presented for each study.

## ACKNOWLEDGEMENT

This study was supported by project 1919B012107851 no. within the scope of the 2209-A University Students Research Projects Support Program carried out by the Science Fellowships and Grant Programmes Department (TU-BİTAK BİDEB). We also thank the Directorate of Plant Protection Central Research Institute, the Republic of Türkiye Ministry of Agriculture and Forestry for support in obtaining the original dataset.

## CONFLICT OF INTEREST

The authors declare that they have no potential conflict of interest.

## AUTHOR CONTRIBUTION

Tolga Hayit designed the models and analysed the data, and also wrote the manuscript and read and approved the final manuscript. Sadik Eren Kose collected original images and contributed image processing work.

## References


1. Maslow AH. A theory of human motivation. *Psychol Rev.* 1943 50(4):370-396.
2. Agrios NG. *Plant pathology.* San Diego (USA): Elsevier Academic Press; 2005.
3. Polat K. Tarım Ürünleri Piyasaları [Internet]. Turkey (SGB): Tarımsal Ekonomi ve Politika Geliştirme Enstitüsü; 2021 [reviewed 2022 Dec 15; cited 2022 Dec 20]. Available from: <https://arastirma.tarimorman.gov.tr/tepge/Belgeler/PDF%20Tar%C4%B1m%20%C3%9Cr%C3%BCnleri%20Piyasalar%C4%B1/2021-Ocak%20Tar%C4%B1m%20%C3%9Cr%C3%BCnleri%20Raporu/Bu%C4%9Fday,%20Ocak%202021,%20Tar%C4%B1m%20%C3%9Cr%C3%BCnleri%20Piyasa%20Raporu.pdf>
4. FAO. *World Food and Agriculture – Statistical Yearbook 2022.* Rome: <https://doi.org/10.4060/cc2211en>; 2022.
5. Babaroğlu NE, Akci E, Çulcu M, Yalçın F. Süne ve Mücadelesi. Ankara (TR): Tarım ve Orman Bakanlığı Gıda ve Kontrol Genel Müdürlüğü; 2020.
6. Ziraî Mücadele Teknik Talimatları Cilt 1. Ankara (TR): Gıda Tarım ve Hayvancılık Bakanlığı Tarımsal Araştırmalar ve Politikalar Genel Müdürlüğü Bitki Sağlığı Araştırmaları Daire Başkanlığı; 2008.
7. Hububat Zararlıları [Internet]. [place unknown: publisher unknown]; [reviewed 2022 Dec 16; cited 2022 Dec 20]. Available from: <https://arastirma.tarimorman.gov.tr/zmmae/Belgeler/Sol%20Menu/Zirai%20M%C3%BCcadele%20Rehberi/Hububat/Hububat-Zararlı%C4%B1.pdf>
8. LeCun Y, Bengio Y, Hinton G. Deep learning. *Nature.* 2015;521(7553):436-444.
9. Hayit T, Erbay H, Varçın F, Hayit F, Akci N. Determination of the severity level of yellow rust disease in wheat by using convolutional neural networks. *JPP.* 2021;103(3):923-934.
10. Hayit T, Erbay H, Varçın F, Hayit F, Akci N. The classification of wheat yellow rust disease based on a combination of textural and deep features. *Multimedia Tools and Applications.* 2023:1-19.
11. Zhu LQ, Ma MY, Zhang Z, et al. Hybrid deep learning for automated lepidopteran insect image classification. *Oriental Insects.* 2017;51(2):79-91.
12. Lim S, Kim S, Kim D. Performance effect analysis for insect classification using convolutional neural network. In 2017 7th IEEE International Conference on Control System, Computing and Engineering. 2017; Penang, Malaysia; 2017. p. 210-215.
13. Xia D, Chen P, Wang B, Zhang J, Xie C. Insect detection and classification based on an improved convolutional neural network. *Sensors.* 2018;18(12):4169.
14. Marques ACR, Raimundo MM, Cavalheiro EMB, et al. Ant genera identification using an ensemble of convolutional neural networks. *Plos One.* 2018;13(1):e0192011.
15. Lu CY, Rustia DJA, Lin TT. Generative adversarial network based image augmentation for insect pest classification enhancement. *IFAC-PapersOnLine.* 2019;52(30):1-5.
16. Thenmozhi K, Reddy US. Crop pest classification based on deep convolutional neural network and transfer learning. *Comput Electron Agric.* 2019;164(104906).
17. Hansen OL, Svenning JC, Olsen K, et al. Species-level image classification with convolutional neural network enables insect identification from habitus images. *Ecol Evol.* 2020;10(2):737-747.
18. Nanni L, Maguolo G, Pancino F. Insect pest image detection and recognition based on bio-inspired methods. *Ecol Inform.* 2020;57(101089).
19. Ayan E, Erbay H, Varçın F. Crop pest classification with a genetic algorithm-based weighted ensemble of deep convolutional neural networks. *Comput Electron Agric.* 2020;179(105809).
20. Visalli F, Bonacci T, Borghese NA. Insects image classification through deep convolutional neural networks. *Prog Artif Intell.* 2021:217-228.
21. Kasinathan T, Singaraju D, Uyyala SR. Insect classification and detection in field crops using modern machine learning techniques. *Inf Process Agric.* 2021;8(3):446-457.
22. Zheng T, Yang X, Lv J, Li M, Wang S, Li W. An efficient mobile model for insect image classification in the field pest management. *IJEST.* 2023;39(101335).
23. GBIF.org. What is GBIF? [Internet]. Copenhagen (DK); 2022 [reviewed 2023 Jan 05; cited 2023 Jan 20]. Available from: <https://www.gbif.org/what-is-gbif>
24. GBIF.org. Aelia images. Copenhagen (DK); 2023 [reviewed 2023 Jan 10; cited 2023 Jan 10]. Available from: <https://doi.org/10.15468/dl.x52gqx>
25. GBIF.org. Anisoplia images. Copenhagen (DK); 2023 [reviewed 2023 Jan 08; cited 2023 Jan 08]. Available from: <https://doi.org/10.15468/dl.3k29je>
26. GBIF.org. Eurygaster images. Copenhagen (DK); 2023 [reviewed 2023 Jan 08; cited 2023 Jan 08]. Available from: <https://doi.org/10.15468/dl.7sz7cp>
27. GBIF.org. Pachytychius images. Copenhagen (DK); 2023 [reviewed 2023 Jan 08; cited 2023 Jan 08]. Available from: <https://doi.org/10.15468/dl.fh8q57>
28. GBIF.org. Zabrus images. Copenhagen (DK); 2023 [reviewed 2023 Jan 05; cited 2023 Jan 05]. Available from: <https://doi.org/10.15468/dl.tp43zy>
29. Moreno-Barea FJ, Jerez JM, Franco L. Improving classification accuracy using data augmentation on small data sets. *Expert Syst Appl.* 2020;161(113696).
30. Tian X, Ding CH, Chen S, Luo B, Wang X. Regularization graph convolutional networks with data augmentation. *Neurocomputing.* 2021;436:92-102.

31. Oyelade ON, Ezugwu AE. A deep learning model using data augmentation for detection of architectural distortion in whole and patches of images. *Biomed Signal*.2021;65(102366).
32. Mohanty SP, Hughes DP, Salathé M. Using deep learning for image-based plant disease detection. *Front Plant Sci*. 2016;7(1419).
33. Krizhevsky A, Sutskever I, Hinton GE. Imagenet classification with deep convolutional neural networks. *Commun*. 2017;60(6):84-90.
34. He K, Zhang X, Ren S, Sun J. Deep residual learning for image recognition. *Proceedings of the IEEE conference on computer vision and pattern recognition*; 2016; Las Vegas, NV, USA.
35. Szegedy C, Vanhoucke V, Ioffe S, Shlens J, Wojna Z. Rethinking the inception architecture for computer vision. *Proceedings of the IEEE conference on computer vision and pattern recognition*; 2016. p. 2818-2826.
36. Szegedy C, Liu W, Jia Y, et al. Going deeper with convolutions. *Proceedings of the IEEE conference on computer vision and pattern recognition*; 2015. p. 1-9.
37. Sultana F, Sufian A, Dutta P. Advancements in image classification using convolutional neural network. In *2018 Fourth International Conference on Research in Computational Intelligence and Communication Networks (ICRCICN)*. 2018 Nov. p. 122-129.



# On The Blind Denoising Efficiency of Image Denoising Algorithms Through Robustness, Image Quality and Computational Burden

Kenan Gencol 

 Hitit University, Department of Electrical and Electronics Engineering, Corum, Türkiye

## ABSTRACT

The main goal of the image denoising is to recover the original image while attaining the structure of the image as much as possible. When the image denoising task is blind, we have no a priori information about the original image. Thus, we cannot measure the degradation level in the image directly; instead, noise variance can be estimated by the denoising algorithm. According to the estimated value, denoising is performed. Such algorithms are supposed to be robust to varying and high levels of noise interference. Moreover, in time-constrained real-world applications, they must balance the tradeoff between image quality and computation time. In this study, we assess the performance of the image denoising algorithms armored for these goals. We are aimed to determine the optimal performance yielded by such algorithms and the noise bounds wherein each algorithm is superior. After the experimental work, important conclusions are drawn.

### Keywords:

Image processing; Image analysis; Image denoising; Filtering; Noise

## INTRODUCTION

Let  $s(t)$  be a reference signal corrupted by additive white Gaussian noise (AWGN), i.e.  $sN(t) = s(t) + w(t)$  where  $w(t) \sim N(0, a^2)$  is AWGN with zero mean and  $a^2$  variance. When  $s(t)$  is considered to be an image signal, the main goal of image denoising is to recover signal  $s(t)$  while preserving image structures and features as much as possible. In the process of recovering original signal, the suppression of noise and preservation of image details is a compromise. Noise can be due to imperfections in camera sensory systems and imaging process, different sources of noise such as photon, thermal and quantization noise, poor illumination conditions, etc.

One of the oldest and simplest methods of denoising is to average the image spatially. This process acts as a low-pass filter and removes the noise by smoothing it. In smoothing operations, the pixels that have significantly higher or lower intensity values would smear across neighboring pixels and thus create blur. Similarly, neighborhood filters which take an input pixel and apply an algorithm to neighbor pixels of the corresponding pixel create shocks and artifacts [1,2]. To address the blurring problems of spatial and neighborhood filters anisotropic diffusion filter [3] was designed by Perona

and Malik to avoid the blurring effects of spatial and neighborhood filters. This filter smooths the image in the direction that is orthogonal to the gradient direction. Also, a minimization technique called total variation filter [4] designed by Rudin et al. acts for the same goal. Unfortunately, these two approaches are fairly slow and come with more computation burden compared to aforementioned spatial techniques. It is a fact that noise commonly manifests itself as fine grained structure in images. Many researches have been conducted addressing this phenomenon. Wavelet based techniques [5–7] rely on this phenomenon. In wavelet domain, most of the noise is represented by wavelet coefficients at finer scales. The coefficients are thresholded to get rid of unwanted noise. The main handicap of wavelet thresholding techniques is that the chosen threshold may not match the specific distribution of image signal. Also, hard thresholding would create visual artifacts and soft thresholding would create blur in the recovered image. Nonlinear estimators based on Bayesian theory attempt to overcome the disadvantages of wavelet based methods at cost of high computation burden [8]. On the other hand, an algorithm called Non-Local Means [9–10] brought a new perspective to image denoising task. This algorithm have for the first time used patch-wise pixel

### Article History:

Received: 2023/05/26

Accepted: 2023/09/13

Online: 2023/09/30

**Correspondence to:** Kenan Gencol,  
Hitit University, Electrical and Electronics  
Engineering, 19030, Corum, TÜRKIYE  
E-Mail: kenangencol@hitit.edu.tr;  
Phone: +90 364 219 1302;  
Fax: +90 364 219 1399.

This article has been checked for similarity.



This is an open access article  
under the CC-BY-NC licence

<http://creativecommons.org/licenses/by-nc/4.0/>

### Cite as:

Gencol K, "On The Blind Denoising Efficiency of Image Denoising Algorithms Through Robustness, Image Quality and Computational Burden". Hittite Journal of Science and Engineering 2023;10(3): 259–267. doi:10.17350/hjse19030000315



operations instead of point-wise pixel operations. As a second contribution, the algorithm has considered the patches physically not near the pixel of interest and hence having its name as nonlocal. Following this, the search for optimally designing a filter that maximizes the signal-to-noise ratio (SNR) for each component of the signal in Wiener filter resulted an algorithm that is still considered as the state-of-the-art called Block-Matching and 3-D Filtering (BM3D) [11]. This algorithm stacks the 2-D noisy image patches into 3-D groups and then a high-dimensional filtering approach called collaborative filtering is employed. This latter operation includes 3-D transform, shrinkage and inverse transform of image data. Recently, some image denoising techniques based on deep learning appear [12]. But, these methods need lots of data for training and are not yet mature to be employed in real-world denoising operations. Interested readers can refer to [13] for more comprehensive review of the image denoising algorithms.

The remainder of the paper is organized as follows. In the next section, the algorithms suitable for blind image denoising are briefly explained. Then, the results obtained on the basis of quality, robustness and computation time are presented and discussed. Finally, some concluding remarks are given.

## MATERIAL AND METHODS

In this section, we introduce the problem of image denoising and briefly explain the algorithms suitable for blind image denoising. Gaussian, Wiener, NLM, Wavelet hard and soft denoising methods, and BM3D are evaluated and the results are presented in terms of image quality metrics and computational efficiency.

### Problem Definition

Let the problem be modeled as

$$y(i, j) = x(i, j) + n(i, j) \quad (1)$$

where  $x(i, j)$  is the noise-free input image,  $n(i, j) \sim N(0, \sigma^2)$  is AWGN and  $y(i, j)$  is the noisy image observed. We would like to obtain an estimate  $\hat{x}$  of the original image,  $x$ . A relatively simple approach is to convolve (or correlate) the noisy image with a lowpass kernel centered at  $(i, j)$  in spatial domain, i.e.,

$$\hat{x} = y * h \quad (2)$$

where  $\hat{x}$  is the estimate of noise-free image and  $h$  is the  $N \times N$  kernel with weights satisfying the general rule:  $\sum w(i, j) = 1$ . The simplest weighted averaging filter is the average (or smoothing) filter with weights  $1/(N \times N)$ , 2-D, an isotropic (i.e., circularly symmetric) Gaussian filter [14] has the form:

$$w(i, j, k, l) = w(|i - k|, |j - l|) \\ = \frac{1}{\sum_{k,l} w(i, j, k, l)} e^{-(i-k)^2 + (j-l)^2} \quad (3)$$

### Wiener Filter

In wiener filtering, the goal is to obtain a linear estimate of the noise-free image,  $\hat{x}(i, j)$  of the size  $M \times N$  that minimizes the mean squared error (MSE), i.e.

$$MSE = \frac{1}{MN} \sum_{i,j=1}^{i,j=M,N} (\hat{x}(i, j) - x(i, j))^2 \quad (4)$$

This linear estimate is given by

$$\hat{x}(i, j) = \frac{\sigma_x^2(i, j)}{\sigma_x^2(i, j) + \sigma_n^2(i, j)} [y(i, j) - \mu_x(i, j)] \\ + \mu_x(i, j) \quad (5)$$

where  $\sigma_x^2$  and  $\mu_x$  are the signal variance and the mean of the original image and  $\sigma_n^2$  is the variance of noise, respectively. The wiener filter is optimal when  $x(i, j)$  and  $n(i, j)$  are stationary Gaussian processes.

### Non-local Means (NLM)

The NLM method aims to take advantage of the high degree of redundancy found in any natural images. It uses the fact that every small window in a natural image has many similar windows in the same image:

$$NL[x](i) = \sum_{j \in I} w(i, j) v(j) \quad (6)$$

where weighting kernel  $w(i, j)$  depends on the similarity between the pixels  $i$  and  $j$ :

$$w(i, j) = \frac{1}{Z(i)} e^{-\frac{\|v(N_i) - v(N_j)\|^2}{h^2}} \quad (7)$$

and  $Z(i)$  is the normalizing constant:

$$Z(i) = \sum_i e^{-\frac{\|v(N_i) - v(N_j)\|^2}{h^2}} \quad (8)$$

where  $h$  is the size of the kernel. In this approach, the Euclidean distance  $\|\cdot\|$  between two pixels in the bilateral filter [15, 16] is replaced by the weighted Euclidean distance between two patches. Moreover, the Euclidean distance in the weight function is substituted with a Gaussian. Thus, it can be considered as a variation of the neighborhood filter [17].

### Wavelet-based Denoising

In wavelet-based denoising, the image is decomposed into subbands (LL, LH, HL, HH) by the wavelet transform as shown in Fig.1. Then, coefficients of the detail subbands are compared with a threshold value and modified ac-



**Figure 1.** A sample image 'Barbara' and 2-D wavelet decomposition of the image. From top left to bottom right: LL, LH, HL, and HH (detail) subbands.

ording to some thresholding rules. Finally, the image is reconstructed from the updated wavelet coefficients by performing inverse wavelet transform. Generally, there are two thresholding rules: hard-thresholding and soft-thresholding. In hard-thresholding, wavelet coefficients that are smaller than or equal to the threshold value  $T$  are set to zero and the others are kept:

$$T_H(x) = \begin{cases} 0, & |x| \leq T \\ x, & \text{otherwise} \end{cases} \quad (9)$$

On the other hand, in soft thresholding, wavelet coefficients that are larger than the threshold value are shrunk towards to zero by a factor of  $T$ :

$$T_S(x) = \begin{cases} 0, & |x| \leq T \\ \text{sign}(x) \cdot (|x| - T), & \text{otherwise} \end{cases} \quad (10)$$

Thus, we refer to this latter procedure as the wavelet shrinkage. Here, the signum function  $\text{sign}(\cdot)$  preserves the sign of the wavelet coefficients.

### Block-Matching and 3-D Filtering (BM3D)

BM3D is essentially based on Wiener filtering. BM3D clusters the 2-D noisy image patches or blocks that have similar local structures into stacked 3-D groups. Then, a higher dimensional filtering called collaborative filtering is applied to exploit potential similarity between groups. Collaborative filtering reveals the fine details in 3-D groups and preserves the unique features of each group. This filtering operation is realized in three successive steps: 3-D transform of the group, shrinkage of the transform spectrum and the inverse 3-D transform. 3-D transform includes the 2-D transform within a group such as DCT or wavelets and the 1-D transform across groups such as

Haar wavelet. Shrinkage by hard-thresholding or wiener filtering is employed to attenuate noise in transform domain. Finally, estimates of grouped fragments are produced by inverting from the transform domain.

### Evaluation Criteria

In order to evaluate the performance of the denoising algorithms, we have used two quality metrics: Peak Signal-to-Noise Ratio (PSNR) and Structural Similarity Index Measure (SSIM) [18]. Given a reference image  $x$ , the PSNR of the denoised image  $\hat{x}$  is defined as:

$$PSNR(x, \hat{x}) = 10 \log_{10} \left( \frac{255^2}{\|x - \hat{x}\|^2} \right) \quad (11)$$

where  $\|\cdot\|^2$  is the  $\ell_2$  -norm distance between two images and the SSIM of the image is given by:

$$SSIM(x, \hat{x}) = \frac{(2\mu_x \mu_{\hat{x}} + C_1)(2\sigma_{x\hat{x}} + C_2)}{(\mu_x^2 + \mu_{\hat{x}}^2 + C_1)(\sigma_x^2 + \sigma_{\hat{x}}^2 + C_2)} \quad (12)$$

where  $\mu_x, \mu_{\hat{x}}$  are the means and  $\sigma_x^2, \sigma_{\hat{x}}^2$  are the variances of the images  $x$  and  $\hat{x}$ , respectively, and  $\sigma_{x\hat{x}}$  is the covariance of the images. Here, the constant parameters  $C_1$  and  $C_2$  are inserted to stabilize the result in the case that one of the denominator operands is very close to zero.

PSNR metric is merely used for compatibility. SSIM is proven to better represent the image quality [19]. For this reason, we only consider SSIM metric in experimental studies.

## RESULTS AND DISCUSSION

For benchmarking purposes, we utilize nine well-known images of size 256-by-256 and 512-by-512 pixels from



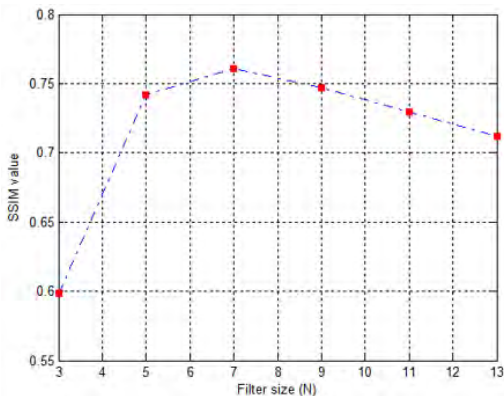
**Figure 2.** Montage of benchmarking images used in the experiments. From left to right and top to bottom: (a) Lena (b) Goldhill (c) Boats (d) Mandrill (e) Cameraman (f) Barbara (g) House (h) Livingroom (i) Pirate.

image set as shown in Fig.2. Images were chosen to represent a categorical set, i.e., human, nature, and textural. AWGN is added to reference images ranging from standard deviation (std)  $\sigma=5$  to  $\sigma=100$  with increments of 5 std units.

## Robustness

### Wiener Filter

In wiener filtering, for a moderate noise level  $\sigma = 25$ , the images were filtered by a  $N \times N$  kernel ranging from 3 to 13. The results are given in Fig.3. As it can be observed, the optimal wiener filter size was found as  $7 \times 7$ .



**Figure 3.** Filter size vs. SSIM value in Wiener filtering.

By increasing noise standard deviation  $\sigma = 5$  to  $\sigma = 100$  with 5 units, we denoised the images and superimposed the all results as shown in Fig. 4. It is seen that SSIM value is around 0.73 in  $\sigma = 5$  case and decreases monotonically towards 0.35 when  $\sigma$  is increased up to 100. It is evident that Wiener filtering is not robust to noise.

### Wavelet Hard Threshold

We set up the threshold level to its default value  $\text{thr} = 0.1$  and choose a base level of decomposition  $L = 1$ . The obtained SSIM values for haar wavelet, dual-tree wavelet and double density dual-tree complex wavelet (ddtcwt) [20,21] are 0.289649, 0.320354, and 0.589060, respectively.

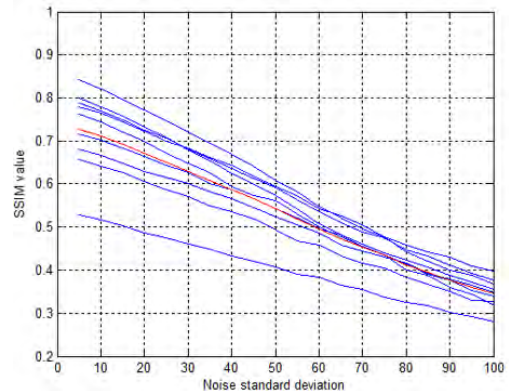


**Figure 4.** Robustness of Wiener filter (Average is denoted by red curve).

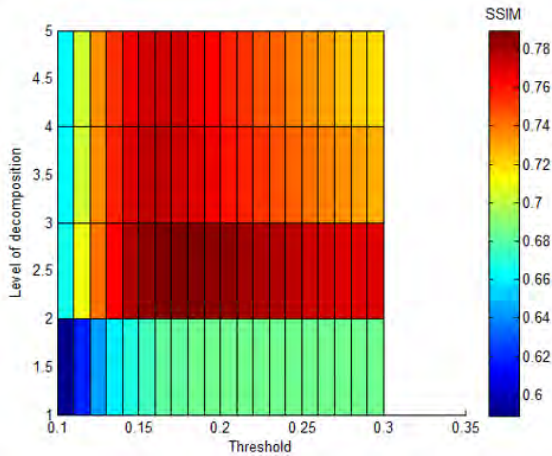


**Figure 5.** Heat map for optimum values of threshold and level of decomposition for wavelet hard thresholding.

ddtcwt improves the image quality tremendously compared with haar and dual-tree wavelets. Concurrently, we measure the computational burdens of the wavelet types. The average run-time performances are 0.077567, 0.123712, and 0.359911 seconds, respectively. As one would expect, ddtcwt comes with extra computational time which is nearly five times haar wavelet to offer this improved image quality. By setting the wavelet type to ddtcwt, we increase the threshold level from its default value 0.1 with increments 0.01 up to 0.3 and  $L = 1$  to  $L=5$ . The more level of decomposition bring out much computational burden. We searched for the optimum values of these parameters and we give the heat map obtained in Fig. 5. It is interesting to note that better SSIM scores are obtained at  $L=2$ . The figure demonstrates that as the level of decomposition increases, less peak SSIM scores are obtained. The performance of the algorithm decreases after the decomposition level 2 and saturates after the decomposition level 4. The best SSIM score was achieved at the threshold 0.16 and decomposition level 2 which is 0.7896.

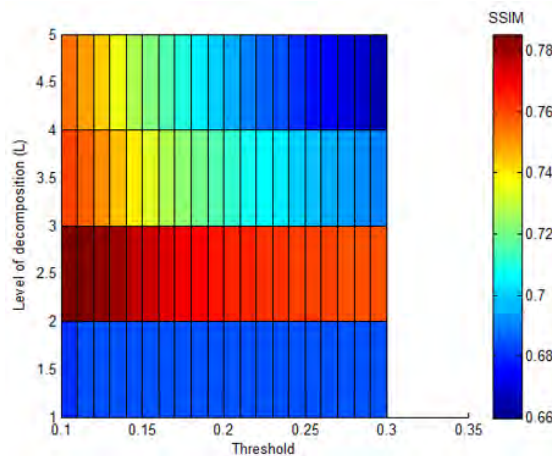


**Figure 6.** Heat map for optimum values of threshold and level of decomposition for wavelet soft thresholding.

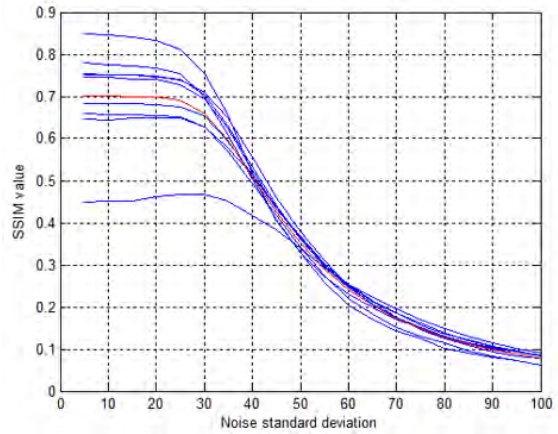


**Figure 7.** Robustness of wavelet hard thresholding.

### Wavelet Soft Threshold

The same procedure was applied for wavelet soft thresholding method. We give the heat map in Fig. 6. As in hard thresholding case, better SSIM scores are obtained at  $L=2$ . As the figure demonstrates the performance of the algorithm decreases sharper than hard thresholding after the decomposition level 2. The best SSIM score was achieved at the threshold 0.10 and decomposition level 2 which is 0.7854.

By increasing noise standard deviation  $\sigma = 5$  to  $\sigma = 100$  with 5 units, we denoised the images and superimposed the results of hard and soft thresholding together as shown in Fig. 7 and Fig. 8. Up to around  $\sigma = 30$ , the image qualities of both methods are comparable. After  $\sigma = 30$ , the performances of both methods decrease sharply though soft thresholding gets better SSIM scores. After  $\sigma = 50$  for hard thresholding and  $\sigma = 60$  for soft thresholding, it is seen that the image qualities of both methods becomes worse than Wiener filtering.

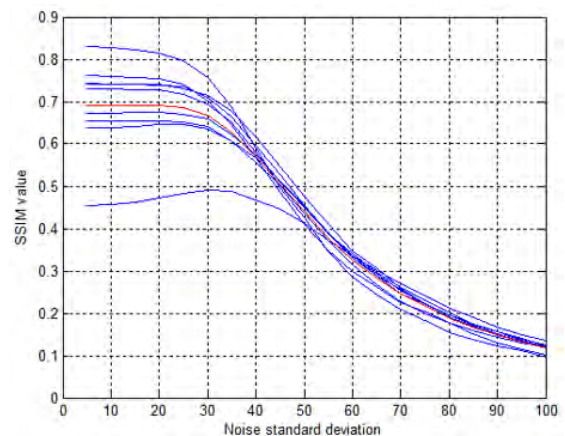


**Figure 8.** Robustness of wavelet soft thresholding.

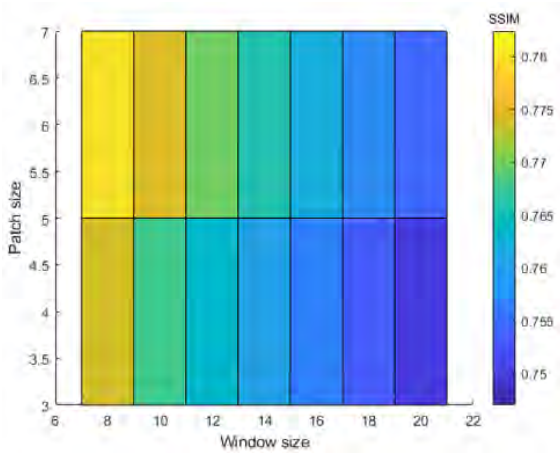


Figure 9. Heat map for optimum values of window size and patch size.

### NLM

In NLM method, as aforementioned two windows are used: patch window and search window. Patch window indicates the neighborhood of the corresponding pixel for weight computations. On the other hand, search window indicates the area wherein similar patches will be searched. In original NLM algorithm, a patch window of the size 7x7 and a search window of the size 21x21 are chosen. But, the search paradigm and suggested values are not suitable for real-world image denoising operations. The original algorithm lasts in time amounts of tens of seconds not milliseconds to complete the denoising task. So, in this study, we preferred to use fast NLM approach [22,23]. The degree of filtering  $h$  used in weight computation was chosen as  $10 * \sigma$  as suggested. As the size of search window increases, the method brings out more computational burden. By varying the patch size in the range 3 to 7 and the window size in the range 7 to 21, we searched for the optimum values of these parameters and obtained the heat map presented in Fig. 9. The figure shows that with a fixed patch size as the window size inc-

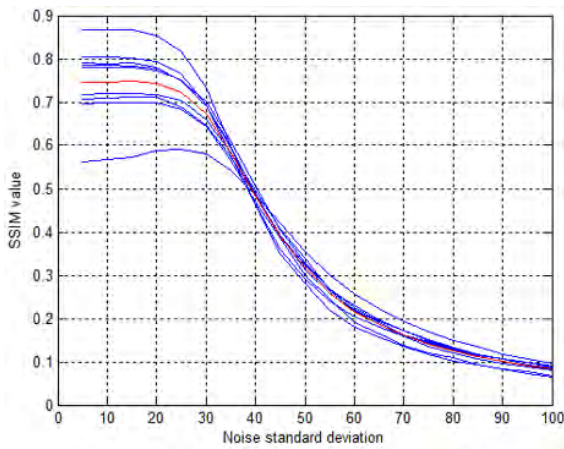


Figure 10. Robustness of the NLM.

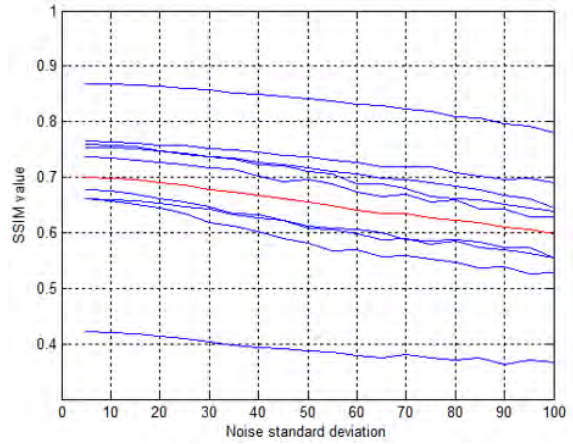


Figure 11. Robustness curve of BM3D.

reases the SSIM scores slightly decreases. Also, with a fixed window size as the patch size increases the SSIM scores slightly increases. Thus, we obtained the best SSIM score with a patch and window size of 7, which is 0.7824.

Fig.10 shows the robustness curve of NLM method. After  $\sigma = 25$ , the performance of the method decreases evidently.

### BM3D

It is a well-known fact in very low SNR values, the performance of the BM3D method in terms of image quality deteriorates sharply. There is a quality/complexity trade-off profile selection key in the implementation of the method [24]. Thus, when implementing the BM3D method, we have selected normal profile for balanced quality/complexity. Fig. 11 shows the robustness curve of the method. Although it is observed that the performance decreases slowly, the method is also more robust against noise interference than the prior methods.

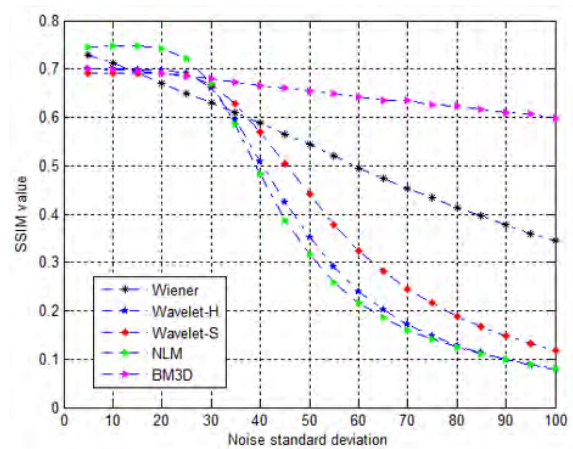


Figure 12. Average robustness of the methods.



**Figure 13.** Denoised Lena images ( $\sigma = 20$ ) (a) Original Lena image (b) Noisy (c) Wiener (d) Wavelet soft thresholding (e) NLM (f) BM3D.



**Figure 14.** Denoised Lena images ( $\sigma = 50$ ) (a) Original Lena image (b) Noisy (c) Wiener (d) Wavelet soft thresholding (e) NLM (f) BM3D.

### Denoised Image Quality

Fig. 12 shows the robustness of the methods together averaged over the benchmarking images. As it is observed, BM3D is the most robust method against noise interference. But, at moderate noise levels up to  $\sigma = 30$ , NLM is more robust than BM3D. Moreover, at low noise levels up to  $\sigma = 15$ , Wiener filter performs better BM3D. After  $\sigma = 30$ , the performances of four methods other than BM3D

decrease more sharply. It is also interesting to note that Wiener filter performs better than wavelet and NLM methods at moderate and high noise levels after  $\sigma = 35$ .

Fig. 13 and Fig.14 show denoised sample 'Lena' images by Wiener, Wavelet soft thresholding, NLM, and BM3D methods in  $\sigma = 20$  (low-moderate levels of noise) and  $\sigma = 50$  (moderate-high levels of noise) cases, respectively.

**Table 1.** DIQ scores of the methods.

Wiener	Wavelet H	Wavelet S	NLM	BM3D
0.5327	0.3795	0.4230	0.3811	0.6523

Average denoised image quality for each method is calculated by averaging the SSIM values obtained at each  $\sigma$  value of noise interference in the robustness curves over the  $N$  benchmarking images. Let the  $SSIM_{\sigma}^i$  denote the SSIM value of the  $i$ th image in the dataset obtained at the  $\sigma$  standard deviation of noise interference. Then the average denoised image quality,  $DIQ$  is given as:

$$DIQ_{Method} = \frac{1}{N} \sum_{i=1}^N \sum_{\sigma=1}^{\sigma=20} SSIM_{5\sigma}^i / 20 \quad (13)$$

Table 1 shows DIQ scores of the methods. As one would expect, although soft thresholding gets more high denoising score, the performances of both wavelet thresholding methods are quite similar. The denoising score of Wiener filter is remarkable which is higher than the remaining three methods except BM3D.

### Computation Time

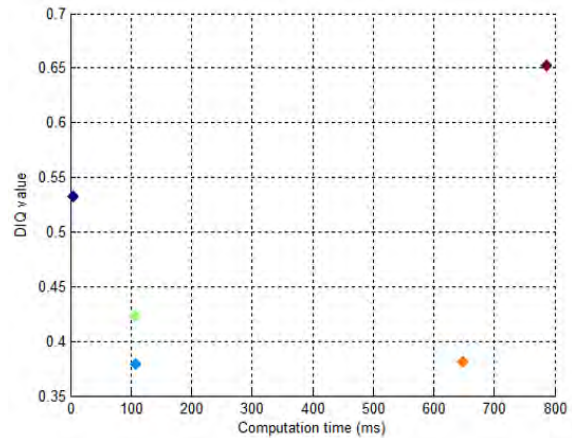
For a sample image, Table 2 gives the computation times of sizes 256x256 and 512 x512 or when the size is doubled. Experiments were carried out in MATLAB R2018 environment on an Intel Core i5-6200U CPU @ 2.3 GHz computer with 8 GB RAM. The experiments were repeated a hundred times and averaged. If the first case is examined, it can be deduced that Wiener filter is approximately 20x (20 times) faster than Wavelet-based methods, 120x faster than NLM method, and 150x faster than BM3D method. It is observed that NLM and BM3D methods are quite slow with respect to Wiener filter and Wavelet-based methods.

In the second case, when the image size is doubled, this would ideally give 4x extra computational burden. From the computation times it can be deduced that Wiener, Wavelet, and BM3D methods keep their computational burdens in this case. But, NLM cannot keep its computational burden in which case yields 6x extra computational burden.

Fig. 15 shows the DIQ values versus computation times of the respective methods for images of the size 256x256. Optimal algorithms are supposed to have less computational times and at the same time high DIQ scores. According

**Table 2.** Average computational burdens of the methods (in terms of seconds)

Image size	Wiener	Wavelet H	Wavelet S	NLM	BM3D
256x256	0.0052	0.1081	0.1051	0.6479	0.7863
512x512	0.0181	0.4479	0.4027	3.7751	3.3097

**Figure 15.** DIQ values versus computation times of the corresponding methods.

to the figure, Wiener filter satisfies this criterion as much as possible. In this respect, it is observed that NLM is far away from satisfying this criterion.

### CONCLUSION

In time-constrained blind image denoising operations, both image quality and computational burden are important factors. Also, denoising algorithms must be robust to varying noise interference. Due to this, an optimal performance is desired. In this study, we have derived the robustness, image quality, and computational time efficiencies of the image denoising algorithms employed for these goals. From the experimental works, we can conclude that up to moderate noise levels, i.e.  $\sigma = 30$ , NLM is superior to other denoising algorithms, namely, Wiener, Wavelet-based and BMD methods. At high noise levels, especially higher than  $\sigma = 50$ , BM3D performs best in terms of image quality. It is interesting to note that Wiener filter also performs better from Wavelet-based and NLM methods in high noise levels. When the computation times are considered, Wiener filter is far away efficient from the other algorithms. Especially, NLM and BM3D methods are approximately 120x ~ 150x slower than the Wiener filter. We can deduce that under low-moderate noise levels, if the image quality is more important than the computation time NLM can be chosen. Under moderate-high noise levels, if the same goals are required, BM3D is the selection. But, for optimality, Wiener filter is the figure of merit and is considered to satisfy both criteria as much as possible.

### CONFLICT OF INTEREST

The authors declare that they have no known competing financial interests or personal relationships that could have appeared to influence the work reported in this paper.

---

## References

---

1. Yaroslavsky L. Digital Picture Processing. Berlin, Germany: Springer Verlag; 1987.
2. Gonzalez RC, Woods J. Digital Image Processing, 3rd ed. Englewood Cliffs, NJ: Prentice-Hall; 2008.
3. Perona P, Malik J. Scale-space and edge detection using anisotropic diffusion. *IEEE Transactions on pattern analysis and machine intelligence*. 1990; 12(7): 629-639.
4. Rudin LI, Osher S, Fatemi, E. Nonlinear total variation based noise removal algorithms. *Physica D: nonlinear phenomena*, 1992; 60(1-4):259-268.
5. Donoho DL, Johnstone IM. Ideal spatial adaptation by wavelet shrinkage. *Biometrika*, 1994; 81(3): 425-455.
6. Donoho, DL. De-noising by soft-thresholding. *IEEE transactions on information theory*, 1995; 41(3): 613-627.
7. Chang SG, Yu B, Vetterli M. Adaptive wavelet thresholding for image denoising and compression. *IEEE transactions on image processing*, 2000; 9(9): 1532-1546.
8. Pizurica A, Philips W, Lemahieu I, Acheroy M. A joint inter-and intrascale statistical model for Bayesian wavelet based image denoising. *IEEE Transactions on Image Processing*, 2002; 11(5): 545-557.
9. Buades A, Coll B, Morel JM. A non-local algorithm for image denoising. In: 2005 IEEE computer society conference on computer vision and pattern recognition (CVPR'05). 2005 Jun; IEEE: 2; 60-65.
10. Buades A, Coll B, Morel JM. A review of image denoising algorithms, with a new one. *Multiscale modeling & simulation*, 2005; 4(2): 490-530.
11. Dabov K, Foi A, Katkovnik V, Egiazarian K. Image denoising by sparse 3-D transform-domain collaborative filtering. *IEEE Transactions on image processing*, 2007; 16(8): 2080-2095.
12. Zhang K, Zuo W, Chen Y, Meng D, Zhang L. Beyond a gaussian denoiser: Residual learning of deep cnn for image denoising. *IEEE transactions on image processing*, 2017; 26(7): 3142-3155.
13. Goyal B, Dogra A, Agrawal S, Sohi BS, Sharma A. Image denoising review: From classical to state-of-the-art approaches. *Information fusion*, 2020; 55: 220-244.
14. Bozkurt F, Yaganoglu M, Günay FB. Effective Gaussian blurring process on graphics processing unit with CUDA. *International Journal of Machine Learning and Computing*, 2015; 5(1): 57.
15. Tomasi C, Manduchi R. Bilateral filtering for gray and color images. In: Sixth international conference on computer vision. 1998 Jan; IEEE: 839-846.
16. Elad M. On the origin of the bilateral filter and ways to improve it. *IEEE Transactions on image processing*, 2002; 11(10): 1141-1151.
17. Singer A, Shkolnisky Y, Nadler B. Diffusion interpretation of nonlocal neighborhood filters for signal denoising. *SIAM Journal on Imaging Sciences*, 2009; 2(1): 118-139.
18. Wang Z, Bovik AC, Sheikh HR, Simoncelli EP. Image quality assessment: from error visibility to structural similarity. *IEEE transactions on image processing*, 2004; 13(4): 600-612.
19. Wang Z, Bovik AC. Mean squared error: Love it or leave it? A new look at signal fidelity measures. *IEEE signal processing magazine*, 2009; 26(1): 98-117.
20. Sendur L, Selesnick IW. Bivariate shrinkage functions for wavelet-based denoising exploiting interscale dependency. *IEEE Transactions on signal processing*, 2002; 50(11): 2744-2756.
21. Selesnick I. Wavelet Software at Brooklyn Poly [Internet]. Electrical Engineering: Polytechnic University of New York; [cited: 2023 May 25]. Available from: <https://eeweb.engineering.nyu.edu/iselesni/WaveletSoftware/dt2D.html>
22. Darbon J, Cunha A, Chan TF, Osher S, Jensen, GJ. Fast nonlocal filtering applied to electron cryomicroscopy. In: 2008 5th IEEE International Symposium on biomedical imaging: from nano to macro. 2008 May; IEEE: 1331-1334.
23. Wu Y. (2023). Fast Non-Local Mean Image Denoising Implementation [Internet]. MATLAB Central File Exchange: Mathworks; 2012 [updated: 2012 Sep 18; cited: 2023 May 25]. Available from: <https://www.mathworks.com/matlabcentral/fileexchange/38200-fast-non-local-mean-image-denoising-implementation>
24. Foi A. Image and video denoising by sparse 3D transform-domain collaborative filtering [Internet]. Department of Signal Processing: Tampere University of Technology; [cited: 2023 May 25]. Available from: <https://webpages.tuni.fi/foi/GCF-BM3D/index.html>





# Simultaneous Effect of Welding Current with Post-Weld T6 Heat Treatment on Corrosion Susceptibility of Al6013 Alloy Joined by GTAW

Mehmet Topuz 

Van Yuzuncu Yil University, Department of Mechanical Engineering, Van, Türkiye

## ABSTRACT

Al6013 base metals were joined successfully with ER4047 filler metal by using the GTAW method under different welding currents. Post-weld T6 heat treatment effects on corrosion properties were investigated in terms of open circuit potential (OCP), potentiodynamic polarization (PDS), and electrochemical impedance spectroscopy (EIS) tests. It was determined that corrosion resistance of the post-weld samples increased with increasing welding current, while T6 heat treatment only effective on 110A and 140A welding current samples (3.61 to 2.08, 2.95 to 2.40, and 1.38 to 2.15  $\mu\text{A}\cdot\text{cm}^{-2}$  for 110A, 140A, and 170A welding current before and after T6 heat treatment). The characteristics of the oxide films on the surfaces are revealed with EIS analysis. While the passive film originating from Al is generated on the surfaces, the two-constant equivalent circuit model found that as it also contains pittings on the surface. It was determined that the pitting resistance of the T6 heat treated 110A sample increased (3075 to 4562  $\Omega$ ). Post-corrosion SEM surface morphologies showed that low welding currents lead to more destruction as increased exposure to corrosion.

## Keywords:

Al6013, GTAW, Weld current, T6 heat treatment, Corrosion

## INTRODUCTION

Aluminium (Al), which second-largest subterranean reserve in the world, can exhibit different physical and mechanical properties as a result of various alloying and different heat treatment processes [1]. Because of the low density, simplicity in shaping, high corrosion resistance, and adaptable physical and mechanical properties of Al alloys, application fields are increasing day by day. These fields are in various fields such as the manufacturing industry, agriculture, energy, construction, and especially transportation [2]. The density value of Al is about 2.7  $\text{g}\cdot\text{cm}^{-3}$ , and it is about one-third of the density of steel (7.83  $\text{g}\cdot\text{cm}^{-3}$ ) and copper (8.93  $\text{g}\cdot\text{cm}^{-3}$ ), so it is favourable for weight reducing for vehicles such as airplanes or many others. As a result of the weight reduction due to its low density, it also contributes to the reduction of carbon emission in the aviation field so they have a significant place in the aerospace industries [3,4].

Today, there are numerous Al alloys developed for industrial applications [5]. High mechanical properties can be attained in such a vast number of Al alloys, particularly for alloys that can be heat treated following

the age hardening procedure. 2XXX (Al-Cu), 6XXX (Al-Mg-Si), and 7XXX (Al-Zn-Mg) series Al alloys are favourable among these Al alloys for obtaining high mechanical properties after the aging process [6,7]. As a result of secondary aging heat treatment (T4: natural aging or T6: artificial aging) processes to be applied to these alloys, the strength of these Al alloys can be increased with a precipitation hardening mechanism [8,9]. This principle was discovered independently in 1938 by Guinier and Preston. It is based on the homogeneous dissolution of elements such as Cu, Mg, and Si in the alloy during solid solution and forming a precipitate with quenching [10]. Among these Al alloys, the 6XXX series, which is frequently used in the aerospace industry, stands out due to its relatively high specific strength as well as good formability, weldability, and corrosion resistance. Despite the mentioned benefits, the corrosion resistance of 6XXX alloys may decrease due to the alloying elements which increased impurity (percent decrease in the amount of Al). Therefore, studies on the development of 6XXX series Al alloy based on the investigation of heat treatment parameters have gained momentum [11]. 6XXX series alloys comprise Mg and

## Article History:

Received: 2023/06/12

Accepted: 2023/07/31

Online: 2023/09/30

Correspondence to: Mehmet Topuz,

E-mail: mehmettopuz@yyu.edu.tr;

Phone: +90 506 674 3546;

Fax: +90 432 225 1730

This article has been checked for similarity.



This is an open access article under the CC-BY-NC licence

<http://creativecommons.org/licenses/by-nc/4.0/>

## Cite as:

Topuz M, "Simultaneous Effect of Welding Current with Post-Weld T6 Heat Treatment on Corrosion Susceptibility of Al6013 Alloy Joined by GTAW" Hittite Journal of Science and Engineering, 10(3):269–277, 2023. doi:10.17350/hjse19030000316

Si that will form magnesium silicide ( $Mg_2Si$ ) in their microstructure so precipitation hardening was favourable with heat treatment. The amount and size of  $Mg_2Si$  particles can vary depending on the temperature and time during the heat treatment [10]. When the T6 heat treatment is applied to the alloys in this group, the strength of the alloys can be increased remarkably. In addition to these two elements, 6XXX series may contain small amounts of Copper (Cu), Manganese (Mn), and other elements [12]. By adding Manganese (Mn) and Chromium (Cr) to many of the 6XXX series aluminium alloys, an increase in elastic limits and grain size control can be achieved. As a result, the relatively new alloy Al6013 has a higher Cu content than other 6XXX series, which improves its strength as a result of its secondary hardening mechanism [8]. Due to its high Cu concentration it tends to form precipitation-free zones (PFZ) at grain boundaries during precipitation hardening, which makes highly susceptible to intergranular corrosion the Al6013 alloy [13]. Al6013-T6 alloy has been popular in the aerospace, particularly because of its enhanced weldability and high resistance to corrosion [7].

Al6013-T6 alloy has good corrosion resistance during contact with different corrosive environments (air, water, oils, etc.) and against many other chemicals like all Al and its alloys [14]. Due to the high affinity of Al for oxygen, the thin and dense oxide layer ( $Al_2O_3$ ) formed on the surface as a result of contact with the atmosphere provides resistance against corrosive effects. This feature of aluminium provides higher corrosion resistance as well as expanded its application area. The ability of aluminium to resist corrosion is directly related to its purity. In other words, other elements such as Mg, Si, Cu, etc., may be responsible for diminished corrosion resistance [15]. Therefore, it is necessary to investigate the corrosion behaviour of Al and its alloys in all processes.

In various applications, the use of welding, which creates joins of the same and/or different metals, becomes necessary [2,16]. Especially in industries such as aviation, it is important to joints multiple small and complex parts. Among various welding methods Gas Tungsten Arc Welding (GTAW) was mostly used because of applicable of wide range of applications. In GTAW method, a tungsten electrode carried by a suitable torch creates an arc with the base metal. High amount of heat was released as a result of this arc followed by base metal and filler metal melting [15]. The advantages of GTAW welding can be listed as follows; i) it can be applied with both manual and automatic welding systems, ii) it can be used by melting the base metal or melting an additional filler metal, iii) suitable for welding thin materials, iv) high penetration and non-porous joining can be made, v) the deformation of the workpiece is less since the heat input is concentrated on the weld zone, and vi) it

gives a smooth weld seam [2,15]. The shielding gas sent to the welding area through the hood. Thus, possible welding faults are prevented by protecting the area. The shielding gas has a great influence on the stability of the arc and the quality of the weld [17].

There are various studies on the corrosion susceptibility of 6XXX series Al alloys. In the study conducted by Abo Zeid [18], the highest corrosion resistance was determined in the Al6013-T6 alloy. It was also stated that the  $Mg_2Si$  particles precipitated in the 6XXX series increased the corrosion resistance, especially the pitting corrosion. On the other hand, Lei et al. [13] have researched that T6 heat treatment parameters and the effect of different continuous heating at 20, 30, 40, 60, and 80 °C.min<sup>-1</sup> on the microstructure, mechanical and corrosion properties of Al6013 alloy after 30 minutes of solution at 570 °C. However, with increasing final heat treatment temperature changes (140, 190, 220, and 240 °C) at a constant aging rate of 60 °C.min<sup>-1</sup>, it was determined that the intergranular corrosion depth decreased with increasing final heat treatment temperature. By this way, it has been predicted that the T6 heat treatment of the Al6013 alloy can inhibit corrosion, especially by reducing the intergranular corrosion mechanism with continuous heating. Furthermore, observation of intergranular corrosion at the cross-section of alloy has been proven together with the corrosion current density ( $I_{corr}$ ) values and it has been revealed that maximum corrosion protection is obtained with continuous heating at 60 °C.min<sup>-1</sup>.

Al6013 alloy is a relatively new alloy specially designed for the aerospace industry, which was developed to increase the low yield and tensile stresses of the Al6061 alloy and to have similar mass properties [19]. However, compared to Al6061 alloy, its weldability remains low due to the insufficient Al proportion. According to the previous studies, the effect of welding current and post-weld T6 heat treatment was not investigated in terms of Al6013 alloy joined with the GTAW process. As a research hypothesis, corrosion susceptibilities can resemble those achieved with high welding current when T6 heat treatment is applied to an Al6013 alloy joint with low welding current strength. To put forward this hypothesis, Al6013 plates were joined by GTAW using ER4047 (AlSi12) alloy as filler metal, and after being characterized, corrosive properties were investigated in detail.

## MATERIAL AND METHODS

### Materials and GTAW Process

The extruded Al6013 alloy was supplied with the dimensions of 200×60×5 mm from Simitçioğlu Metal. AlSi12 (ER4047) alloy with a diameter of 3 mm was used as the filler metal (Blueweld GTAW AlSi12, Vega Makina). ER4047 alloy chosen for its advantages such as good flu-

idity, low melting point, enhanced corrosion resistance, and prevention of welding distortion after process. The chemical compositions of the Al6013 and ER4047 used along with the study were presented in Table 1. For the welding process, the parts to be welded were chamfered at 45 degrees and a pool was formed for the weld seam. Thus, two single v-grooves (Fig. 1a) were welded [5], and the effect of T6 heat treatment on welded plates was investigated. Zenweld Ultimate AC/DC 315 welding machine was used in GTAW processes, and welding currents were preferred as 110A, 140A, and 170A (A: Amperes), respectively. These currents were determined from detailed literature research for evaluating low, medium, and high welding current on welding process [2,20]. In addition, according to previous [1,17,20,21] and preliminary studies, other parameters were fixed as welding speed: 160 to 180 mm.min<sup>-1</sup>, wire speed: 6 mm.min<sup>-1</sup>, voltage: 20 V, and gas flow: 12 L.min<sup>-1</sup>. During the GTAW of plates, 99.999% high-purity Ar gas was used as shielding gas for a protective atmosphere. The plates after the GTAW process, which were welded in 3 different currents, were cut into two with an abrasive cutter (Micracut 202, Metkon). Solutionizing was carried out at 575 °C for 1 h followed by quenched in ice water, T6 heat treatment was applied in a furnace (MT1120, Magmatherm) at 191 °C for 4 h [22]. After T6 heat treatment, the weld joints were cut into different sizes for further tests and analyses. To better clarification of the post-weld and T6 heat treatment processes in the joints, 110A, 140A, and 170A represents post weld joints while HT-110A, HT-140A, and HT-170A represents T6 heat treated joints after GTAW, respectively.

**Table 1.** Compositions of Al6013 and ER4047 alloys

Material	Composition (wt.%)								
	Si	Ti	Zn	Cu	Fe	Mn	Cr	Mg	Al
Al6013	0.20	0.15	0.25	4.30	0.30	0.60	0.10	1.50	Balance
ER4047	12.00	0.05	0.10	0.05	0.50	0.15	-	0.05	Balance

### Microstructure Analysis

Before electrochemical corrosion tests of the weld zones (WZ: a combination of base metal, heat affected zone: HAZ, and weld seam), were characterized with macro photos. HAZs and weld seams were also characterized by optical microscopy (OM) images. NaOH etching was used for OM micrographs of welded joints. The before and after corrosion tests WZs were characterized by scanning electron microscopy (SEM) images and attached energy dispersive X-ray (EDX) analyses to detect both elemental analyses and the damages in the WZs after electrochemical corrosion tests. For precipitation formation at WZ was determined using X-ray diffraction (XRD, PANalytical Empyrean). XRD analyses were performed with a Cu-K $\alpha$  radiation source at a wavelength of 1.5406 (angle range from 30 to 80 2 $\theta$ ) and a step rate of 0.05.

### Electrochemical Corrosion Tests

The evaluation of the corrosion susceptibilities of WZ was carried out using Gamry PCI14/750 device following ASTM G59 standards [23]. Electrochemical corrosion tests were performed using the three-electrode method, Ag/AgCl and platinum were used as reference electrodes and counter electrode, respectively, while WZ was used as working electrodes. 3.5 by wt.% NaCl was used as the electrolyte and the WZ which was in contact with the electrolyte was fixed at 2 cm<sup>2</sup> and masked by cold moulding. The potential ( $E_{ocp}$ ) changes were recorded in the electrolyte for 3600 s for the samples to reach the equilibrium state (open circuit potential: OCP). Then, the samples that reached the equilibrium state were polarized to  $\sim -0.15V$  vs.  $E_{ocp}$  starting from  $-0.3 V$  vs.  $E_{ocp}$  cathodic overpotential using 1 mV.s<sup>-1</sup> scanning rate with potentiodynamic scanning (PDS) method. Electrochemical impedance spectroscopy (EIS) measurements [24], especially for the oxide film forming ability of the WZ and the corrosion mechanism, are used with AC amplitude of 10 mV over OCP in the frequency range from 100 kHz to 0.01 Hz after PDS tests. Fittings of EIS data were calculated with EC-Lab (Demo version) software through the Randomize+Simplex method under 10000 iterations for Randomize and 5000 iterations for Simplex until a minimum chi-square ( $\chi^2$ ) value was obtained. All tests were repeated 3 times and their reproducibility was revealed. Afterward, the samples were ultrasonically cleaned and stored in a desiccator until post-corrosion SEM surface morphology observations.

### RESULTS AND DISCUSSION

After the GTAW process, macro images taken from the cross sections of the weld joints with 110A, 140A, and 170A, respectively, are presented in Fig. 1. In macro examinations, especially in the weld seam, an increased porosity was determined with increasing welding current (110 to 170A). The first reason for the observation of porosity in the welding process can be the increase in the amount of supersaturated hydrogen in Al as a result of increased welding current [15]. On the other hand, since the obtained macro images were taken after etching in NaOH of the WZs, it is thought that these porosities may have been formed as a result of further etching of the weld seam. Moreover, it is predicted that the increased amount of welding current causes grain growth in the weld seam, so its sensitivity to NaOH etching solution may have increased [5]. Another finding is that in GTAW performed with 110A current, the visible area between base metal and weld seam disappears with increased welding current (Fig. 1a to 1c). It is thought that this may be due to the high Al content in the Al6013 alloy and the high thermal transfer coefficient (239 W.m<sup>-1</sup>.K<sup>-1</sup>) of Al

[25]. As a result of the increased welding current and the high thermal transfer coefficient, the heat transfers from the weld seam to the base metal and increases a homogeneous HAZ formation. It has been observed that this HAZ becomes more visible with increasing welding current (Fig. 1c). On the other hand, after the GTAW process in all different currents, pitting formation was observed especially in the middle of the v-groove (Fig. 1b). This is attributed to heat transfer from ER4047 to Al6013, which causes a partial cooling of the weld seam from the torch until it reaches the v-groove joint [21].

In Fig. 2, OM images of weld seams and HAZs after NaOH etching under different welding currents are presented. As the first striking finding, it is seen that with increased welding current grain size was increased especially in 170A. Moreover, as mentioned in Fig. 1, it is observed that the width of the HAZ increases with increasing current. It can be deduced that the increased welding current increases the width of the HAZ, but it causes an increase in the grain size of the weld seam, which may lead to a decrease in both the strength of the weld seam and more prone to corrosion.

EDX analysis results of WZs are presented in Fig. 3. The excess of Si element in the EDX analysis of the base metal is due to the wt.% 12 Si ratio of Al6013 (Table 1). On the other hand, even though the Cu amount seems low in the EDX analysis with #2, due to the wt.% 92.87 Al ratio of ER4047, it has a count of about 1K and is higher than base metal. The porosities of both base metal and weld seam were observed along with the SEM images and their elemental contents were confirmed by EDX analyses were taken. Another finding from EDX is that possible presence of elements that will form precipitation particles such as  $Al_2Cu$  and  $Mg_2Si$  in base metal and weld seams.

In Fig. 4, XRD analysis performed for determine possible precipitate phases that may occur in the microstructure of WZ before and after T6 heat treatment. As can be seen in Fig. 4a, characteristic Al peaks, which constitute the majority of both base metal and weld seam, were found at approximately 38, 44, 65, and 78  $2\theta$  angles. With the T6 heat treatment, the Al peaks sharpened and the crystallinity of the microstructure increased. On the other hand, after T6 heat treatment,  $Al_2Cu$  precipitation phases were encountered at approximately 30, 37.5, and 51.3  $2\theta$  angles, while  $Mg_2Si$  precipitation phases were encountered at 65.8, 72.4, and 79.1  $2\theta$  angles (Fig. 4b). It is also predicted that these phases can be formed after welding with slow cooling and a long time in atmospheric conditions. Undoubtedly, this microstructural change will greatly affect corrosive properties. As a matter of fact, while the mechanical strength will increase with precipitation formation, the corrosive susceptibilities of the WZ may increase with possible galvanic couple formation.

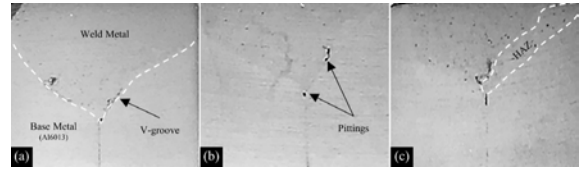


Figure 1. Macroscopic cross-section image of base metal, HAZ, and weld seams (a) 110A, (b) 140A, and (c) 170A

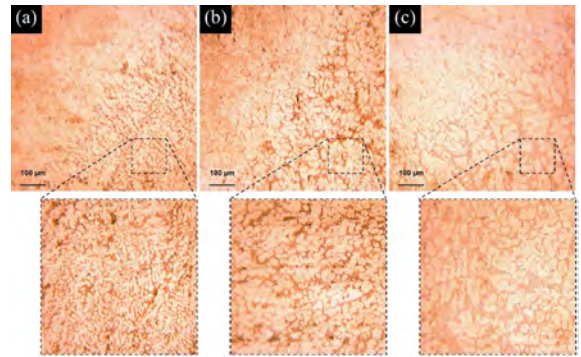


Figure 2. Optical microscopy of weld seams and HAZs, (a) 110A, (b) 140A, and (c) 170A

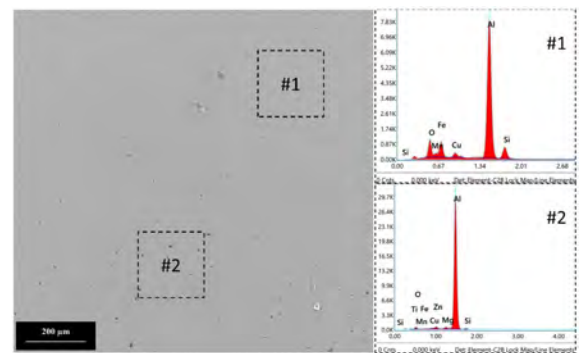


Figure 3. EDX analyses of weld zone which was welded with 170A

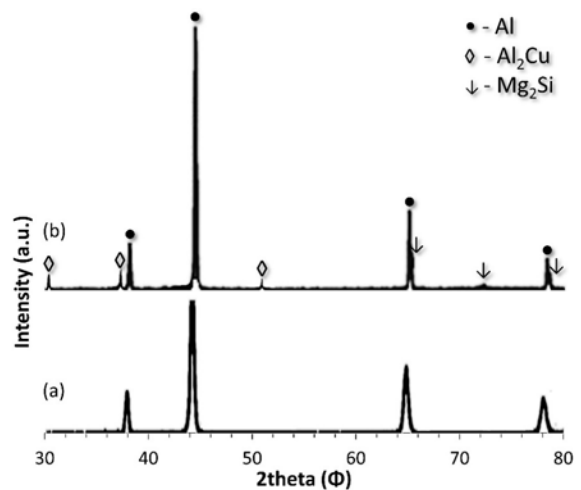
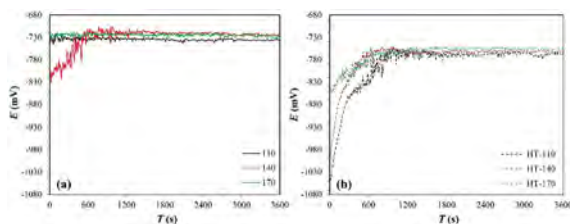


Figure 4. XRD results of 140A weld joints' WZ, (a) before and (b) after T6 heat treatment

The OCP test result of post-weld and T6 heat treated WZ is given in Fig. 5. As can be seen from Fig. 5a, while in the 110A and 170A joins became a steady state in a short time, this situation took about 600 s with the 140A. The size and distribution of the porosities in the weld seams and HAZs as a result of various welding currents are assumed to be the cause of this alteration. On the other hand, Fig. 5b, which shows the OCP change in the WZ after T6 heat treatment, a noble behaviour was observed in all samples up to about 900 s, while it became stable with increased immersion time. Particularly, the size, distribution and shape of the pores on the side of the weld seam are an important factor in the change of the open circuit potential ( $E_{ocp}$ ) values before and after T6 heat treatment. The porosities formed on the surface may cause potential fluctuations along the surface as they form regions where the electrolyte remains stagnant during the increasing immersion time [26]. As a general opinion, it has been observed that the time for all samples to reach the steady state is 1200 s, and it can be said that the corrosion samples have a stable potential behaviour along their surfaces which indicates stable oxide film formation.



**Figure 5.** OCP immersion results of (a) post-weld and (b) T6 heat treated WZs

Fig. 6a and 6b represents PDS curves of post-weld and T6 heat treated WZ in 3.5% NaCl electrolyte after OCP are presented, respectively. In addition to PDS curves, the important corrosion parameters calculated by the Tafel extrapolation method are presented in Table 2. Similar to the  $E_{ocp}$  values, the corrosion potential ( $E_{corr}$ ) values in the PDS curves were observed in approximately the same potential range in all samples (-695 to -173 mV for post-weld and -752 to -755 mV for T6 heat treated). It can be deduced from the PDS curves corrosion current density ( $I_{corr}$ ) of 170A ( $1.38 \mu\text{A}\cdot\text{cm}^{-2}$ ) was lower than the 110A and 140A samples ( $3.61$  and  $2.95 \mu\text{A}\cdot\text{cm}^{-2}$ , respectively). As a matter of fact, since the  $I_{corr}$  value represents the amount of current passed per unit surface area in electrochemical tests, the decrease of this current means higher corrosion resistance or lower susceptibility of the sample [2,13]. On the other hand, the  $I_{corr}$  values of the HT-170A were increased ( $2.15 \mu\text{A}\cdot\text{cm}^{-2}$ ) after T6 heat treated WZ, while there was a decrease of HT-110A and HT-140A ( $2.08$  and  $2.40 \mu\text{A}\cdot\text{cm}^{-2}$ , respectively). In other words, a decrease in  $I_{corr}$  values, i.e. increased corrosion resistance, was observed with the increasing welding current.

However, after T6 heat treatment, the corrosion behaviour of all samples showed similar behaviour. An increase in corrosion resistance occurred in the HT-110A sample. It is thought that this behaviour may have occurred as a result of the formation of porosity at the weld seams. This can be explained by porosity-precipitation relationship. Indeed, this situation can be explained as follows; decrease in  $I_{corr}$  of HT-110A was grain size and precipitation effect on grain boundaries [8,18]. As Çomaklı [27] mentioned, grain boundaries act as a physical corrosion barrier for coatings but uncoated samples used in present research behave differently due to the precipitations located in grain boundaries after T6 heat treatment. Furthermore, protective efficiency P (%) of the coating was described also with an equation:  $P (\%) = [1 - (I_{corr} / I_{corr}^0)] \times 100$  where  $I_{corr}$  and  $I_{corr}^0$  represent coating and substrate, respectively. But in this study, these parameters are specified as T6 heat treated and post-weld, respectively. In this way, 110A, 140A, and 170A P values were calculated as, 42.38%, 18.64%, and -55.79% respectively. So, it means that for 110A and 140A samples, T6 heat treatment was effective for corrosion protection while for 170A samples not. Moreover, calculated  $I_{corr}$  values are inversely proportional to the polarization resistance ( $R_p: \Omega\cdot\text{cm}^2$ ) values, and decreasing  $I_{corr}$  values indicate an increasing  $R_p$  value (Table 2). On the other hand, decreasing  $I_{corr}$  values change in direct proportion to the corrosion rate (*corr. rate*:  $\mu\text{mpy}$ ) calculated by considering the homogeneous corrosion mechanism on the surface. In short, the increased corrosion resistance as a result of the decreasing  $I_{corr}$  value also decreases the *corr. rate* value and shows the homogeneous corrosion rate in  $\mu\text{mpy}$  unit that will degrade as a result of corrosion from the surface homogeneously [28].

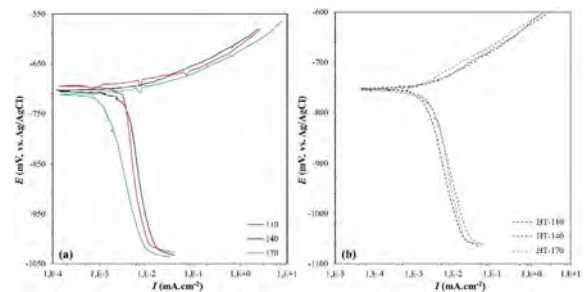


**Figure 6.** PDS curves of (a) post-weld and (b) T6 heat treated WZs

**Table 2.** Important corrosion parameters calculated from PDS curves according to Tafel extrapolation method

Samples	$E_{corr}$ (mV)	$I_{corr}$ ( $\mu\text{A}\cdot\text{cm}^{-2}$ )	$\theta_a$ (V/decade)	$\theta_c$ (V/decade)	$R_p$	<i>corr.rate</i> ( $\mu\text{mpy}$ )
110A	-704	3.61	0.04	0.61	4312	41.31
140A	-695	2.95	0.05	0.66	3078	25.97
170A	-713	1.38	0.03	0.40	8403	10.54
HT-110A	-753	2.08	0.05	0.36	9165	13.20
HT-140A	-752	2.40	0.05	0.30	7754	24.54
HT-170A	-755	2.15	0.05	0.29	8613	18.26

In Fig. 7, the EIS analysis results of the post-weld and T6 heat treated WZs are presented. Nyquist curves obtained from EIS analyses are evaluated as a measure of the stability of the oxide film on the samples in the electrolyte. From this point of view, the results of Nyquist curves are in parallel with the  $I_{corr}$  values obtained by the Tafel extrapolation method from the PDS curves given in Fig. 6 and given in Table 2. In post-weld joints, the highest Zreal ( $\Omega \cdot \text{cm}^2$ ) vs Zimag ( $\Omega \cdot \text{cm}^2$ ) radius and thus the most stable oxide film characteristic and corrosion resistance were obtained with the 170A (Fig. 7a) [29]. Again, similar to the PDS curves, it was determined that HT-110A was more resistant to corrosion. However, unlike the PDS curves, it is observed that there is a greater increase in the Nyquist radii of the HT-110A, especially as the oxide film stability (Fig. 7c). As seen in Figs. 7a and 7c, it is thought that a flattening semi-circle curve in the Nyquist diagrams may have resulted from a possible capacitance behaviour [30]. Furthermore, due to various reasons such as surface homogeneity, roughness, porosity, and composition difference of the working electrode (WZs), the ideal capacitance behaviour can act as a constant phase element (CPE) [30]. On the other hand, it is seen in the bode diagrams given in Figs. 7b and 7d that both Freq (Hz) vs Zmod ( $\Omega \cdot \text{cm}^2$ ) and Freq (Hz) vs Zph ( $^\circ$ ) values diverge in the positive direction after T6 heat treatment. In order to determine the mechanism that triggers the oxide film formation and interactions between electrolyte, Nyquist curves should be investigated in terms of electrochemical circuit model.

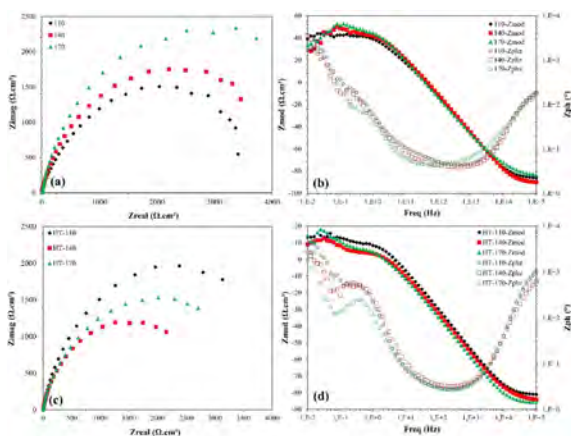


**Figure 7.** Non-destructive EIS results of (a) and (c) Nyquist diagram with (b) and (d) Bode-plots of WZs

In Fig. 8, the data fitting through the EC-Lab demo software using the data in the Nyquist diagrams presented in Figs. 7a and 7c, and the recommended equivalent circuit diagram are presented. The simulated fitting values are presented in Table 3. All results were well-fitted with the proposed two-constant equivalent circuit model [27]. Electrical components in the equivalent circuit are,  $R_e$ : resistance of the electrolyte,  $Q_p$ : constant phase element (CPE) of the

passive film,  $R_p$ : resistance of the passive film,  $Q_{pit}$ : constant phase element of pittings, and  $R_{pit}$ : polarization resistance of associated with pits represent pits [24]. The Nyquist curves have presence of an element showing capacitive behaviour in the corrosion mechanism. However, this circuit element, which should show capacitive behaviour due to different reasons such as reactivity of surface, microstructural heterogeneity, roughness, and porosity on the weld seams, can act as a constant phase element (Q) [30]. The impedance of CPE is given by  $Z_{CPE} = Q^{-1}(j\omega)^{-n}$ , where Q is the magnitude of the CPE,  $j^2 = -1$ ,  $\omega$  is the angular frequency, and n (between 0 to 1) is the exponential term [30]. It's well known that for almost all Al and alloys protective and sticky oxide films occur on the surface with various environments [31]. So  $Q_p$  and  $R_p$  were the first important parameters for the corrosion protection of WZ. Lower  $Q_p$  indicates greater corrosion resistance and less ion absorption from the electrolyte by the passive film during immersion. The fact that the  $R_p$  increased as welding current increased (0.45, 14.59, and 928 for 110A, 140A, and 170A, respectively) indicates that the resistance of the passive oxide coating was enhanced. Additionally, as Sicupira et al. [30] pointed out, the diameter of the slope represents the charge transfer resistance, or, more specifically, the resistance of the passive film, and it is an indication that the corrosion resistance increased with a larger diameter of the slope. Here, it is thought that it may be due to the increase in the resistance of the oxide film due to the increase in the amount of Al diffused from base metal to weld seam with the increased welding current. Supporting this, the capacitance values of passive films, which is known as  $Q_p$ , are also decreased with increased welding current ( $32.53, 19.96, \text{ and } 15.23 \text{ F} \times \text{s}^{(a_1-1)} \times 10^{-6}$  for 110A, 140A, and 170A, respectively). These values, which are valid for the passive film, coincide with the Tafel extrapolation values obtained from the PDS curves for the samples after T6 heat treatment, and the corrosion resistance of the 110 increased after T6 heat treatment ( $R_p$ : 2684, 26.44, and 41.18  $\Omega$  and  $Q_p$ : 19.56, 57.12, and 22.51  $\text{F} \times \text{s}^{(a_1-1)} \times 10^{-6}$  for HT-110A, HT-140A, and HT-170A, respectively). As can be seen in the cross-sectional macro image (Fig. 1), similar results were observed for the  $R_{pit}$  and  $Q_{pit}$  values in the equivalent circuit [32], which occur due to the pittings seen especially in the weld seam.  $R_{pit}$  values were calculated at 3075, 4751, 4808, 4562, 1923, and 3837  $\Omega$  for 110A, 140A, 170A, HT-110A, HT-140A, and HT-170A, respectively. On the other hand,  $Q_{pit}$  values were calculated at 29.23, 13.18, 6.36, 11.00, 43.57, and 27.01  $\text{F} \times \text{s}^{(a_1-1)} \times 10^{-6}$  for 110A, 140A, 170A, HT-110A, HT-140A, and HT-170A, respectively. Here, more observable pittings on the 170A and HT-170A samples did not cause the  $R_{pit}$  and  $Q_{pit}$  trends to change. It is predicted that the grain size/structure, the size/number of the pittings, and the amount, size, and composition of precipitations (such as  $\text{Al}_2\text{Cu}$ ,  $\text{Mg}_2\text{Si}$ , etc.) may have occurred as a result of the different welding currents.

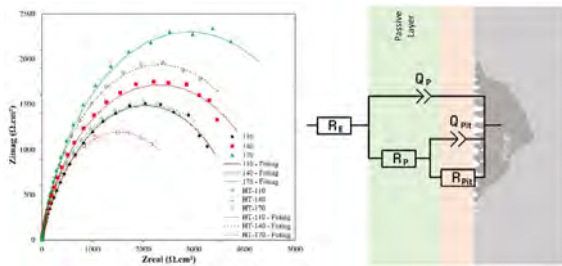


**Figure 8.** Fitting results of Nyquist diagrams with proposed equivalent circuit model on the surface of WZs

**Table 3.** Fitting parameters of the equivalent circuits with two time constants for Al6013 GTAW welded with ER4047 filler in 3.5% NaCl at room temperature presented in Fig. 8

Samples	$R_E$ ( $\Omega$ )	$Q_P$ ( $F \times 5^{(a_2-1)} \times 10^{-6}$ )	$a_1$	$R_P$ ( $\Omega$ )	$Q_{Pit}$ ( $F \times 5^{(a_3-1)} \times 10^{-6}$ )	$a_3$	$R_{Pit}$ ( $\Omega$ )
110A	1.414	32.53	0.89	0.45	29.23	0.76	3075
140A	2.115	19.96	0.88	14.59	13.18	0.82	4751
170A	2.470	15.23	0.74	928	6.36	0.98	5808
HT-110A	2.470	19.56	0.18	2684	11.00	0.93	4562
HT-140A	1.405	57.12	0.92	26.44	43.57	0.52	1923
HT-170A	2.045	22.51	0.90	41.18	27.01	0.88	3837

SEM images of corrosion defects occurring in HAZ after electrochemical corrosion tests of 110A, 140A, 170A, HT-110A, HT-140A, and HT-170A, respectively, are given in Fig. 9. It is thought that pitting corrosion occurs as a result of the cathode behaviour of the Al-Cu-Mg-Si precipitated particles at the grain boundary and acts as a cathode compared to the grain boundaries. In other terms, a galvanic couple occurs between precipitated particles and grain boundaries. In other words, pitting corrosion started with the presence of these precipitated particles at the grain boundaries. On the other hand, intergranular corrosion started on the surface and with the pitting corrosion continued a mixed corrosion mechanism [22]. Presumably, while intergranular corrosion will increase the pitting width, the pitting corrosion will also lead to deep corrosion with increasing immersion time [9]. In the post-corrosion SEM pictures of the samples that were post-weld, especially with the higher welding current, micropores that are inner walls of the pittings were not visible because of the rise in diffusion phenomena in the grains in the HAZ. A similar situation was observed in the post-corrosion SEM images of the HAZ of the T6 heat treated samples. So, as Braun [22] mentioned corrosion mechanism was independent of heat treatment for 6XXX Al alloys. With the exception of HT-170A, a relative decrease in the size of the pittings on the HAZ surface was seen after the T6 heat treatment. These pore sizes are compatible and supportive with the values specified in Fig. 8 and Table 3 and the equivalent circuit model. In T6 heat treated WZs, it was found that grain boundaries had a greater impact on corrosion as welding current increased. In other words, it was determined that the size of the pitting corrosion increased. The most important result that can be obtained from the post-weld SEM surface morphologies is

that the increased welding current is quite effective in preventing pitting corrosion, which is a very dangerous type of corrosion [7,18]. Both PDS and EIS curves show that the corrosion resistance of the HT-110A increased. As shown in Fig. 9d, the pitting area has decreased, but it is anticipated that longer exposure time will increase the damage of pitting corrosion due to poor grain growth grain which caused by low welding current. This shows that it is very important to perform OM or SEM morphology examinations on surfaces after electrochemical corrosion measurements for detailed corrosion examination.

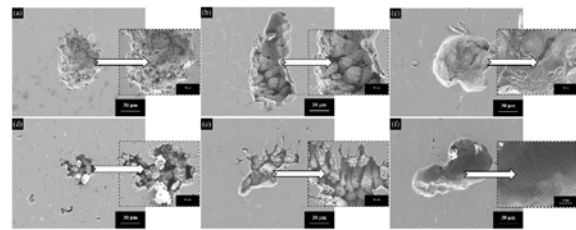


**Figure 9.** Post-corrosion SEM surface morphology investigation of WZs, (a, d) 110A, HT-110A, (b, e) 140A, HT-140A, and (c, f) 170A, HT-170A, respectively

## CONCLUSION

In this study, Al6013 base metal was successfully joined with different welding currents by the GTAW method using ER4047 filler metal. To examine the effect of post-weld aging on different welds current, T6 heat treatment was carried out. The findings of the study can be summarized as follows;

- It was observed that the base metal and weld seam were tightly joined with all welding currents, and porosities were encountered on the weld seam with the increasing welding current. Furthermore, it has been predicted that the HAZ will expand with increasing welding current. Elemental compositions of both Al6013 and ER4047 were proved with EDX analyses.  $Al_2Cu$  and  $Mg_2Si$  precipitates were encountered in XRD results.

- The effects of both welding current and T6 heat treatment on the WZs are investigated with PDS tests. It was revealed that the corrosion resistance increased as the welding current increased ( $3.61$ ,  $2.95$ , and  $1.38 \mu A \cdot cm^{-2}$  for 110A, 140A, and 170A, respectively). However, with the T6 heat treatment, the corrosion resistance of 110A increased, surprisingly ( $3.61$  to  $2.08 \mu A \cdot cm^{-2}$ ). This phenomenon is thought to be the result of increased Al diffusion from base metal to weld seam.

- Passive film characterization on WZs have been revealed with EIS tests according to both the Nyquist and Bode diagrams, as well as the proposed equivalent circuit



model. A two-constant equivalent circuit consisting of resistors and constant phase elements is recommended for all samples. Accordingly, it agrees with the proposed model that both a passive film is formed on the surface due to the Al and pitting occurs as a result of the different welding currents.

- Moreover, SEM surface morphology after corrosion tests confirmed that, pitting size and shape changes with various processes on weld seams, especially. It has been revealed that precipitates (such as  $Al_2Cu$  and  $Mg_2Si$  for Al alloys) that may occur in the microstructure during or after welding are very important in terms of corrosion susceptibilities. As a suggestion, it has been revealed that electrochemical methods do not give accurate results alone in corrosion measurements, moreover, surface morphology examinations such as OM or SEM can provide a more reliable result.

## ACKNOWLEDGEMENT

The author would like to thank Professor Burak Dikici for helpful contribution on electrochemical corrosion tests..

## CONFLICT OF INTEREST

Authors approve that to the best of their knowledge, there is not any conflict of interest or common interest with an institution/organization or a person that may affect the review process of the paper.

---

## REFERENCES

---

- Demirbaş K, Çevik S. TIG Kaynak Yöntemiyle Birleştirilmiş Alüminyum 1050 Alaşımının Mekanik Ve Mikroyapı Özellikleri, *Academic Platform Journal of Engineering and Science*, 2020 471-477.
- Mercan E, Ayan Y, Kahraman N. Investigation on joint properties of AA5754 and AA6013 dissimilar aluminum alloys welded using automatic GMAW, *Engineering Science and Technology, an International Journal*, 23 (4) 2020 723-731.
- Kosedag E, Ekici R. Low-velocity impact performance of B4C particle-reinforced Al 6061 metal matrix composites, *Materials Research Express*, 6 (12) 2019 126556.
- Pantelakis SG, Daglaras PG, Apostolopoulos CA. Tensile and energy density properties of 2024, 6013, 8090 and 2091 aircraft aluminum alloy after corrosion exposure, *Theoretical and Applied Fracture Mechanics*, 33 (2) 2000 117-134.
- Salah AN, Mabuwa S, Mehdi H, Msomi V, Kaddami M, et al., Effect of Multipass FSP on Si-rich TIG Welded Joint of Dissimilar Aluminum Alloys AA8011-H14 and AA5083-H321: EBSD and Microstructural Evolutions, *Silicon*, 14 (15) 2022 9925-9941.
- Ayvaz M. Determination of the effect of artificial aging parameters on dry sliding wear resistance of 6013 aluminum alloy (Al-Mg-Si-Cu), *International Advanced Researches and Engineering Journal*, 5 (2) 2021 181-187.
- Petroyiannis P V., Kermanidis AT, Papanikos P, Pantelakis SG. Corrosion-induced hydrogen embrittlement of 2024 and 6013 aluminum alloys, *Theoretical and Applied Fracture Mechanics*, 41 (1-3) 2004 173-183.
- Barbosa C, Dille J, Delplancke J-L, Rebello JMA, Acelrad O. A microstructural study of flash welded and aged 6061 and 6013 aluminum alloys, *Materials Characterization*, 57 (3) 2006 187-192.
- Braun R, Investigation on Microstructure and Corrosion Behaviour of 6XXX Series Aluminium Alloys, *Materials Science Forum*, 519-521 2006 735-740.
- Haryadi GD, Kim SJ. Influences of post weld heat treatment on fatigue crack growth behavior of TIG welding of 6013 T4 aluminum alloy joint (Part 1. Fatigue crack growth across the weld metal), *Journal of Mechanical Science and Technology*, 25 (9) 2011 2161-2170.
- Made Wicaksana Ekaputra I, Dwi Haryadi G, Mardikus S, Dewa RT. Probabilistic evaluation of fatigue crack growth rate for longitudinal tungsten inert gas welded al 6013-T4 under various postweld heat treatment conditions, *E3S Web of Conferences*, 130 2019.
- He L, Zhang H., Cui J. Effects of thermomechanical treatment on the mechanical properties and microstructures of 6013 alloy, *Journal of Wuhan University of Technology-Mater. Sci. Ed.*, 24 (2) 2009 198-201.
- Lei G, Wang B, Lu J, Wang C, Li Y, et al. Microstructure, mechanical properties, and corrosion resistance of continuous heating aging 6013 aluminum alloy, *Journal of Materials Research and Technology*, 18 2022 370-383.
- Varshney D, Kumar K. Application and use of different aluminium alloys with respect to workability, strength and welding parameter optimization, *Ain Shams Engineering Journal*, 12 (1) 2021 1143-1152.
- Li H, Zou J, Yao J, Peng H. The effect of TIG welding techniques on microstructure, properties and porosity of the welded joint of 2219 aluminum alloy, *Journal of Alloys and Compounds*, 727 2017 531-539.
- Zhao Z, Liang H, Zhao Y, Yan K. Effect of Exchanging Advancing and Retreating Side Materials on Mechanical Properties and Electrochemical Corrosion Resistance of Dissimilar 6013-T4 and 7003 Aluminum Alloys FSW Joints, *Journal of Materials Engineering and Performance*, 27 (4) 2018 1777-1783.
- Çetinkaya C, Tekeli S, Kurtuluş O. Alüminyum Alaşımlarının Kaynaklanabilirliği ve Kaynak Parametrelerinin Mekanik Özelliklere ve Mikroyapıya Etkisi, *Politeknik Dergisi*, 5 (4) 2002 321-335.
- Abo Zeid EF. Mechanical and electrochemical characteristics of solutionized AA 6061, AA6013 and AA 5086 aluminum alloys, *Journal of Materials Research and Technology*, 8 (2) 2019 1870-1877.
- Kosedag E, Ekici R. Low-velocity and ballistic impact resistances of particle reinforced metal-matrix composites: An experimental study, *Journal of Composite Materials*, 56 (7) 2022 991-1002.
- Yürük A, Çevik B, Kahraman N. Analysis of mechanical and microstructural properties of gas metal arc welded dissimilar aluminum alloys (AA5754/AA6013), *Materials Chemistry and Physics*, 273 (March) 2021 125117.
- Jeyaprakash N, Haile A, Arunprasath M. The Parameters and Equipments Used in TIG Welding: A Review, *International Journal of Engineering Science*, 2015 2319-1813.
- Braun R. Investigations on the long-term stability of 6013-T6 sheet, *Materials Characterization*, 56 (2) 2006 85-95.
- ASTM International, ASTM G59 - Standard test method for conducting potentiodynamic polarization resistance measurements,

- Volume 97, (West Conshohocken, PA, USA), 2014.
24. Mansfeld F. Electrochemical impedance spectroscopy (EIS) as a new tool for investigating methods of corrosion protection, *Electrochimica Acta*, 35 (10) 1990 1533–1544.
  25. Carvill J. *Mechanical Engineer's Data Handbook*, 1st ed., (Butterworth-Heinemann), 1993.
  26. Kartsonakis IA, Balaskas AC, Koumoulos EP, Charitidis CA, Kordas G. Evaluation of corrosion resistance of magnesium alloy ZK10 coated with hybrid organic–inorganic film including containers, *Corrosion Science*, 65 2012 481–493.
  27. Çomaklı O. Improved structural, mechanical, corrosion and tribocorrosion properties of Ti45Nb alloys by TiN, TiAlN monolayers, and TiAlN/TiN multilayer ceramic films, *Ceramics International*, 47 (3) 2021 4149–4156.
  28. Tozkoparan B, Dikici B, Topuz M, Bedir F, Gavgali M. Al-5Cu/B4Cp composites: The combined effect of artificially aging (T6) and particle volume fractions on the corrosion behaviour, *Advanced Powder Technology*, 31 (7) 2020 2833–2842.
  29. Singh IB, Mandal DP, Singh M, Das S. Influence of SiC particles addition on the corrosion behavior of 2014 Al-Cu alloy in 3.5% NaCl solution, *Corrosion Science*, 51 (2) 2009 234–241.
  30. Sicupira DC, Cardoso Junior R, Bracarense AQ, Frankel GS, de V. Electrochemical study of passive films formed on welded lean duplex stainless steel, *Materials and Corrosion*, 68 (6) 2017 604–612.
  31. Dikici B, Topuz M. Production of Annealed Cold-Sprayed 316L Stainless Steel Coatings for Biomedical Applications and Their in-vitro Corrosion Response, *Protection of Metals and Physical Chemistry of Surfaces*, 54 (2) 2018 333–339.
  32. Cabot PL, Garrido JA, Pe' rez E, Moreira AH, Sumodjo PTA, et al. EIS study of heat-treated Al-Zn-Mg alloys in the passive and transpassive potential regions, *Electrochimica Acta*, 40 (4) 1995 447–454.